Design of the Ion Optical Components in a Time-of-flight Mass Spectrometer For The Study of Ultracold Chemistry

by

Davis Holmes

Supervisor: Dr. Kirk Madison

A THESIS SUBMITTED IN PARTIAL FULFILLMENT OF
THE REQUIREMENTS FOR THE DEGREE OF

Bachelor of Science in Engineering Physics

in

The Faculty of Applied Sciences

Queen's University
(Kingston)
September 1, 2009

Abstract

The design of ion optical components for a time-of-flight mass spectrometer (TOF-MS) was motivated by the recent interest in the study of chemical reaction resonances. An optimal setting to study these resonances would have reactants with very well defined kinetic energies. The system proposed to accomplish this uses a magneto-optical trap (MOT) to localize and cool atoms to temperatures below 100μK, which act as targets for a beam of cold molecules created using a hexapole Stark guide. The reaction products would then be ionized through resonance-enhanced multiphoton ionization (REMPI) and analyzed with a TOF-MS.

Many obstacles were presented by the high voltage hexapole's close proximity with the TOF-MS electrodes. However, they were overcome by a careful selection of dimensions and active shielding. Adding the MOT brought about other constraints: off-axis ion detection and open aperature extraction plates. The issues that these generated were solved by employing a set of parallel deflection plates and an Einzel lens. Engineering solutions were tested by simulating ion trajectories in SIMION 3D™, a commonly used commerical program in mass spectrometer design. To keep solutions financially feasible, a budget constraint of $100,000 was put in place. The mass resolution goal of 200 was met for heavy, cold molecules but was not met for light, hot atoms. The final electrode configuration had a transmission efficiency of approximately 100% in all scenarios that were simulated, surpassing the 95% benchmark. The end result is a TOF-MS electrode geometry with sufficient performance characteristics to resolve the masses of particles likely to be used in the study of ultracold chemistry.

Acknowledgements

Cutting short a plan to extend my undergraduate degree left me with the task of completing this thesis over the summer of 2009. Without a supervisor by May 13^{th}, I was nearly forced to register for a 5th year of schooling, when Dr. Madison and I connected, and he agreed to be my supervisor. This work would not have been possible without his guidance. Taking time out of his schedule for weekly meetings, consistently consuming 2 hours or more at a time, was a large sacrifice for him to make on my behalf, and for that I am grateful. Routinely, Dr. James Booth and Dr. Taka Momose attended the meetings providing invaluable insight and experience, which manifests itself in the soundness of this design.

This thesis also could not have been completed if a Queen's professor was not willing to support me. Dr. James Fraser graciously fulfilled this role with routine meetings through VoIP to keep my design on track and provide much needed feedback for the actual writting of this thesis. He displayed the same sincere and knowledgable perspective that he did when teaching me in PHYS460 and for that I am grateful.

I would like to thank my parents and brothers for their understanding of my need for seclusion over the entire summer to complete this project. Their continued support and encouragement as well as willingness to work around my schedule whenever possible made this process easier to embrace and for that I am grateful.

Contents

1 Introduction **1**

2 Time-of-flight Principles **2**

3 The Design **4**

3.1 Nominal Geometry 6

3.2 Generating Ions 8

3.3 Distortion due to the Hexapole 8

3.3.1 Background 8

3.3.2 Test & Measurments 9

3.4 Extraction Plate Focusing 10

3.4.1 Background 10

3.4.2 Tests/Measurements 11

3.5 Deflection Plates 12

3.5.1 Background 12

3.5.2 Tests/Measurements 12

3.6 Final Geometry 14

3.7 Realistic Conditions 14

3.7.1 Background 14

3.7.2 Wide Ionization Beam 15

3.7.3 Laser Misalignment 15

3.7.4 Hot and Cold Products 17

3.8 Drawbacks in Resolution 18

4 Budget **19**

5 Summary **19**

6 Future Work **20**

A Background **24**

A.1 Magneto-optical Trapping 24

A.1.1 Principles 24

A.1.2 Anti-Helmholtz Coils 25

A.2 2D-MOT Loader 26

A.3 Resonant-enhanced Multiphoton Ionization . . . 27
A.4 Ultracold Molecular Beam . . . 28

B Miscellaneous **30**
B.1 Nominal Geometry . . . 30
B.2 Electrode Material Selection . . . 30
B.3 Ion Generation . . . 31
B.4 Detector Orientation . . . 34
B.5 Final Geometry . . . 35
B.5.1 Extraction Plates . . . 35
B.5.2 Einzel Lens . . . 36
B.5.3 Deflection Plates . . . 36
B.5.4 SIMION Model . . . 36
B.6 Resolution Drawbacks . . . 37
B.7 Detection Limit Calculations . . . 40
B.7.1 Geometric Efficiency . . . 41
B.7.2 Ionization Efficiency . . . 42
B.7.3 Transmission Efficiency . . . 43
B.7.4 Detector Efficiency . . . 43
B.8 Budget . . . 44
B.8.1 3D-MOT Vacuum . . . 44
B.8.2 Optics . . . 45
B.8.3 2D-MOT Loader . . . 45
B.8.4 3D-MOT Magnet . . . 46
B.8.5 TOF-MS Electronics and Data Acquisition System . . . 46

C Additional Case Analyses **47**
C.1 Hexapole Distortion . . . 47
C.1.1 Simplest Geometry (No Hexapole) . . . 47
C.1.2 Nominal Geometry . . . 49
C.1.3 Solid Lower Plate . . . 51
C.1.4 Square Plates . . . 53
C.1.5 Complete Drift Shield . . . 55
C.2 Magnetic Interference . . . 56
C.2.1 Background . . . 56

C.2.2 Tests/Measurements . . . 58
C.3 Lensing . . . 62
C.3.1 Extraction Plates' Focal Length . . . 62
C.3.2 Einzel Lens Operating Modes . . . 63
C.4 Realistic Conditions . . . 64
C.4.1 Large Ionization Volume . . . 64
C.4.2 Li + OH Reaction Assumptions . . . 66
C.4.3 Hot & Cold Products . . . 67
C.5 Space Focus Tunability . . . 69
C.6 Hexapole Orientation . . . 71

D Ion Detectors **75**

E Vacuum **76**

F Ray Optics **77**
F.1 Aperture Lenses . . . 77
F.2 Einzel Lenses . . . 77
F.3 Deflection Plates . . . 78

List of Figures

1 TOF-MS sequence of events . . . 3
2 General TOF-MS instrumentation . . . 4
3 Orientation of MOT, hexapole and TOF-MS . . . 5
4 Design challenges outline . . . 6
5 SIMION model of nominal geometry . . . 7
6 SIMION view of ionization volume . . . 8
7 Illustration of unwanted deflection due to hexapole . . . 9
8 Implementation of drift shield solution . . . 10
9 Optical analogy of extraction plate-Einzel lens combination . . . 11
10 Extraction plate focal distance curve . . . 12
11 Parallel plates' fringe fields effects . . . 13
12 Final geometry with key dimensions highlighted . . . 14
13 Mass resolution using a wide ionization beam . . . 15
14 Mass resolution with misaligned ionization laser . . . 16
15 TOF histogram at space focuses with ideal and non-ideal laser alignment . . . 16
16 Mass resolution of hydrogen product from Li + OH reaction . . . 17
17 General MOT layout . . . 24
18 Spatial force dependence due to Zeeman effect . . . 25
19 Anti-Helmholtz coils configuration . . . 25
20 Laser ionization schemes . . . 27
21 Dr. Momose's hexapole assmebly . . . 28
22 Hexapole geometry . . . 29
23 Ionization volume position distributions . . . 32
24 Ionization volume initial velocity and energy distributions . . . 33
25 Detector orientations . . . 34
26 Standard deviation of ion cloud along flight path . . . 34
27 Extraction plate drawings . . . 35
28 Einzel lens drawings . . . 36
29 Deflection plate drawings . . . 36
30 Isometric view of the final geometry's cross section in SIMION™ . . . 37
31 Ideal geometry's E_x asymmetry . . . 48
32 Average x position of ions in ideal geometry . . . 48
33 Nominal geometry's E_x asymmetry . . . 49

34 Average x position of ion cloud in nominal geometry 50
35 E_x asymmetry using a solid lower plate geometry 51
36 Average x position of ions along flight path using a solid lower plate geometry . . 52
37 E_x asymmetry using a square plate geometry 53
38 Average x position along flight path using a square plate geometry 54
39 Complete drift shield E_x asymmetry 55
40 Average x position using complete drift shield 56
41 Influence of magnetic field from 200mm coils ($\frac{dB_z}{dz} = 10$G/cm) on mass resolution 58
42 Influence of magnetic field from 300mm coils ($\frac{dB_z}{dz} = 10$G/cm) on mass resolution 59
43 Influence of magnetic field from 300mm coils ($\frac{dB_z}{dz} = 100$G/cm) on mass resolution 60
44 Screenshots of SIMION with middle plate voltage at 800V and $\frac{dB_z}{dz}|_{mot} = 100$G/cm 60
45 Screenshots of SIMION with middle plate voltage at 800V and $\frac{dB_z}{dz}|_{mot} = 0$G/cm 61
46 Mass resolution over the entire drift length in the presence of magnetic field ($\frac{dB_z}{dz} = 10$G/cm) 62
47 Beam width over entire drift length 63
48 Einzel lens operating mode mass resolution comparison 64
49 SIMION screen shots of ion trajectories with large ionization volume 65
50 Comparison of mass resolution when ions are produced outside of the nominal volume 66
51 TOF histogram at the space focus when the ionzation volume is $\Delta x = 75$mm, $\Delta y = \Delta z = 0.1$mm. 66
52 Mass resolution over entire drift length comparing 1amu particles at 4000K with 100amu particles at 1K 68
53 Mass resolution over entire drift length comparing 1amu particles at 5000K with 100amu particles at 1K 69
54 Slot aperture geometry 70
55 Location of space focus in drift region as a function of middle plate voltage . . . 71
56 Two possible hexapole orientations (red = molecular beam, yellow = trapped atoms) 71
57 Hexapole orientations 73
58 Mass resolution over drift length for standard and non-standard hexapole orientations 74
59 Average x position over drift length for standard and non-standard hexapole orientations 74
60 General aperature lens 77
61 Einzel lens schematic displaying the reference plane (or mid-plane), 2 principal focal planes (PF) and 2 principal planes(PP) (11) 78

62 Ideal deflection of ion trajectory by parallel plates 79
63 Rotation of isochronous surface by parallel plates 79
64 Plot of the change in effective parallel plate length due to thin field terminators . 80
65 Field terminator geometry (36). 80

Nomenclature

V_1	voltage on the lower extraction plate
V_2	voltage on the middle extraction plate
V_3	voltage on the upper extraction plate
DOF	degree-of-freedom
ITO	indium tin oxide
LIMS	laser ionization time-of-flight mass spectrometer
MCP	microchannel plate
MOT	magneto-optical trap
MS	mass spectrometer
NRMPI	non-resonant multiphoton ionization
REMPI	resonance-enhanced multiphoton ionization
TOF-MS	time-of-flight mass spectrometer

1 Introduction

Resonances in chemical reaction rates are a major topic in modern chemical physics. Systems to contain reactants with very well defined kinetic energies are starting to be realized, and will provide much needed experimental tools to study chemical reaction resonances(1).

Magneto-optical traps (MOTs) are devices that localize and cool atoms to extremely low temperatures and can act as ideal sources of reactants for ultracold chemistry. Dr. Kirk Madison's group at the University of British Columbia (UBC) performs research using MOTs and can consistently produce a tightly confined cloud of ultracold atoms ($< 100\mu$K)) with a density as high as 10^{10}cm^{-3} and a diameter of approximately 1mm (2).

For the second source of reactants, a beam of molecules with a very narrow kinetic energy distribution is required. There are many methods for producing cold molecular beams with temperatures approaching those achieved with MOTs (3). Dr. Taka Momose's research group at UBC has created a working hexapole velocity filter that produces a pulsed beam containing $\sim 10^9$ cold molecules (< 100mK).

The motivation for the design of a time-of-flight mass spectrometer (TOF-MS) is derived from the need to study the reaction products resulting from the collision of the molecular beam with the trapped atoms. The crux of any TOF-MS design is its ion optics that transport a cloud of charged particles towards a detector. The overall system design process for TOF-MSs is well described by many texts and article reviews and for that reason is not the main focus of this report.

The combination of a MOT, hexapole velocity filter and TOF-MS has never been described in literature. Many challenges arise when the three systems are brought together that must be investigated in order to provide an engineering solution. The major issues that will be addressed with this design stem from (i) the MOT's magnetic field and requirement of optical access for 3 pairs of orthogonal lasers, and (ii) the hexapole's requirement of close proximity to the MOT and acceleration region of the TOF-MS. To study these problems and gauge the performance of proposed solutions, the trajectories of ions in the TOF-MS will be simulated using SIMION™.

The study of ultracold chemistry will involve light, simple molecules, likely with masses below 100amu. A mass resolution goal of 200 was set, which provides a safety factor of ~ 2 if the largest mass for this system to analyze is 100amu. The sensitivity of mass spectrometers has reached the single particle level (4); however, from a counting statistics perspective, detection limits lie in the range of 10 to 100 particles. The original detection limit goal of this mass spectrometer was set for 50 molecules; however, verifying this goal relies on tenuous approximations. A more appropriate performance objective is to discuss the transmission efficiency of the ion optics which lie at the heart of this design. Therefore, the detection limit objective was replaced by the goal of achieving an ion transmission efficiency greater than 95%. An additional goal of keeping the budget of the TOF-MS below $100,000 was established to ensure that any engineering solutions are also feasible from financial perspective.

Both of these goals will be judged based on the full width at half maximum definition of resolution. The experimental conditions constraining the ions during performance evaluation are (i) the ions must start within the nominal ionization volume outlined in section 3.2, and (ii) the ions must have realistic initial velocity conditions; examples of such conditions are to be based on the advice of Dr. Madison.

2 Time-of-flight Principles

Ions with the same charge but different mass will take different lengths of time to travel a given distance if they have the same kinetic energy. The general relationship between flight time and mass is,

$$t^2 = \frac{mD^2}{2eV}, \tag{1}$$

where t is time it takes for a singly charged (+) ion to travel to the detector, V is the potential difference that the ion is accelerated through, m is the mass of the ion and D is approximately the distance between the starting location and the detector. The actual relationship between time and mass is more complicated but still displays the same $t^2 \propto m$ relationship (5).

When TOF mass spectrometry is performed, the ion cloud has finite spatial dimensions and non-zero initial velocities, resulting in an arrival time signal with a finite height and width. The obvious performance measure of a mass spectrometer is mass resolution, ie. if two different species are ionized in the same volume, are the two signals separated in time enough to be quantitatively discerned? The electrical output from an ion detector is a series of pulses and the definition for sufficient peak separation is that the peaks' centroids must be separated by a minimum of one peak width. There are two generally accepted definitions for peak width: the full width at half max (FWHM) and the full width at 10% of max (FWTM) (6). For the remainder of the report the symbols representing resolution using these two definitions will be R_{50} and R_{10}.

Two similar definitions were defined for this report: the full width at 0% of max (FWZM) and full width at 1 standard deviation from max (FWSDM).[1] The symbol for mass resolution corresponding to these two definitions of peak width are R_0 and R_{SD}. The R_0 definition provided a more accurate comparison between the performance of different geometries. The R_{SD} definition was easier to implement from a programming standpoint and consistently was within 5% of R_{50}.

To calculate mass resolution based on temporal characteristics, the following equation is used,

$$\frac{m}{\Delta m} = \frac{t}{2\Delta t}, \tag{2}$$

where Δt is one of the definitions of peak width described above and t is the time aligned with the peak's centroid. This result is easily derived from equation 1.

Wiley and McLaren (5) published one of the most cited works in TOF mass spectrometry because they devised a TOF-MS with an adjustable space focus. The space focus is the plane in the drift region where ions that started deeper in the extraction region overtake ions that started closer to the detector as illustrated by figure 2.

[1] Generally, peaks in mass spectra can be represented by Gaussian lineshapes; however, simulation results with unusual peak shapes occured during the initial design stages and using the standard definitions of resolution skewed results.

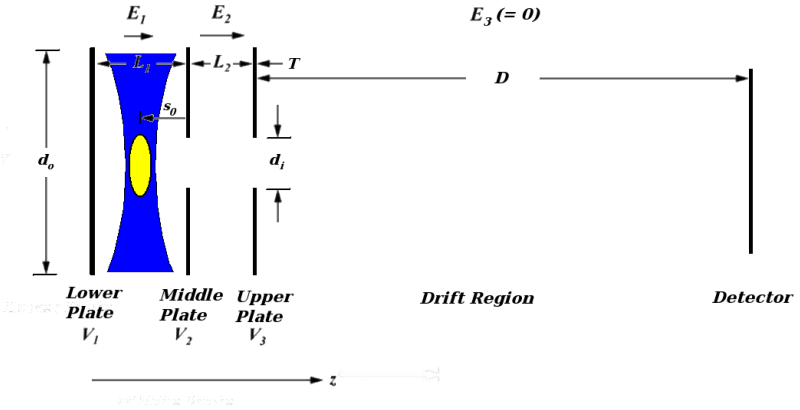

(a) Ionization

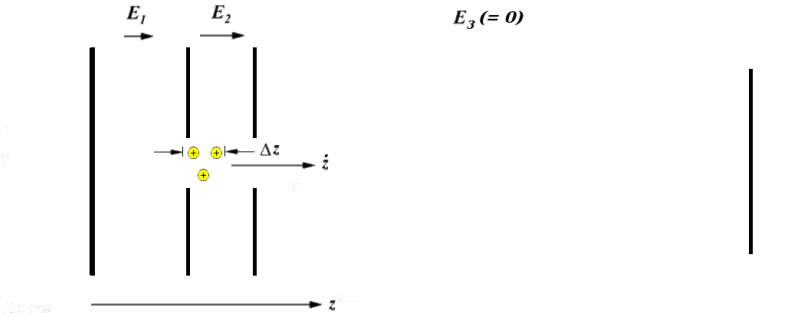

(b) Acceleration

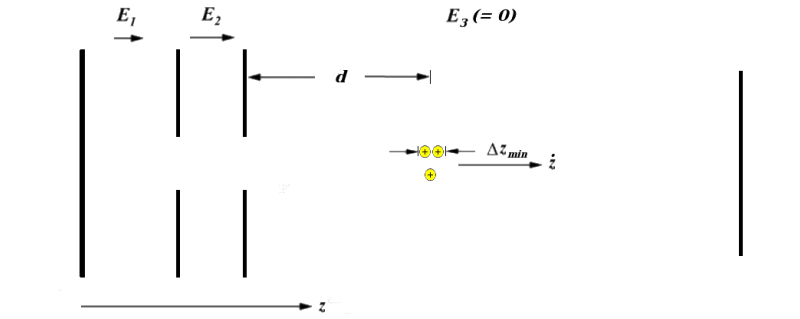

(c) Space Focus

Figure 1. Sequence of events in TOF-MS: (a) neutral particles are ionized by a pulsed UV laser (blue), (b) ions are accelerated through extraction plates, (c) ions reach point in space where their separation is a minimum (space focus), which can be moved to the detector's location

The mass resolution significantly increases at this point because the ion packet's width for all ion masses reaches a minimum. According to (5), the space focus condition is given by

$$d = 2s_0 k_0^{\frac{3}{2}} \left(1 - \frac{1}{k_0 + k_0^{\frac{1}{2}}} \frac{L_2}{s_0} \right), \tag{3}$$

where d is the drift length coincident with the space focus, k_0 is a characteristic ratio of the system, s_0 is the distance between the ions' average starting location and the middle plate, and

L_2 is the distance between the middle and upper plates. k_0 represents the ratio of the total energy that the particle gains from the first and second electric field to the energy that the particle gains from the first electric field alone; it is defined by

$$k_0 = \frac{s_0 E_1 + L_2 E_2}{s_0 E_1} = 1 + \frac{L_2}{s_0}\frac{E_2}{E_1} \tag{4}$$

where E_1 is the electric field in the first extraction region and E_2 is the electric field in the second extraction region. Equation 4 displays that in order to move the space focus further away from the source, the ratio L_2/s_0 must be increased or E_2/E_1 must be increased. In general, the resolution of a TOF-MS is a function of k_0, so it is the ratio of lengths and field strengths that govern its overall performance.

3 The Design

A TOF-MS consists of (i) extraction plates and possibly other ion optical elements, (ii) an ion detector, (iii) a vacuum chamber, (iv) pulse electronics, (v) an ionization source, and (vi) a signal storage device. Item (i) is the largest concern when designing any TOF-MS because the last four items are either components that can be purchased as standard parts or built based on the designs of others. Each of these areas will be discussed, however, only item (i) was considered at length. A linear, laser ionization TOF-MS (LIMS) with the major components outlined can be seen in figure 2.

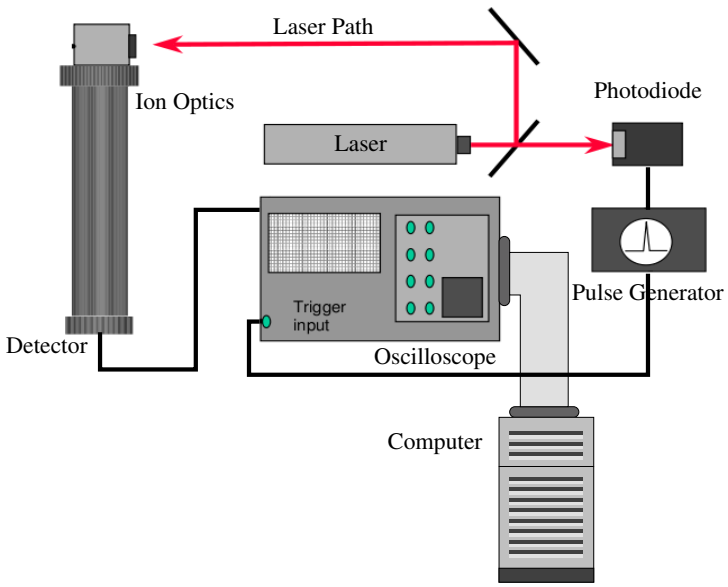

Figure 2. General TOF-MS instrumentation. Laser acts as ionization source; ion optics are contained in a linear vacuum chamber; detector is in vacuum at one end of the vacuum chamber; oscilloscope digitizes the electrical output from the detector and dumps its memory into a computer for offline analysis; photodiode and pulse generator constitute pulse electronics to trigger the oscilloscope. Adapted from (7).

This design specifically sets out to develop the ion optics required for a TOF-MS to be combined with a MOT and a hexapole Stark guide. The end result is an ion optical system with the form seen in figure 3(a).

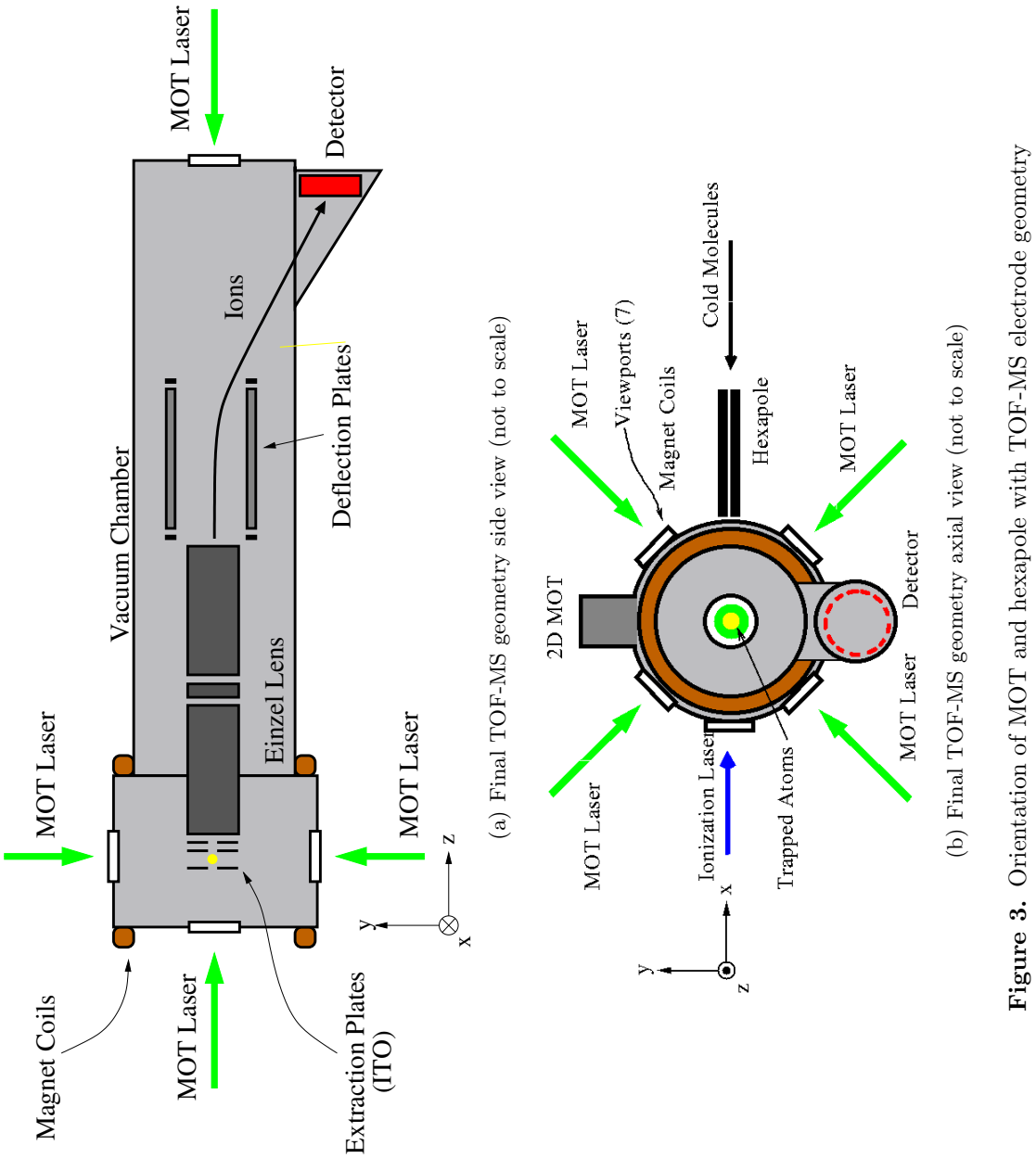

(a) Final TOF-MS geometry side view (not to scale)

(b) Final TOF-MS geometry axial view (not to scale)

Figure 3. Orientation of MOT and hexapole with TOF-MS electrode geometry

This design was approached from the premise that the TOF-MS would be a modified Wiley-McLaren mass spectrometer (5); components and complexity were added only as needed until the final geometry was reached.

As can be seen from figure 3, atoms trapped inside the MOT must have a direct line of sight with the hexapole guide (see appendix A.4 for the hexapole's geoemtry). Also, the atoms must lie along the central axis of the parallel plates used by the TOF-MS for sufficient optical access. The method of ionization used to create the ions is known as resonance-enhanced multiphoton ionization (REMPI) ; further details concerning the details of the process and reasons for using this method are given in appendix A.3.

Generally, a TOF-MS can be modeled using a 1D approach to express the dynamics of the ions as they fly towards the detector. This approach cannot be accurately applied to this system because this system requires (i) a high voltage hexapole be in close proximity with the ionization region and (ii) the ions be detected off of the normal flight axis to provide optical access for two of the MOT lasers . This project sets out to understand the severity of the issues that these constraints create and engineer solutions to mitigate their influence. The investigation process aimed to explore the areas outlined in figure 4.

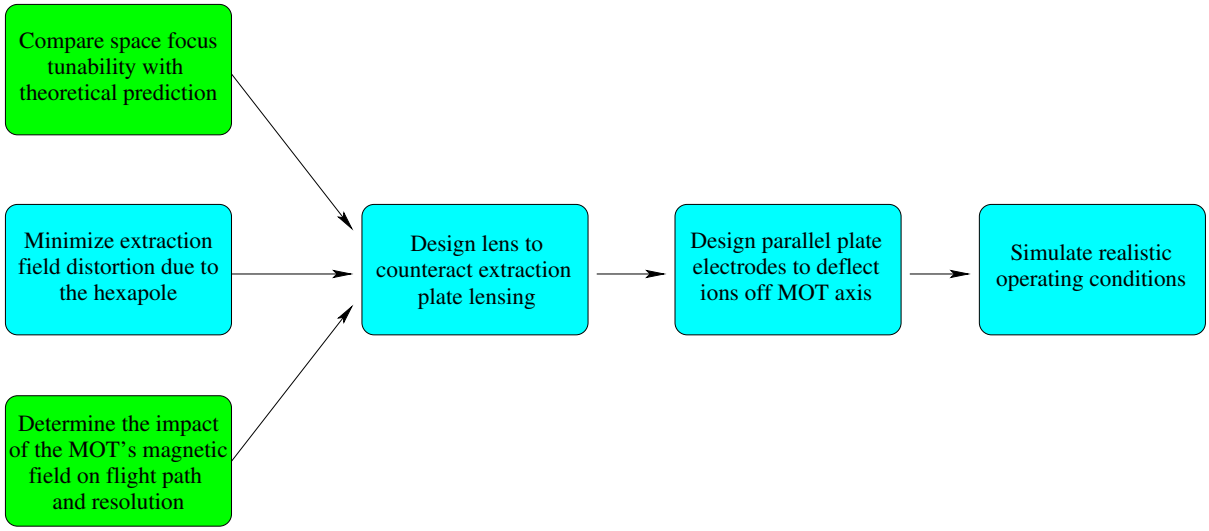

Figure 4. Design challenges to integrate MOT and high voltage hexapole with TOF-MS. Items in blue are discussed in the main report while items in green are discussed in the appendix.

3.1 Nominal Geometry

A nominal geometry provided a basic system on which complexity could be added and performance measures could be monitored. The nominal geometry has the following dimensions, which refer to figure 1(a), and a model of this geometry in SIMION is displayed as figure 5:

Dimension	Length
L_1	10mm
L_2	5mm
s_0	$L_1/2$
d_o	40mm
d_i	10mm
T	2mm
D	1m

Table 1. Nominal geometry dimensions

The distance between the hexapole and the center of the plates is 25mm. The orientation of the hexapole with respect to the flight path is a degree-of-freedom of this system. Two orientations were investigated, the one shown in figure 5, which will be referred to as the standard orientation, and the orientation if the hexapole were rotated by 30° about its axis. The deductions that lead to this choice of nominal geometry are summarized in appendix B.1.

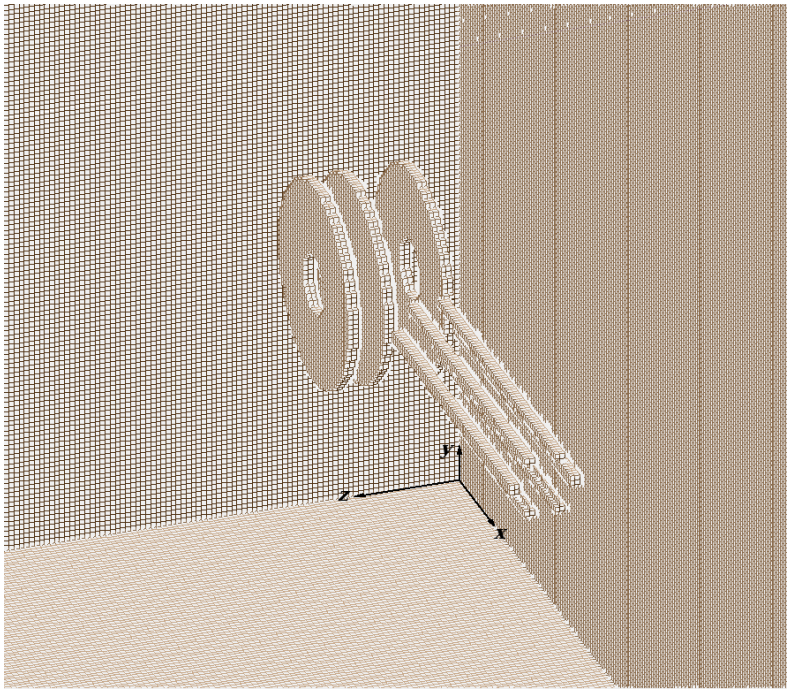

Figure 5. SIMION model of nominal geometry

For most runs, the voltage on the lower plate (V_1) and the upper plate (V_3) were kept at 1000V and 0V, respectively. These voltages were chosen to keep the order of magnitude of the accelerating field similar to the field produced by the hexapole, which had its poles at ±2500V. Much higher plate voltages could be used to reduce the turn-around-time effect, which limits the resolution of "hot" ions; however, doubling the voltage would have the undesirable effect of reducing, the shortest arrival time into the sub-μs range if the flight path is constrained to less than a meter.

From this point forward, references to axes will correspond to those seen in figure 5. Unless

otherwise stated, the grid density used in the simulations was 1mm/gu.[2]

3.2 Generating Ions

The nominal ionization volume was a rectangular polygon with dimensions $\Delta x \times \Delta y \times \Delta z \rightarrow$ 5mm $\times$ 0.1mm $\times$ 0.1mm; its centre matched the centre point between the middle and lower plates as displayed by figures 6(a) and 6(b).

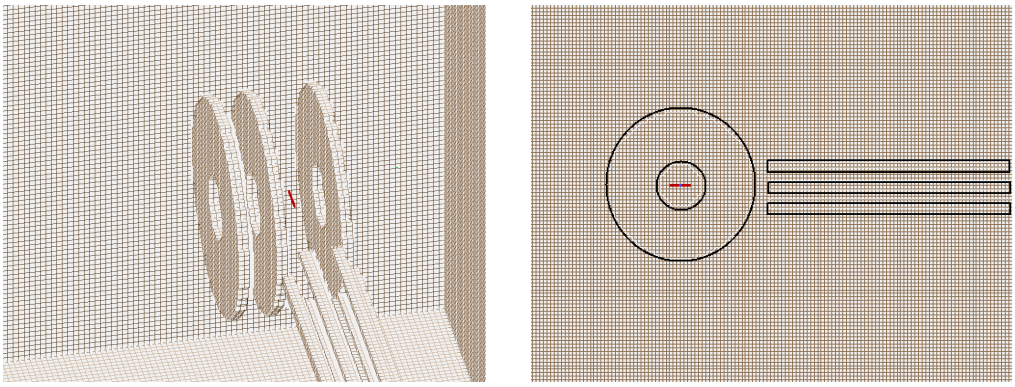

(a) Isometric (b) XY

Figure 6. Two views of the ions (red) in the nominal ionization volume

The 5mm dimension was estimated based on the maximum attainable MOT size while the 0.1mm dimensions were based on a typical ionization beam's diameter (8). Further information concerning initial conditions and the orientation of the volume with respect to the hexapole can be found in appendix B.3.

3.3 Distortion due to the Hexapole

3.3.1 Background

Obstacle Description While mass resolution is perhaps the most important performance parameter in most TOF-MSs, the transmission rate is an equally important parameter in this design. The hexapole destroys the axial symmetry of the electric field used to accelerate the ions and causes the ions to be deflected off the plates' axis undesirably as they travel through the drift region.

Proposed Solutions Three, independent solutions were considered to improve the axial symmetry of the accelerating electric field:

1. Remove the hole from the lower plate electrode to increase electrode surface area
2. Use square plates instead of circular plates to increase electrode surface area
3. Design a shield to isolate the drift region from the hexapole

[2]While this is a relatively course grid density and circular apertures are represented as jagged polygons, a short investigation into the effect of increasing grid density verified 1mm/gu would be sufficient for this design.

3.3.2 Test & Measurments

To determine the portion of the flight path most influenced by the hexapole, the x component of the electric field (E_x) was used as a quantitative measure. The y component of the electric field (E_y) in the ionization volume varied over a much smaller range because the extent of the ionization volume in that direction was only 100μm. The quantity created to gauge any improvements made to field asymmetries by shielding or geometry changes was $E_{asym} = E_x|_{99,100,z} - E_x|_{101,100,z}$. In these runs, the SIMION defined volume was $200\text{mm} \times 200\text{mm} \times 1000\text{mm}$ so that the ionization volume's centre point was $(x, y, z) \rightarrow (100\text{mm}, 100\text{mm}, 50\text{mm})$. For consistency, the lower, middle and upper plates voltages were $1000\text{V}, 650\text{V}$ and 0V, respectively, for all geometries. All ions were given zero kinetic energy at $t = 0$.

A simulation without the hexpole was performed to ensure that the ideal case produced ideal results. Following that investigation, the misdirection caused by the hexapole in the nominal geometry was considered. In summary, the hexapole introduces a substanial asymmetry, which is more pronounced in the drift region than originally expected. After travelling approximately 1m, the average ion position moved $\sim$ 6mm off its intended flight path. The results of these simulations can also be found in appendix C.1.1 and C.1.2, respectively. An illustration of the unwanted deflection from the plates' axis is displayed in figure 7.

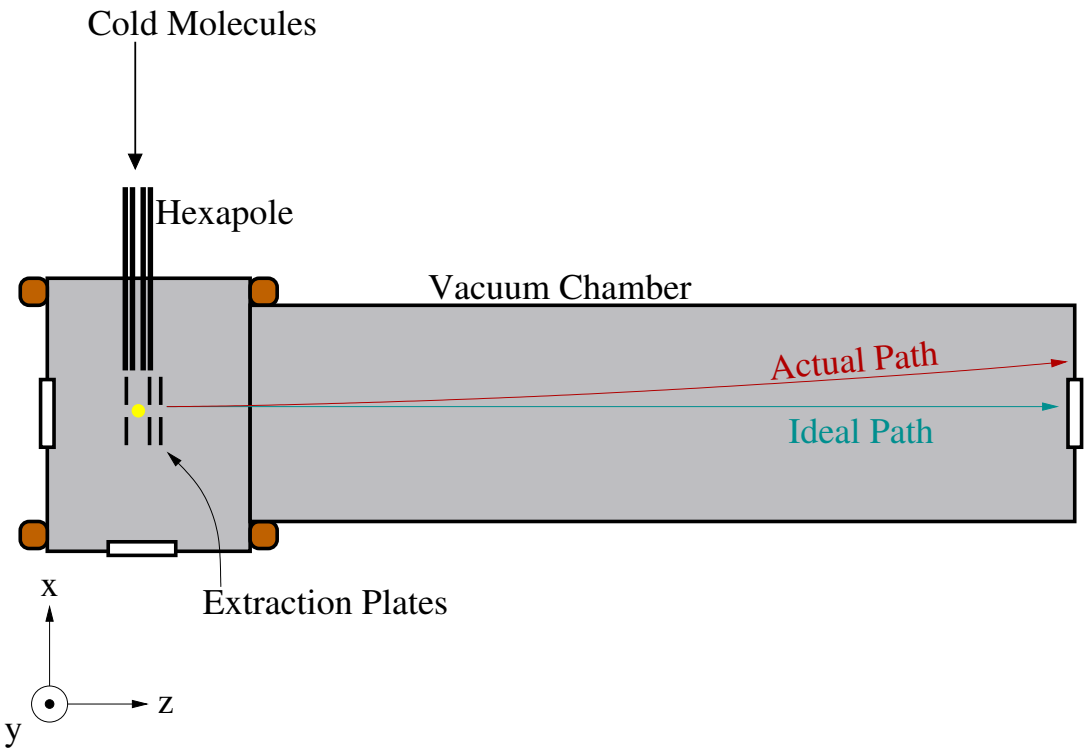

Figure 7. Unwanted deflection due to hexapole's close proximity to the ion flight path

To investigate the first solution, the hole was removed from the lower plate. The details of this simulation can be found in appendix C.1.3. The results show that removing the hole does not provide a significantly more symmetric electric field to outweigh the losses in trapping efficiency brought about by a solid lower plate(2).

The second attempt at improving field homogeneity was through the use of square plates. This simulation's results can be found in appendix C.1.4. The improvements that this offered

were more significant compared to removing the hole in the lower plate and since there were not any forseeable drawbacks of using sqaure plates, the decision to incorporate this solution into the final design was made.

The results of a complete drift shield formed by an 'infinitely' large upper plate can be found in C.1.5. This solution showed the most promise by correcting the ion path 5× more effectively than the other two solutions. A number of methods were considered for implementing the complete drift shield. The solution chosen was to surround the flight path by a tubular, grounded shield. Effectively, it would be a mesh surrounding the ions for the initial portion of the drift length. An illustration of this solution is displayed in figure 8.

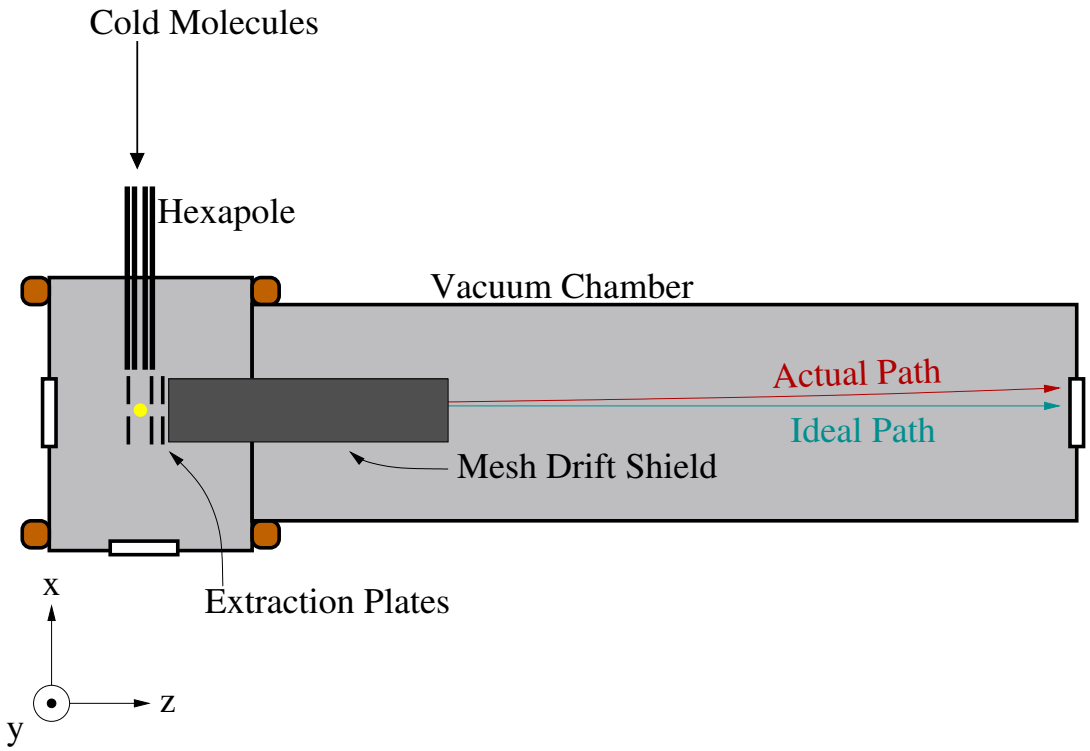

Figure 8. Implementation of a tubular drift shield solution to reduce negative effects due to the hexapole.

3.4 Extraction Plate Focusing

3.4.1 Background

Obstacle Description The extraction plates must as aperature lenses. An extremely diverging ion beam results from a voltage configuration that moves the space focus into the last half of the drift tube (see figure 55); this result magnifies the drops in performance caused by any following ion optical elements.

Proposed Solution At this point, the decision to include a mesh drift shield had been made. Giving the shield the added task of acting as a cylindrical electrostatic lens was proposed to "straighten" the ion trajectories upon entry into the drift region. Any electric fields that exchange an ion's energy between its lateral directions and its flight path direction are likely to reduce resolution. This solution was approached with some skepticism since R_0 was already

very close to the resolution performance goal. In figure 9, a light optics analogy displays the role of the Einzel lens.

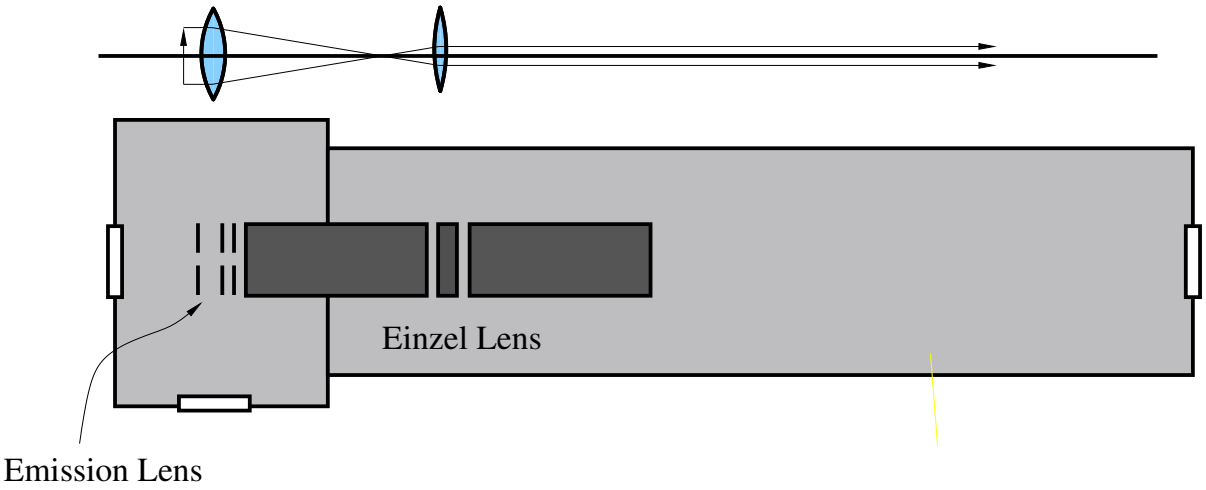

Figure 9. Optical analogy of the Einzel lens's role in correcting the extraction plate focusing. Three aperature lenses act as an emission lens (9).

3.4.2 Tests/Measurements

An Einzel lens, as described in appendix F.2, does not permanently alter the kinetic energy of the ions; it simply alters their path. If the focus of the Einzel lens matches the position of the extraction plate focus, the rays should leave the lens parallel to the optical axis (ie. plates' axis).

If the detector were to lie somewhere beyond $z = 700$mm, then one can estimate that the voltage on the middle plate (V_2) will be no less than ~ 825V; the extraction plate voltage will focus the ions to some point less than $z = 100$mm.

By inspecting a plot of the relevant middle plate voltages (see figure 10), it was deduced that the ions will be focused within the first 35mm of the drift region; this includes a buffer for ions with "hot" initial conditions, which would focus further down the drift tube.

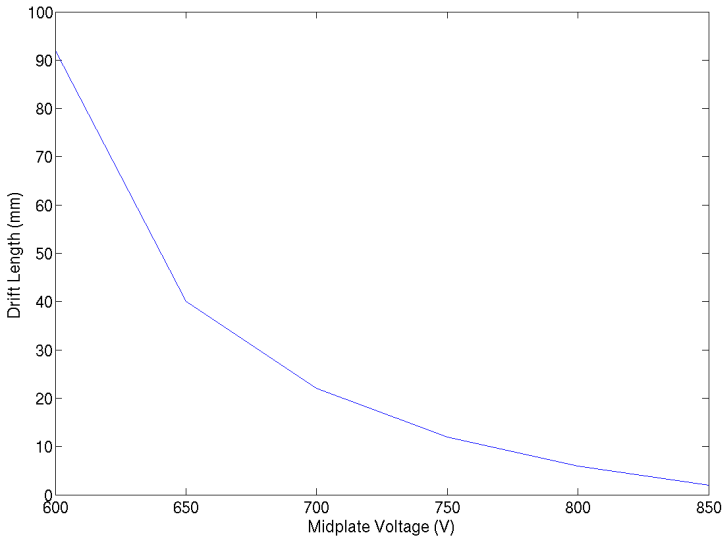

Figure 10. Extraction plate focal length for various middle plate voltages

Following the rule of thumb that a lens should be designed to have a filling factor no greater than 50% (10), the middle plane of the lens was placed 87mm from the upper extraction plate. The inner diameter of the lens was restricted to a minimum size of 40mm so that very large MOT beams could pass unimpeded. From (11), the geometry with $g/D = 0.1$ and $A/D = 0.5$ was chosen because its focal properties did not differ significantly from those presented for $g/D = 0.1$, $A/D = 1.0$; spherical aberration for the two lenses was not significantly different either. The choice of operating mode for the lens to be used in all following simulations is discussed in appendix C.3.2.

3.5 Deflection Plates

3.5.1 Background

Obstacle Description To keep the plates' axis completely open for MOT lasers, the ions would need to be detected off this axis.[3]

Proposed Solution Use parallel plates to deflect the ions through some small angle ($5° - 20°$) as they exit the Einzel lens.

3.5.2 Tests/Measurements

According to (12) and (13), temporal dispersion would come as a result of ions entering the parallel plates at different potential energies. Figure 11 provides a visual assessment of the influence of parallel plates on a collimated beam of ions.

[3] Actually, microchannel plate detectors can be made with small apertures in their centre, which would allow the detector to remain centred on the plates' axis. This solution would involve more complicated ion optics than a parallel plate deflector, so it was not pursued.

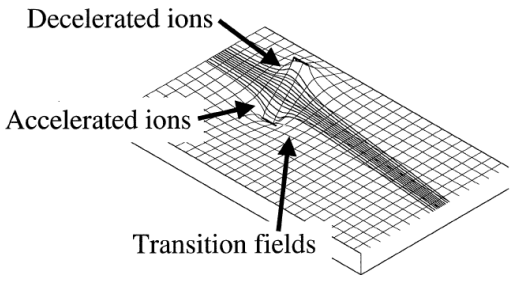

Figure 11. Potential energy surface of 2D parallel plate model displaying the distortion in the flight path of ions due to the fringe fields (13). This is assuming that the plate voltages are centred around 0V and the ions are entering the plates from a region that is a 0V.

To first order, the difference in transit time of a beam depending at what height it enters the plates is given by (12),

$$\Delta t = \sqrt{\frac{m}{2eU_o}}\frac{Vl}{2dU_o}x, \tag{5}$$

where x is the height measured from the plane halfway between the plates, V is the voltage across the plates (centred about $V = 0$), d is the plates' separation, m is the mass of the ions and U_o is the kinetic energy they have upon entering the plates. From equation 5, it was initially deduced that the length over which the bending takes place, does not impact resolution.[4] Given the ionization volume's compact y and z dimensions, the ions must be deflected by plates that lie in $x-z$ planes so that the difference in voltage across the y dimension of the cloud is minimized.

According to equation 5, the isochronous surface of the ions will be rotated by the parallel plates; further details about calculating the rotation angle can be found in section F.3. This means that the detector's surface can be oriented in a predictable way to reduce the dispersion caused by the parallel plates. A sample calculation was performed to estimate the benefit of rotating the detector's surface for two orientations (see section B.4).[5] The result suggests that for a deflection of $\sim 15°$, the poorer detector orientation will broaden the flight times by 3.494ns while the more favourable orientation will broaden the signal by 1.873ns; this applies to the heaviest mass to be analyzed by the system, 100amu. For the lightest mass, 1amu, the broadening in both cases is a factor of 10 smaller. With a resolution goal of 200, this improvement is relatively small, $\sim 5\%$. The only foreseeable drawbacks of this design choice is that the transmission efficiency of the grid on the ion detector will be worsened by approximately 4%, which is fairly insignificant compared to the geometric ionization efficiency of the system.

Conclusions A microchannel plate detector was chosen for this system, which can ordered pre-mounted to a conflat flange. The flange should be mounted to the vacuum system using the improved orientation as seen in appendix B.4.

The deflector plate separation was set at 40mm to allow large MOT beams to pass by unimpeded. The planned deflection angle was set at 15° so that the detector could have a

[4]For ideal plates this is true, however, a number of short runs flying a limited number of ions using different length parallel plates suggested that the less gradual the bend, the worse it is on resolution.

[5]To verify this would actually require a significant amount of manipulation in SIMION so the decision of how to orient the detectors face had to be based on a rough calculation due to time constraints.

reasonably large diameter ($\sim$ 40mm) without interfering with the MOT lasers. The plates' length was set at 100mm to keep the overall system compact[6].

3.6 Final Geometry

Figure 12 corresponds to the layout of electrodes in the simulations performed under realistic conditions. Drawings with more details on the dimensions of individual components can be found in appendix B.5. The purpose of this design was not to provide detailed mechanical drawings from which the ion optics could be constructed. Rather, the purpose was to illustrate a preliminary set of electrode dimensions that meet performance objectives. No attempt was made to design the supporting structure for the electrodes.

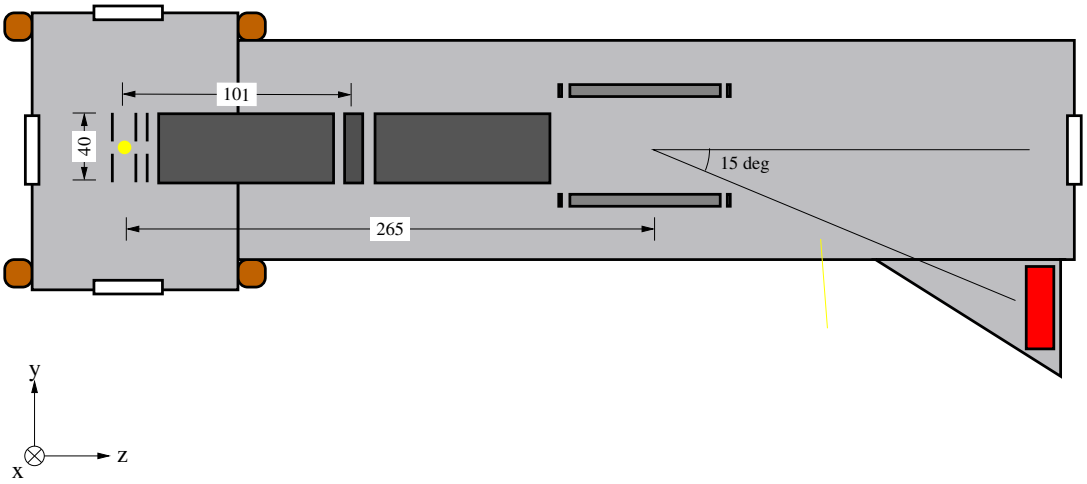

Figure 12. Final geometry with key dimensions highlighted

3.7 Realistic Conditions

3.7.1 Background

All simulations conducted were done to support the choices made in setting the electrode geometry. Ultimately, the robustness of the design needed to be tested.

One simulation examined the decrease in resolution caused by ionizing molecules outside of the nominal ionization volume. It showed that ions along the ionization laser's path and inside a volume centred on the extraction plates' axis with $\Delta x = \pm 7$mm will be pulled through the middle plate's aperture; all other ions will hit electrodes. Of the extra ions that are successfully collected, the percentage that actually impinge on the detector is 9.4%. The transmission efficiency for ions within the nominal volume was 100%. Further details on this simulation can be found in appendix C.4.

[6]Field terminators are located 4mm from the ends of the plates. Field terminators were used for the reasons described in appendix F.3

3.7.2 Wide Ionization Beam

Simulations have always modelled the ionization volume made by a laser with a waist diameter of 0.1mm. If ion yields need to be increased after the MOT has been made as large as possible, the only option left will be to increase the ionization volume by using a beam with a larger diameter. Three simulations were conducted using ionization volumes with x dimensions of 3, 4 and 5mm. The ions were heavy (100amu) and were given a starting temperature of 1K. The resolution (R_{SD}) as a function of drift length is displayed as figure 13.

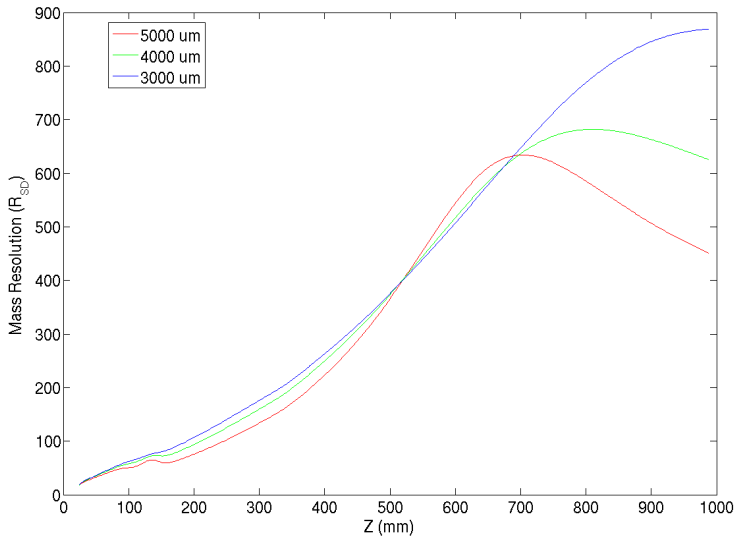

Figure 13. Resolution over entire drift length modelling an ionization laser with a diameter of 0.2mm with various x dimensions. Drift length start: $z = 34$mm; voltage configuration: $V_1 = 1000$V, $V_2 = 900$V, $V_3 = 0$V, $V_{def} = \pm 94.3$V; ionization volumes (3): $\Delta x = 3, 4, 5$mm, $\Delta y = \Delta z = 0.2$mm.

Conclusions The three curves display the robust nature of this TOF-MS. Increasing the diameter of the ionization laser still provides adequate mass resolution for cold, heavy molecules using the largest MOT diameter (5mm).[7] The space focus appears to be sensitive to transverse ionization volume width. Fortunately, as the transverse extent decreases, the space focus moves further away from the extraction plates; thus it could be adjusted back to the detector's plane by reducing the middle plate voltage.

3.7.3 Laser Misalignment

Laser misalignment could result in a twisting of the rectangular volume about the z-axis and increase the temporal dispersion due to the parallel plate deflector. Assuming 3^o to be the largest angular misalignment, runs were completed with (i) a perfectly aligned ionization laser and (ii) the same volume rotated by 3^o. In both runs, the extraction plate voltage configuration was $V_1 = 1000$V, $V_2 = 900$V and $V_3 = 0$V and the ions were deflected by approximately 15^o with deflection plate voltages (V_{def}) of ± 94.3V. Figure 14 displays the resolution for each run as a function of drift length.

[7] Investigation of the TOF histograms confirms that R_{SD} accurately represents R_{50} to within 5% at the space focus.

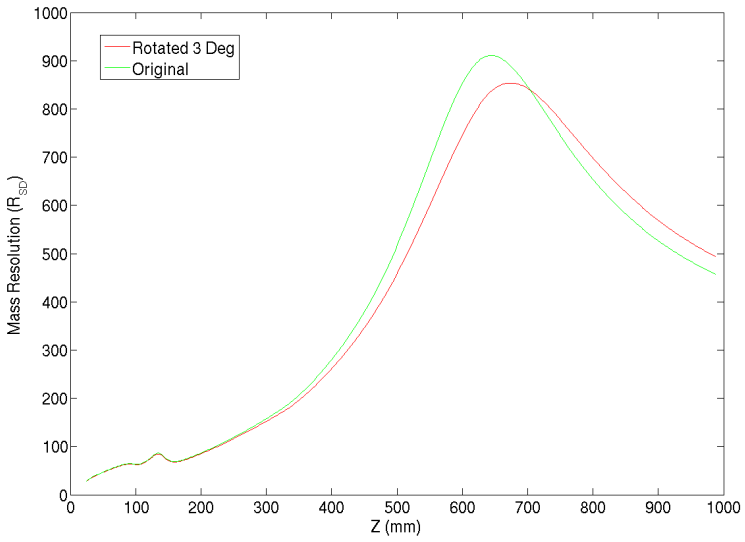

Figure 14. Mass resolution over the entire drift region comparing 0° with 3° of ionization laser misalignment. Drift length start: $z = 34$mm; voltage configuration: $V_1 = 1000$V, $V_2 = 900$V, $V_3 = 0$V, $V_{def} = \pm 94.3$V; ionization volumes: nominal.

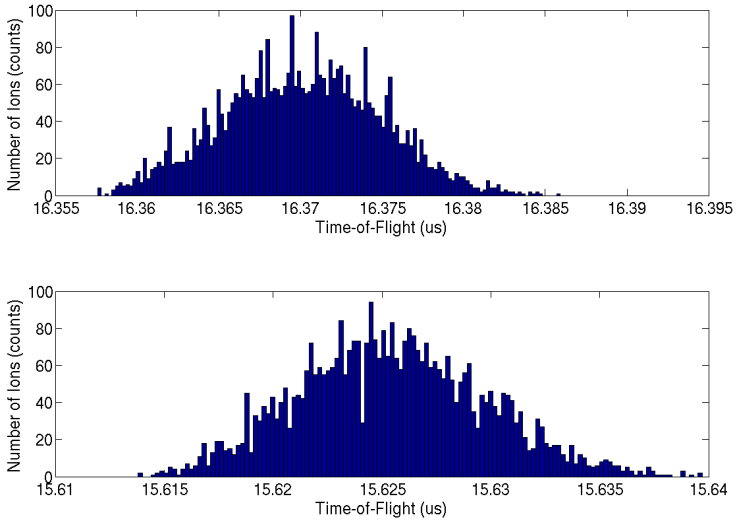

Figure 15. TOF histogram at the space focus for rotated (top) and original (bottom) ionization volume.

Conclusion The space focus has shifted and the maximum resolution has decreased, but in general, even with a slight misalignment, the TOF-MS meets the performance goal when operated at the space focus. As well, the transmission efficiency was 100% for both runs. Inspection of the TOF histogram at the space focus confirmed that R_{SD} was within 2% of R_{50} (see figure 15). Although 3° of misalignment could be viewed as an overestimate of what is generally achieved in an optical system, the result at the space focus of the red curve was used to assess the final geometry's mass resolution performance.

3.7.4 Hot and Cold Products

The largest and smallest masses to be analyzed in this system were assumed to be 100amu and 1amu. All runs have involved large masses with 'slow' initial velocity conditions. If a reaction produces light molecules along with heavy molecules, the light molecules will have much higher initial velocities, which could impact transmission efficiency and will definitely impact resolution. As a first attempt at modelling this scenario, an actual chemical reaction was considered,[8]

$$\mathrm{Li} + \mathrm{OH} \rightarrow \mathrm{LiO} + \mathrm{H} + \Delta H. \tag{6}$$

The assumptions used to determine a reasonable upper limit on the velocity distribution of hydrogen can be found in appendix C.4.2. With a voltage configuration of $V_1 = 1000\mathrm{V}$, $V_2 = 875\mathrm{V}$ and $V_3 = 0\mathrm{V}$ and deflection plates set at $\pm 93\mathrm{V}$ for approximately 15^o of deflection, a run with 4000 ions was completed with mass resolution results displayed in figure 16. The transmission rate was 100%; however, the resolution significantly decreased.

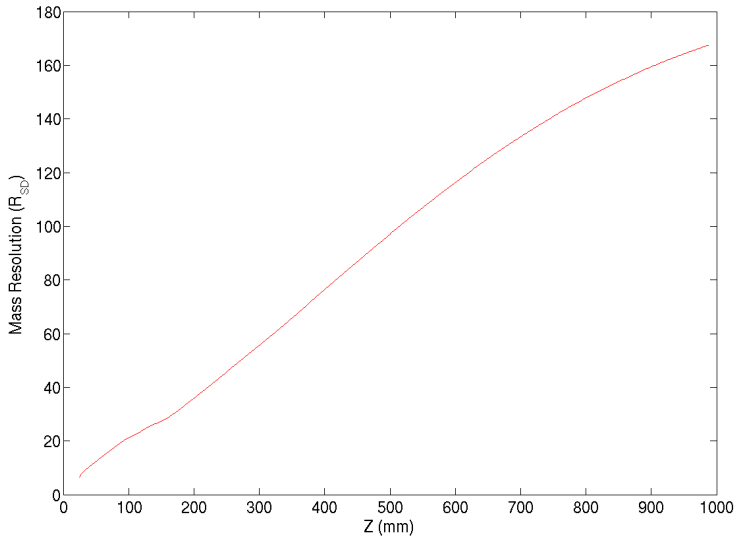

Figure 16. Mass resolution of hydrogen product from Li + OH reaction. Drift length start: $z = 34\mathrm{mm}$; voltage configuration: $V_1 = 1000\mathrm{V}$, $V_2 = 875\mathrm{V}$, $V_3 = 0\mathrm{V}$, $V_{def} = \pm 93\mathrm{V}$; ionization volume: nominal.

Conclusion Even under conditions not representative of the worst case scenario, the mass resolution of a light, hot atom could not meet the mass resolution performance objective. This significant decrease in resolution is attributable to the turn-around-effect, which has a negligible impact on cold ions. For the purpose of assessing the design's ability to meet its resolution goal, this result was used. Two other runs were completed, involving cold, heavy molecules as well as a hot, light atoms. Both simulations were not based on a particular reaction like the above case.

[8] After calculating the reaction's enthalpy, it was realized that this reaction was endothermic ($\Delta H = 47.12\mathrm{kJ/mol}$ (14)), thus not representing the worst possible scenario, which would be an exothermic reaction. With velocity of hydrogen still quite high in this reaction, it was used as a simulation candidate. The purpose of this simulation was to see how diminished the mass resolution would become when extremely products were considered.

The details of these simulations with more extreme initial conditions can be found in sections C.4.3.

3.8 Drawbacks in Resolution

Signal broadening will occur for a number of reasons so as to decrease the mass resolution of the system. The main sources of broadening are described in section B.6 and summarized in table 2.

Table 2. Additional sources of broadening

Broadening Source		σ^1(ns)
Detector surface jitter	$(\sigma_{surface})$	< 0.001
Laser pulse width	(σ_{laser})	2
Detector impulse response	$(\sigma_{detector})$	1
DAQ synchronization jitter	(σ_{DAQ})	0.015
Space charge effect[2]	(σ_{SC})	0.1
Residual gas collisions[3]	(σ_{gas})	negligible

[1] Gaussian distribution FWHM
[2] Assuming linear relationship between ion number and broadening
[3] Assuming vacuum better than 1×10^{-8}torr

There are two sources of broadening that disinguish themselves with FWHM greater than or equal to a nanosecond. For the purpose of calculation, only these broadening sources were considered. All simulations under realistic conditions did not take into account the impact of the magnetic field because of the unreasonable increase in computational time. It was assumed that it could accurately be accounted for by multiplying the temporal widths by a constant fraction, determined to be 1.136 (see appendix C.2).

Assuming all significant contributions to the temporal width are independent and can be represented by Gaussian probability distributions, the following equation can be used to estimate the final peak shape (6),

$$\sigma_T^2 = \left(\frac{\partial T}{\partial s}\right)^2 \sigma_s^2 + \left(\frac{\partial T}{\partial u}\right)^2 \sigma_u^2 + \sigma_{detector}^2 + \sigma_{laser}^2 \tag{7}$$

where σ_T is the FHWM of the signal measured by the data acquistion system, the first two terms on the RHS of equation 7 constitute the FWHM as determined by SIMION. For a heavy mass, 100amu, at 1K in an anti-Helmholtz magnetic field ($\frac{dB_z}{dz} = 10$Gcm) with laser misalignmnet, the TOF-MS will have a σ_T of 11.11ns corresponding to a drop in resolution from 854 (see figure 14) to 737, which is well above the resolution goal.

For a light mass, 1amu, at 2725K in an anti-Helmholtz magnetic field ($\frac{dB_z}{dz} = 10$G/cm) with laser misalignment, the TOF-MS will have a σ_T of 11.6ns corresponding to a drop from 172 to 86, which is far below the performance goal. However, this result does not mean the TOF-MS will not operate satisfactorily. If a peak corresponding to a mass of 2amu is present, the two peaks will be clearly discernible according to the definition of resolution.

4 Budget

The goal of maintaining the cost of the TOF-MS under $\$100,000$ was derived from the cost that typical mass spectrometers with similar resolving powers can be purchased for today. After receiving a quote for a linear TOF-MS from ComStock, Inc, it became clear that the costs of certain items of the system described in this report should not be included to provide a fair comparison. Two budgets can be seen below, table 3 taking into account the approximate value of the entire system and table 4, which only accounts for the components directly associated with the mass spectrometer. A more detailed breakdown of the costs can be found in appendix B.8.

Table 3. Entire Budget

Component Type	Cost ($)
Vacuum	23,680
Loader	8,700
Optics	11,250
Magnet	4,500
Electronics	19,430
Total	67,560

Table 4. TOF-MS Budget

Component Type	Cost ($)
Vacuum	23,680
Electronics	19,430
Total	43,110

5 Summary

This design investigated and overcame many obstacles that would worsen the performance of a TOF-MS used in conjunction with a high voltage hexapole and a cold atom trap. The main issues addressed by the design include:

1. inhomogeneities in the extraction plate region and drift region due to the close proximity of a HV hexapole
2. ion beam divergence due to extraction plates with uncovered apertures
3. off axis ion detection for sufficient optical access

The solutions came in the form of added complexity to the otherwise simple design of a Wiley-McLaren TOF-MS. Inhomogeneities in the extraction field were mitigated by the use of square plates and a mesh drift shield; the resulting flight path was approximately $5\times$ closer to the intended flight path. Lensing due the extraction plates was compensated for by giving the

drift shield the added purpose of acting as an Einzel lens. The optical access of the MOT lasers was guaranteed by introducing parallel deflection plates to move the ion detector off the normal flight axis. It was determined through simulations of a typical anti-Helmholtz magnetic field, that the electromagnet would not need to be switched to achieve a reasonable mass resolution performance.

The series of simulations performed under more realistic operating conditions showed that the transmission efficiency would be approximately 100% for molecules starting in the nominal ionization volume. The resolution objective, however, was not met for all initial ion conditions. More specifically, the case in which hydrogen was flown starting at 2725K, yielded a mass resolution of 86. However, the system would still perform adequately with this mass resolution for hydrogen since the mass resolution needed to discern hydrogen from the next largest mass is 1. The mass resolution goal was met and far exceeded for heavy, cold molecules; taking into account additional broadening neglected in SIMION™simulations, the mass resolution was 737.

The budget goal of $100,000 was quite easily met with the approximate budget estimated at $43,110.

6 Future Work

One question that remains somewhat unanswered is the resolution gain provided by rotating the detector surface with respect to the ions' flight path. SIMION™could be used to estimate this benefit and more accurately weigh the pros and cons of implementing it. While an estimate of the detection limit was calculated in appendix B.7 to determine the overall feasibility of the apparatus to study ultracold chemistry, a more in-depth analysis of the yield from typical chemical reactions should be performed.

References

[1] Roman V Krems. Molecular physics - set for collision course. *Nature Physics*, 3(2):77–78, 2007.

[2] Kirk Madison. private communication, 2009.

[3] B Friedrich and J M Doylei. Why are cold molecules so hot? *CHEMPHYSCHEM*, 10(4): 604–623, 2009.

[4] D Lee, S Cho, S G Lee, and S Kim. Designing points of a single-particle mass spectrometer in terms of aerosol focusing and ion loss. *Journal of the Korean Physical Society*, 49(1, Part 1):370–375, 2006.

[5] W C Wiley and I H McLaren. Time-of-flight mass spectrometer with improved resolution. *Review of Scientific Instruments*, 26(12):1150–1157, 1955.

[6] M Guilhaus. Principles and instrumentation in time-of-flight mass spectrometry - physical and instrumental concepts. *Journal of Mass Spectrometry*, 30(11):1519–1532, 1995.

[7] R C Watson. Laser-ionization time-of-flight mass spectrometry of high molecular mass inorganic complexes. Master's thesis, Virginia Polytechnic Institute and State University, 1997.

[8] Taka Momose. private communication, 2009.

[9] Helmut Liebl. *Applied Charge Particle Optics*. Springer, 2008.

[10] John H Moore, Christopher C Davis, and Michael A Coplan. *Building Scientific Apparatus, A Practical Guide to Design and Construction*. Westview Press, second edition, 1989.

[11] A Adams and F H Read. Electrostatic cylinder lenses ii. 3 element einzel lenses. *Journal of Physics E-Scientific Instruments*, 5(2):150–&, 1972.

[12] Thomas Dresch. Mass resolution by angular alignment of the ion detector conversion surface in time-of-flight mass spectrometers with electrostatic steering deflectors. US Patent 5,654,544, 1997.

[13] D A Dahl, A D Appelhans, and M B Ward. A modular ion beam deflector. *International Journal of Mass Spectrometry*, 189(1):47–51, 1999.

[14] M W Chase Jr, C A Davies, J R Downey Jr, D J Frurip, R A McDonald, and A N Syverud. Janaf thermochemical tables. *Jounal of Physical Chemistry*, 14, 1985.

[15] Christopher J Foot. *Atomic Physics*. Oxford University Press, 2005.

[16] Bastian Schuster. Ultracold li and rb atoms in a magneto-optical trap. Master's thesis, University of British Columbia, 2007.

[17] Todd P Meyrath. Electromagnet design basics for cold atom experiments, August 2004. URL http://george.ph.utexas.edu/~{}meyrath/informal/.

[18] J Schoser, A Batar, R Low, V Schweikhard, A Grabowski, Y B Ovchinnikov, and T Pfau. Intense source of cold rb atoms from a pure two-dimensional magneto-optical trap. *Physical Review A*, 66(2), 2002.

[19] K Wendt, K Blaum, B A Bushaw, C Gruning, R Horn, G Huber, J V Kratz, P Kunz, P Muller, W Nortershauser, M Nunnemann, G Passler, A Schmitt, N Trautmann, and A Waldek. Recent developments in and applications of resonance ionization mass spectrometry. *Fresenius Journal of Analytical Chemistry*, 364(5):471–477, 1999.

[20] R G Berger. *Flavours and Fragrances: Chemsitry, Bioprocessing and Sustainability.* Springer, 2007.

[21] U Boesl, R Weinkauf, C Weickhrdt, and EW Schlag. Laser ion sources for time-of-flight mass spectrometry. *International Journal of Mass Spectrometry and Ion Process*, 131: 87–124, 1994.

[22] D M Lubman. *Laers and Mass Spectrometry.* Oxford University Press, 1990.

[23] Eric Vyskocil. Generation of cold pulsed molecular beams. Master's thesis, University of British Columbia, 2007.

[24] S D Kraft, J Mikosch, P Staanum, J Deiglmayr, J Lange, A Fioretti, R Wester, and M Weidemueller. A high-resolution time-of-flight mass spectrometer for the detection of ultracold molecules. *Applied Physics B-Lasers and Optics*, 89(4):453–457, 2007.

[25] J L Hanssen, E A Dakin, J J McClelland, and M Jacka. Using laser-cooled atoms as a focused ion beam source. *Journal Of Vacuum Science & Technology B*, 24(6, Sp. Iss. SI): 2907–2910, 2006.

[26] Hamamatsu Engineering Division. Mcp and mcp assembly selection guide. Technical report, Hamamatsu Corp, May 2009.

[27] D A Gedcke. How counting statistics and the adc sampling interval control mass accuracy in time-of-flight mass spectrometry. Technical Report AN61, ORTEC, July 2001.

[28] Jurgen H. Gross. *Mass Spectrometry, A Textbook.* Springer, first edition, 2004.

[29] A M Hudor. Fast electronics for time-of-flight measurements. *Review of Scientific Instruments*, 52(6):819–825, 1981.

[30] *Agilent Technologies InfiniiVision 6000 Series Oscilloscopes Data Sheet.* Agilent Technologies, July 2009.

[31] C Weickhardt, F Moritz, and J Grotemeyer. Time-of-flight mass spectrometry: State-of-the-art in chemical analysis and molecular science. *Mass Spectrometry Reviews*, 15(3): 139–162, 1996.

[32] M Guilhaus. Essential elements of time-of-flight mass spectrometry in combination with the inductively coupled plasma ion source. *Sprectrochimica Acta Part B-Atomic Spectroscopy*, 55(10):1511–1525, 2000.

[33] H Rimke, G Herrmann, M Mang, C Muhleck, J Riegel, P Sattelberger, N Trautmann, F Ames, H J Kluge, E W Otten, D Rehklau, W Ruster, and F Scheerer. Principles and analytical applications of resonane ionization mass-spectrometry. *Mikrochimica Acta*, 3 (3-6):223–230, 1989.

[34] U Boesl. Special feature: Tutorial - laser mass spectrometry for environmental and industrial chemical trace analysis. *Journal of Mass Spectrometry*, 35(3):289–304, 2000.

[35] J L Wiza. Micochannel plate detectors. *Nuclear Instruments & Methods*, 162(1-3):587–601, 1979.

[36] D W Koppenaal, C J Barinaga, M B Denton, R P Sperline, G M Hieftje, G D Schilling, F J Andrade, and J H Barnes. Ms detectors. *Analytical Chemistry*, 77(21):418A–427A, 2005.

[37] Edmond de Hoffmann and Vincent Stroobant. *Mass Spectrometry, Principles and Applications*. Wiley, third edition, 2007.

[38] H. Wollnik and H. Ewald. The influence of magnetic and electric fringing fields on the trajectories of charged particles. *Nuclear Instruments and Methods*, 36:193–104, 1965.

A Background

A.1 Magneto-optical Trapping

A.1.1 Principles

MOTs perform the task of spatially localizing and cooling particles by combining an anti-Helmholtz electromagnet with 3 pairs of orthogonal, counterpropagating laser beams as displayed in figure 17.

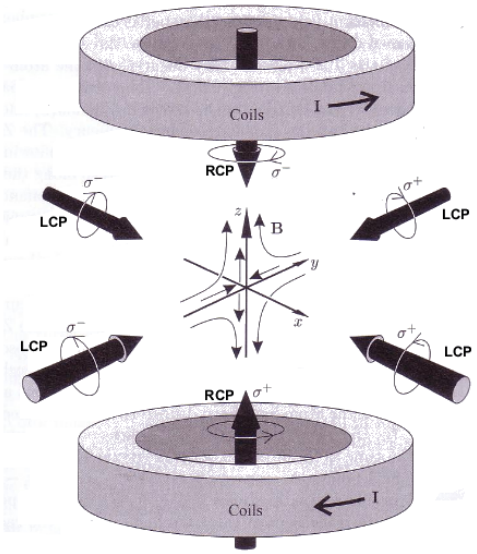

Figure 17. Conceptual layout of a magneto-optical trap (15)

The cooling process is facilitated by the restoring force that results when photons with a frequency that is negatively detuned from the particles' resonance frequency are scattered. For low laser intensities and particle velocities, the force is directly proportional to the velocity of the particle but in the opposite direction. To localize the particles, the restoring force must contain a spatial dependance, otherwise, the atoms will be cooled but diffuse outward. The spatial dependence of the force is provided by the electromagnet. Consider a two energy level system with a 3 times degenerate upper state as seen in figure 18. By introducing a magnetic field with a linear gradient, the degeneracy of the upper state is broken and there exist three upper states that an electron can be excited to, each with its own detuning from the lasers' frequency. If the particle travels in the $+z$-direction, the σ_- transition, which 'kicks' the particle back towards the origin, has a smaller detuning and preferentially occurs over the σ_+ transition, which 'kicks' the particle away from the origin. A similar process occurs when the particles travels in the $-z$-direction except that the σ_+ transition now provides the restoring force because it has the smaller detuning. Although the trapping mechanism has been described for the z-axis, a particle moving out of the symmetry plane of the coils will experience a magnetic field gradient, which leads to the Zeeman splitting of energy levels required for a spatially dependent restoring force(2).

MOTs are now a common instrument used by physicists for the study of atomic and molecular physics and very little innovative design is actually needed to produce a MOT. For this

reason, the experience of Dr. Madison was relied upon when making practical decisions concerning the MOT's performance in this design.

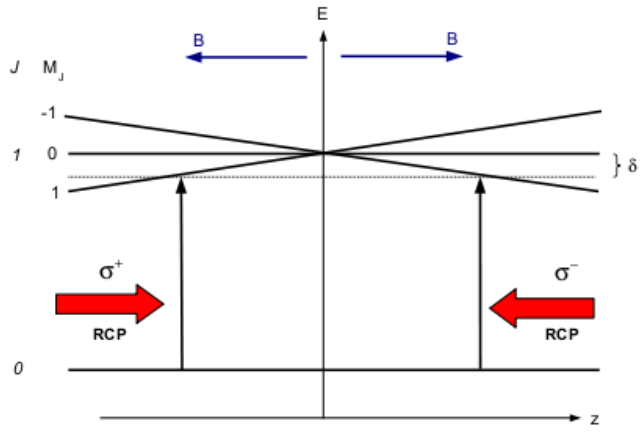

Figure 18. Spatial dependence of detuning leading to hooke's law restoring force (16). δ denotes detuning of an energy level from the laser photon's energy.

A.1.2 Anti-Helmholtz Coils

While providing an overview of how MOTs operate, it is clear that the magnetic field plays a crucial role in trapping atoms. Generally, magnetic fields are not seen in TOF-MSs and how an anti-Helmholtz field will impact the spectrometer's performance is unknown.

The anti-Helmholtz coil configuration produces a quadrupole magnetic field with the steepest linear gradient between them that two coils can generate. The coils and currents are oriented as seen in figure 19. The anti-Helmholtz constraint is described by the following conditions:

1. the coils lie in parallel planes separated by $2D = R$
2. the coils are axially aligned and have the same radius
3. the current in the coils runs in opposite directions as defined by the right hand rule

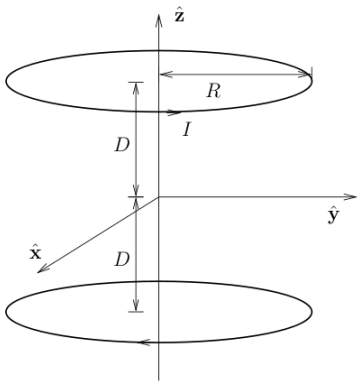

Figure 19. Anti-Helmholtz coils configuration ($R = 2D$) (17)

These constraints yield a maximum in the gradient of the magnetic field's $\hat{z}$ component at the origin (17). The analytic expressions for the magnetic field anywhere in space are given by (17):

$$\begin{aligned} B_z &= \frac{\mu I}{2\pi} \frac{1}{\sqrt{(R+\rho)^2+(z-D)^2}} \left[K(k^2) + \frac{R^2-\rho^2-(z-D)^2}{(R-\rho)^2+(z-D)^2} E(k^2) \right], \\ B_\rho &= \frac{\mu I}{2\pi} \frac{z-D}{\sqrt{(R+\rho)^2+(z-D)^2}} \left[-K(k^2) + \frac{R^2+\rho^2+(z-D)^2}{(R-\rho)^2+(z-D)^2} E(k^2) \right], \end{aligned} \tag{8}$$

where

$$k^2 = \frac{4R\rho}{(R+\rho)^2+(z-D)^2}, \tag{9}$$

and $K(k^2)$ and $E(k^2)$ are respectively the complete elliptic integrals of the first and second kind (17). [9] The first order term of the taylor expansions about the origin are generally used when calculating the magnetic field gradient along $\hat{\rho}$ and $\hat{z}$ (see equations 10 and 11). $\frac{\partial B_z}{\partial z}$ is the often quoted quantity describing the operating condition of the coils. Through experience, the optimal value has been found to lie in the vicinity of 10Gcm^{-1} (2).

$$B_z \simeq 3\mu I \frac{DR^2}{(D^2+R^2)^{5/2}} z \tag{10}$$

$$B_\rho \simeq \frac{3}{2}\mu I \frac{DR^2}{(D^2+R^2)^{5/2}} \rho \tag{11}$$

A.2 2D-MOT Loader

Based on the experience of Dr. Madison, a 2D-MOT system would be the best option for loading the main 3D-MOT. Other methods for loading a MOT exist; however, using these methods would result in an unacceptably large background pressure for a TOF-MS and significantlyconstrain the maximum atomic cloud diameter.

A 2D-MOT works under the same principles as a 3D-MOT but only uses 2 pairs of orthogonal lasers to localize particles in a plane, leaving the third dimension unconstrained. The result is a collimated, high flux jet of particles, which have been pre-cooled so that their average velocity is well below the capture velocity of the 3D-MOT. This method of loading is highly efficient and necessary to quickly load the 3D-MOT and generate large diameter cloud of trapped atoms. Effectively 100% of the atoms that make up the loading beam are trapped by the 3D-MOT. Atom densities of 10^{10}cm^{-3} and cloud diameters of $\sim$ 5mm have been achieved (2). With a flux of 10^{10}atoms/s (18), if the MOT was to be completely reloaded for each run to the maximum cloud size, this process would limit the overall repetition rate of the system to 1.9Hz. The losses due to ionization, atom-atom collisions and atom-molecule collisions are expected to be very small assuming a species selective ionization method is used. This makes it possible for the 3D-MOT to be loaded continuously, leading to a steady state density of nearly 10^{10}cm^{-3}. Using this arrangement, the loading process is not the rate determining step for the mass spectrometer.

[9] These equations, as they appear in (17), contain a sign error that was corrected when the magnetic field was modelled.

A.3 Resonant-enhanced Multiphoton Ionization

Resonance-enhanced multiphoton ionization (REMPI) is a commonly used in time-of-flight mass spectrometers when the selective ionization of a particular species is desired. As its name alludes, REMPI is the process of an atom or molecule absorbing multiple photons that are resonant with its electronic energy structure to excite an electron from a bound state to a continuum state. An important alternative method of moving an electron to a continuum state is through non-resonant multiphoton ionziation (NRMPI) , which also requires the absorption of multiple photons but does not involve a resonant intermediate energy level. Diagrams illustrating the two processes can be seen in figure 20.

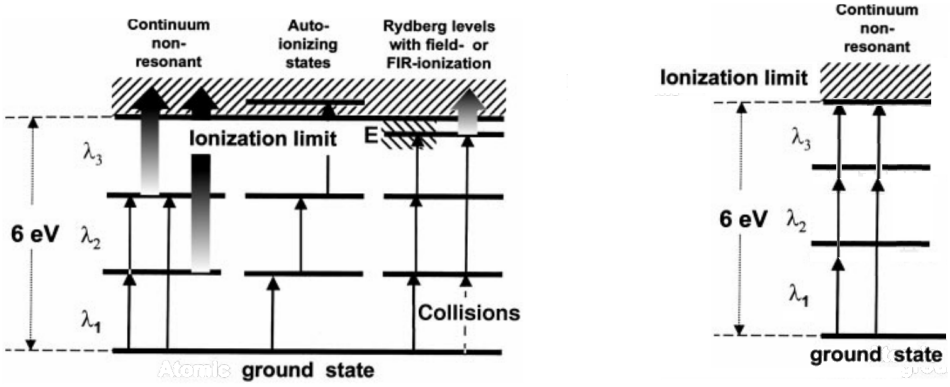

(a) REMPI (b) NRMPI

Figure 20. Laser ionization schemes. Adapted from (19).

With typical first ionization potentials near 6 eV, ultraviolet (UV) wavelengths are generally used. A strict requirement not to use vacuum ultraviolet (VUV) radiation was imposed because of the loss of species selectivity and the increased difficulty of coupling the radiation into the vacuum environment. The three main conditions that determine if REMPI is possible are (20),

1. The molecule must have a bound, excited state energy level that is resonant with the laser photons
2. The excited state has a lifetime long enough to absorb a second photon
3. The ionization energy of the molecule is lower than the combined energy of two laser photons

The qualities of REMPI that make it particularly amicable in this situation is its selectivity and lower laser power requirements. In the analysis of a trace component of a sample, REMPI is implemented because it allows for significantly enhanced ionization probabilities that would require orders of magnitude higher laser intensity with NRMPI. NRMPI is not selective and can result in a larger background signal (21). A typical REMPI ionization laser pulse is $1 - 5$ns long, has a waist intensity of $\sim 10^7 \mathrm{W/cm}^2$ and a waist diameter of ~ 0.1mm (8). Efficiencies are largely species dependent and can range from 1% to 100%.

Being able to operate at much lower laser intensities means that fragmentation is much less likely to occur. For this reason, REMPI is known as a "soft" method of ionization (21). NRMPI

provides uniform ionization efficiencies across all species but requires much higher photon fluxes. For example, for the NRMPI efficiency to be 100%, assuming a typical, two photon cross-section ($\sigma_1\sigma_2$) equal to 10^{-49}cm^4 and a pulse width of 4ns, a flux density of $5 \times 10^{28}\text{cm}^{-2}\text{s}^{-1}$ is required. This corresponds to $3 \times 10^{10}\text{W/cm}^2$ using $\lambda = 330\text{nm}$ (22). Even if REMPI is performed at intensities of 10^8W/cm^2, the NRMPI ionization efficiency of undesired species drops by approximately 4 orders of magnitude.

A.4 Ultracold Molecular Beam

The cold molecular beam system that this apparatus must adapt to was designed and built by Dr Taka Momose's group at UBC. The apparatus consists of a hexapole that is approximately a meter long with two 90^o bends as seen in figure 21; the TOF-MS would replace the RGA mass spectrometer.

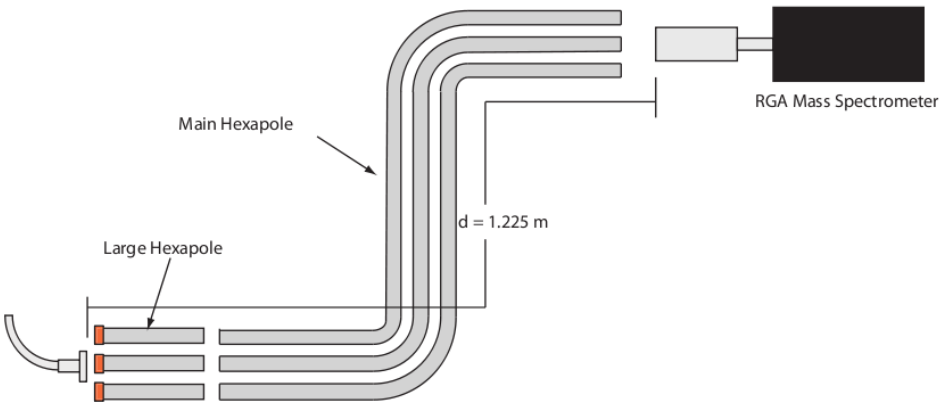

Figure 21. Hexapole assembly that currently guides molecules from the large hexapole to an RGA mass spectrometer (23)

There is essentially no const0raint on the species that can be guided and filtered by the hexapole. The velocity filtering process works based on the Stark shift of the molecules' energy levels, which provides a force only capable of constraining the molecules to the hexapole if their transverse and longitudinal velocities are small enough. The pulse repetition rate is 10Hz, which provides the ultimate limit on the repetition rate of the TOF-MS.

The dimensions of the hexapole are of key importance in determining the separation distance for the extraction plates in the TOF-MS. The hexapole is a perfect hexagon with 6mm between adjacent pole centres. Each pole is 2mm in diameter, which leaves a 4mm gap between adjacent poles (see figure 22). The diameter of the largest circle that can inscribe the interior of the hexapole is 8mm. The molecular beam will have an approximate outer diameter of this size as it enters the extraction plate region creating the constraint that the lower and middle plates must be separated by a minimum of 8mm.

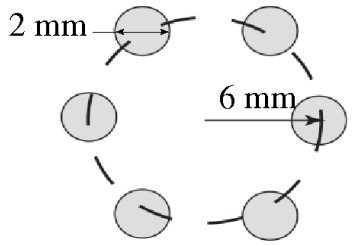

Figure 22. Hexapole geometry. Modified from (23).

The molecular beam can be focused a distance no further than 25mm from the hexapole's exit plane; this creates the constraint that the maximum distance the hexapole can be from the MOT's center is 25mm (8).

To accurately predict the reaction yields in this apparatus would require a quantum mechanical treatment of the reactions and would be greatly species dependent. Nevertheless, a prediction was still made and can be found in section B.7; it assumes that each pulse contains 10^9 molecules (8).

Due to miscommunication, all TOF-MS simulations were executed under the assumption that the main hexapole's operating voltages were ±2500V. In actuality, the hexapole's geometry requires ±5000V to operate efficiently; the diameter of the hexapole would need to be halved in order to operate at ±2500V. Much work had been completed under this incorrect assumption, so that for the remainder of the design, it was assumed that ±2500V was the correct voltage configuration.

B Miscellaneous

B.1 Nominal Geometry

Hexapole Proximity The largest allowable separation of the hexapole and the MOT is ∼ 25mm in order for the molecular beam's focus and the MOT to coincide. The closer the hexapole can be located to the trapped atoms, the more effective the molecular beam will react with them. However, the closer the hexapole is made, the more it deflects the extracted ions off their intended course. The hexapole was located the farthest allowable distance from the MOT atoms.

Aperture Sizes Many TOF-MSs use gridded extraction plates because grids allow ions to be transmitted with very high efficiencies (up to 95%). However, a MS combined with a MOT cannot use gridded plates because of the significant disruption they would cause to the MOT beams (24). The size of middle and upper apertures were constrained to being equal. The lower plate does not need to transmit ions but assuming the electrodes are opaque, it still needs to remain open for the optical access. However, if the electrodes were transparent, it could be feasible to close the hole in the lower plate in order to improve field homogeneity. How this could be accomplished is discussed in appendix B.2.

An upper bound on the diameter comes from field inhomogeneities caused by the hexapole. The larger the hole diameter, the larger the asymmetry in transverse electric field that is felt by the ions. A lower bound on the diameter is posed by the initial velocity of the resonantly ionized particles. In the end, 10mm holes were put in all three plates based on the experience of Dr. Momose. This size provides a sufficient opening for the largest ionization volume[10] to pass through.

Drift Length An upper limit of 1m was put on the drift length so that the apparatus remained reasonably compact.

Plate Separation To ensure all the molecules of the molecular beam are able to enter the extraction plates, the minimum separation is 8mm. This also acts as the maximum plate separation because the further the lower and middle plate are separated, the more the ions will feel the impact of the HV hexapole just outside the extraction region. s_0 was set to half of L_1 so that the molecular beam's axis would be centred between the lower and middle plates.

Plate Diameters Plate diameters are closely related to hexapole proximity, but can be treated as a separate DOF. For a given distance between the hexapole's exit plane and the MOT, the plate diameter can be any size but making it as large as possible is the most logical choice. The design is a balance between hexapole proximity and TOF performance. For a fixed proximity, the TOF performance will always improve as the plates are made larger. It is clear from other designs that circular plates are commonly used; however, intuition suggests that rectangular plates could offer better acceleration field properties, which is why they were examined in the case analyses.

B.2 Electrode Material Selection

The bottom plate in the three plate ion extraction system could be made into a solid electrode since indium tin oxide (ITO) coated quartz electrodes are transparent. ITO is a commonly used

[10] ∼ 5mm is the volume's largest dimension

optical coating with well understood properties.

In a three electrode geometry, the MOT beams that are collinear with the symmetry axis of the plates will pass through a differing number of ITO coatings, which could potentially shift the trapped atom. In the case of unbalanced beams, shim coils can be added that are in a Helmholtz configuration to the trapping location. They work by adding a small, uniform component to the magnetic field in the needed direction. MOTs can be accurately positioned to within 0.1mm (2).

If the ITO coatings have birefringent properties and alter the polarized trapping beams, this could inhibit the trap's ability to localize and cool atoms. However, when ITO is evaporated onto a substrate at an angle normal to the substrate's surface, the optical anisotropy is minimal leading to a coating exhibiting negligible birefringence. Only a single case could be found in which MOT lasers passed through substrates coated with ITO; the apparatus is that of Hanssen et al. (25) who built a novel ion source for focused-ion-beam applications. This case proves that any birefringence that is induced is negligible for MOT applications. What differs between the work of (25) and this design is the necessity for the MOT lasers to pass through multiple layers of ITO. Small tests performed by Dr. James Booth using the MOT he designed and ITO coated microscope slides confirm that atoms can be trapped efficiently through multiple layers of ITO.

B.3 Ion Generation

It was assumed that all ions were created at the same time, although in fact the ions would be created over a time approximately equal to the laser pulse's duration ($\sim 1 - 5$ns). This drawback in resolution was taken into account after the simulations were performed.

In certain instances, it was necessary to change various characteristics of the ions. The energy distribution of atoms in a MOT resembles a Maxwell-Boltzmann distribution (MBD) and Vyskocil (23) displayed that the velocity distribution of molecules exiting the hexapole was also a MBD. Without looking in detail at the dynamics of the atom-molecule interactions, it was assumed that atoms in the ionization volume could also be described by a MBD. The ions were randomly distributed within the ionization volume and unless otherwise stated, each run was made up of 4000 ions. Computational time was the factor limiting how many ions could be flown.

Figures 23(a), 23(b) and 23(c) are examples of the spatial distributions for a typical set of ions used in a simulation. Ideally, the distributions would be flat denoting the coordinates were chosen randomly. The coordinates of the ionization volume's centre in SIMION is $(x, y, z) \rightarrow (50\text{gu}, 50\text{gu}, 50\text{gu})$, which is why the position distributions are not centred about $(0, 0, 0)$. If simulations did not use these coordinates for the centre of the ionization volume, it has been specifically delineated.

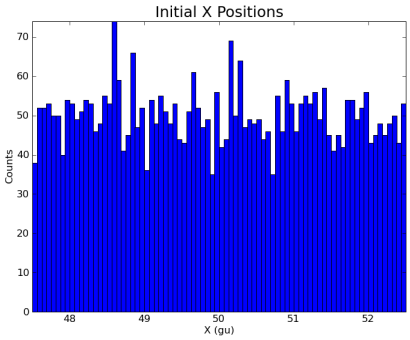

(a) Ion x coordinate distribution

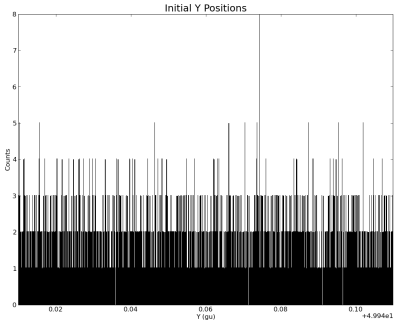

(b) Ion y coordinate distribution

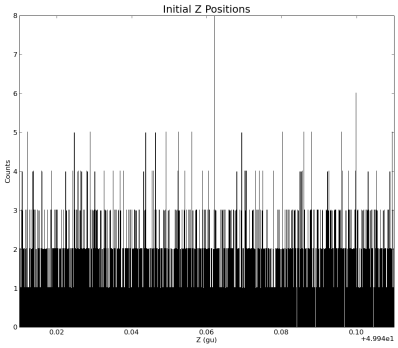

(c) Ion z coordinate distribution

Figure 23. Ionization volume position distributions

When ions were flown with a finite initial velocity, the direction of the initial velocity was randomized and the kinetic energy distribution was modeled with an MBD. Sample distributions of the azimuthal and elevation angles, which describe a velocity's direction, and of kinetic energy are displayed as figures 24(a), 24(b) and 24(c), respectively.

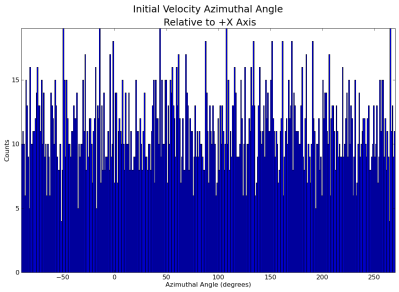

(a) Azimuthal angle distribution

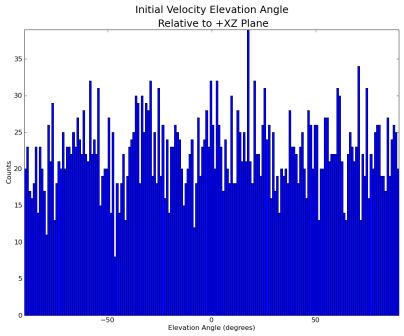

(b) Elevation angle distribution

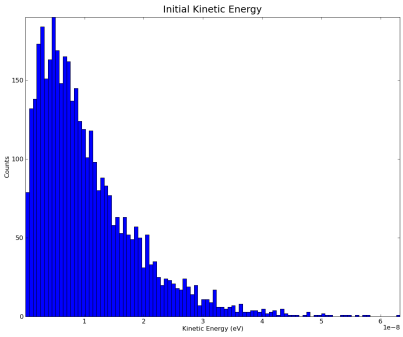

(c) Kinetic energy distribution ($T = 1\text{mK}$)

Figure 24. Ionization volume initial velocity and energy distributions

The orientation of the ionization volume was chosen in an attempt to maximize the probability of ionizing molecules. It could potentially result in the non-negligible ionization of reactant molecules thus causing a background signal. However, the unwanted ionization of reactant molecules would be limited to the focal volume of the laser and given that the ions follow a complicated path to the detector, the chance of the background ions reaching the detector would be significantly diminished (8). An attempt to verify this fact was investigated in appendix C.4.

B.4 Detector Orientation

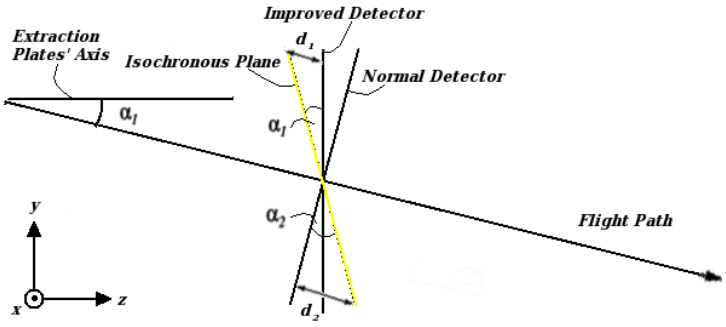

$$v = \sqrt{\frac{2eU_o}{m}}$$
$$\alpha_1 = 15°$$
$$\alpha_2 = 30°$$
$$d_1 = \frac{w}{2} \cdot \tan\theta_1$$
$$d_2 = \frac{w}{2} \cdot \sin\theta_2$$
$$\Delta t_1 = \frac{2d_1 \cdot \tan\theta_1}{\sqrt{\frac{2eU_o}{m}}}$$
$$\Delta t_2 = \frac{2d_2 \cdot \sin\theta_2}{\sqrt{\frac{2eU_o}{m}}}$$

Figure 25. Detector orientation geometries

Data from a run comparing a perpendicular deflector with a small angle deflector[11] was used to determine the width, w, (ie. length of the yellow line in figure 25) of the ions as they enter the deflection plates. Figure 26 displays the change in the standard deviation of the ions' y coodinates as they travel towards a detector at $z = 515$mm.

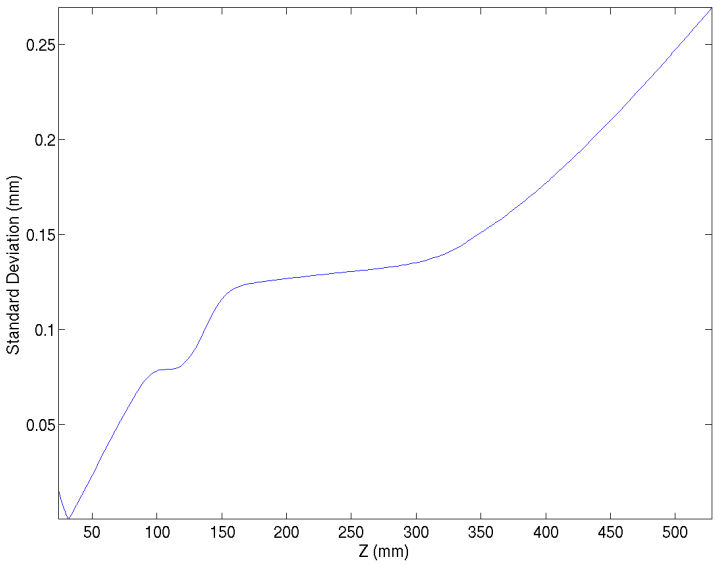

Figure 26. Standard deviation of ion cloud in $\hat{y}$ direction as a function of flight position. Drift region start: $z = 34$mm; deflector entrance: $z = 230$mm; voltage configuration: $V_1 = 1000$V, $V_2 = 900$V, $V_3 = 0$V, $V_{def} = \pm 94.3$V; ionization volume: nominal.

Assuming,

$$w = 2\sigma = 0.29\text{mm}, eV_o = 900\text{eV}, m = 100\text{amu},$$

[11] This simulation is not displayed in this report

then $\Delta t_1 = 3.494$ns and $\Delta t_2 = 1.873$ns. From equation 2 on page 2, one can derive,

$$\%\Delta R = 1 - \frac{\Delta t_o}{\Delta t_o + \Delta t_{def}},$$

where $\%\Delta R$ is the percent decrease in resolution as a result of the parallel plate deflector, Δt_o is the width of the flight time distribution without a parallel plate deflector and Δt_{def} is the width added by the deflector. For the favourable orientation of the detector, $\Delta t_{def} = \Delta t_1 = 1.873$ns and $\%\Delta R = 4.5\%$; for the normal orientation, $\Delta t_{def} = \Delta t_2 = 3.494$ns resulting in $\%\Delta R = 8.52\%$.

B.5 Final Geometry

B.5.1 Extraction Plates

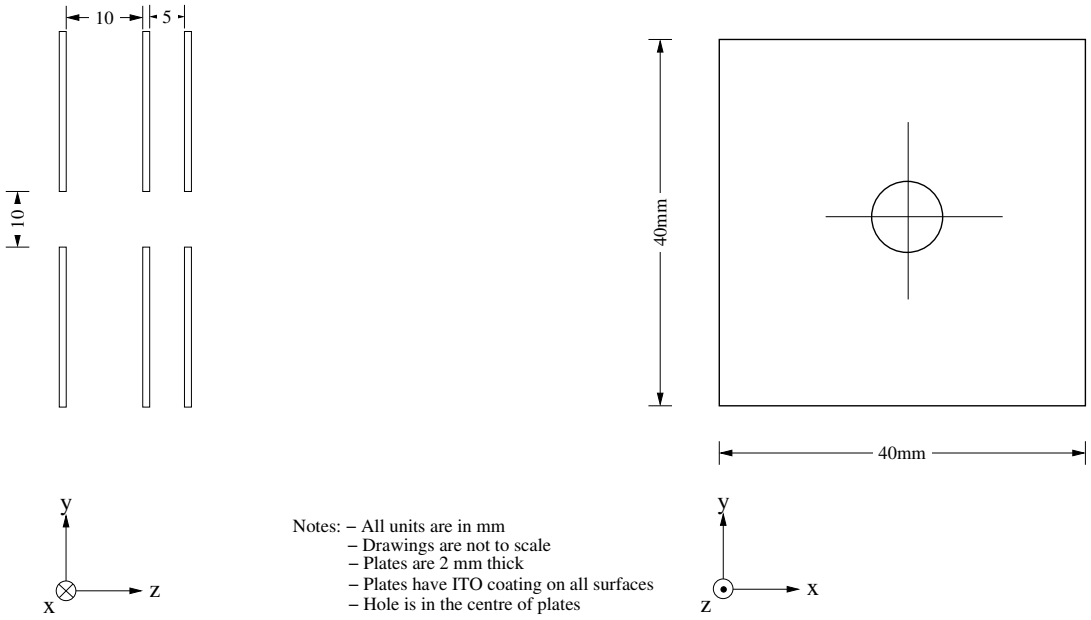

Figure 27. Extraction plate drawings

B.5.2 Einzel Lens

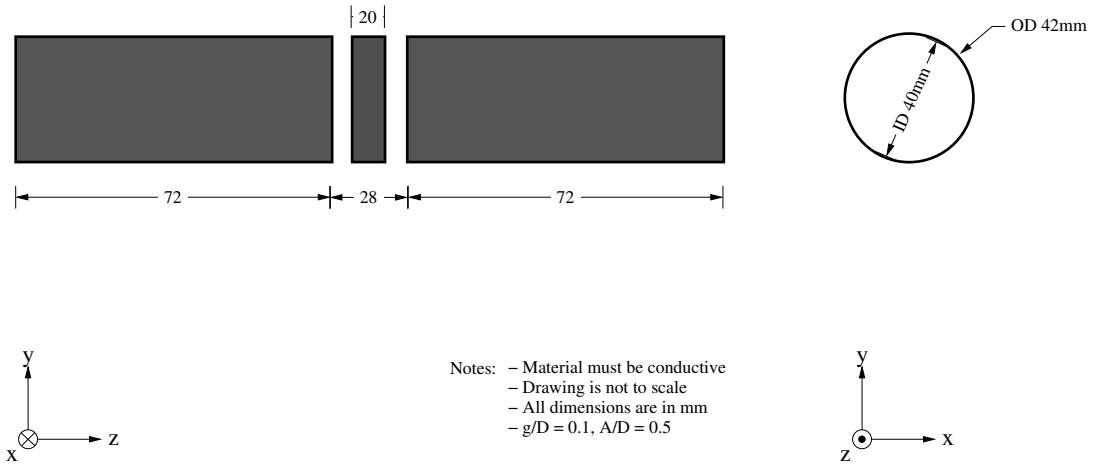

Figure 28. Einzel lens drawings

B.5.3 Deflection Plates

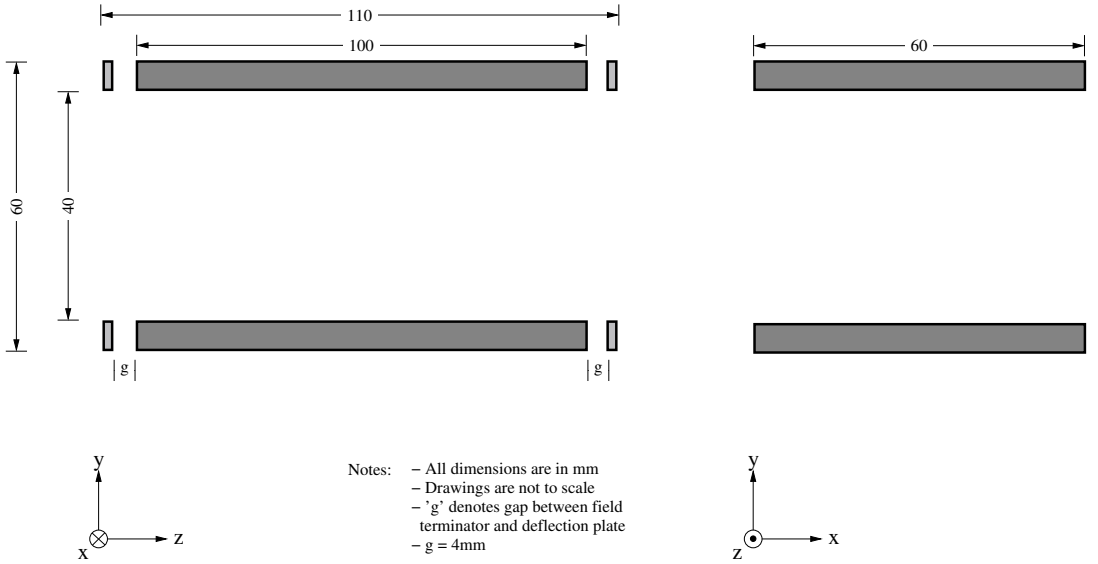

Figure 29. Deflection plate drawings

B.5.4 SIMION Model

The model of this geometry in SIMION™appears differently and can be found in appendix B.5. Reasons for the differences in appearance are due were due to RAM limitations SIMION™puts on the size of electrostatic potential arrays.

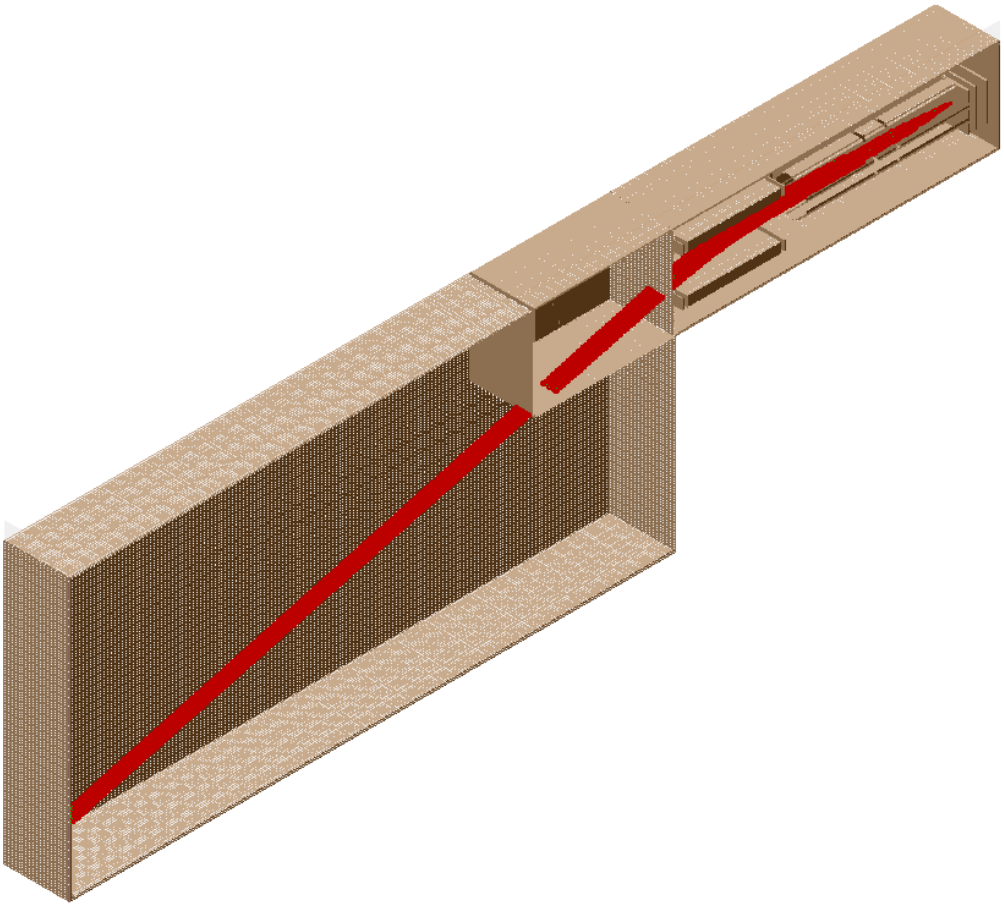

Figure 30. Isometric view of a cross section of the final geometry in SIMION. Red denotes ion flight paths.

B.6 Resolution Drawbacks

Signal broadening will occur for a number of reasons so as to decrease the mass resolution of the system from what was calculated in SIMION. The main sources of broadening are:

Detector Surface Jitter

This is problem seen if the surface of an eletron multiplier detectors is exposed to humid air for extend lengths of time. If this occurs, an MCP absorbs moisture and deforms. This leads to a jitter in arrival times since the MCP is no longer a planar surface. In general, this is not a concern if the proper handling and storage procedures dictated by the manufacturer are followed (26). There is also detector jitter due to the bias angle of a detector's channels to the flight path. This jitter would only be significant if the mass resolution were in the many thousands.

Impulse Response Broadening

The signal from an MCP responding to the repetitive impact of ions in a short burst will be the convolution of the true ion current with the detection system's impulse reponse. This result becomes more significant, the smaller the ion peak width. Since the detector's response is not a delta function, there is some degree of broadening brought about by the detector itself.

Assuming the impulse response can be represented by a gaussian ($\text{FWHM}_{impulse}$), that the inherent spread in arrival time due to finite ion cloud dimensions and velocities can be represented by a gaussian ($FWHM_{flight}$), the FWHM of the ouput signal is broadened by less than 12% if $FWHM_{flight} > 2FWHM_{impulse}$ (27).

As an example, assume that an MCP with $\text{FWHM}_{impulse} = 1\text{ns}$ impulse response uses an oscilloscope with sufficient bandwidth to not introduce additional broadening. A voltage configuration of 1000V, 900V and 0V, atomic hydrogen takes approximately 1.5μs to reach the detector using the geometry seen in figure 52. Had the hydrogen been at a much cooler temperature so that the resolution goal of 200 was achieved, the pulse width, FWHM_{flight} would have been,

$$\begin{aligned} \text{FWHM}_{flight} = \Delta t &= \frac{t_{avg}}{2R_{FWHM}} \\ &= \frac{1.5\mu\text{s}}{2(200)} \\ &= 3.75\text{ns}. \end{aligned} \tag{12}$$

The width of the digitized pulse would have been,

$$\text{FWHM}_{record} = \sqrt{\text{FWHM}_{flight}^2 + \text{FWHM}_{impulse}^2} = 3.88\text{ns}. \tag{13}$$

This would correspond to a drop in resolution of 7, to 193, which is 3.5%.

To ensure that the detection system's impulse response is as narrow in time as possible, broadening due to a low sampling rate must be avoided (28). The rule of thumb for determining the necessary bandwidth (Bw) for a pulse is given by (29),

$$\tau = \frac{0.35}{Bw}. \tag{14}$$

The rise time of the shortest pulse that could be expected in pulse counting mode is ~ 350ps, which means that circuit components must have a bandwidth at least this large. A bandwidth smaller than this for a single ion pulse would attenuate higher frequencies and broaden the pulse. Oscilloscopes that are capable of continuous sampling rates as high as 80Gsa/s are commerically available but such high sampling is unnecessary in this application. 2Gsa/s corresponds to sampling a signal once every 500ps, which corresponds to a FWHM/T_{sample} of 2. According to (27), this results in peak area and peak centroid uncertainties of approximately 1×10^{-3}%. This suggests that if 100 000 ions were contained in a pulse with a width of 2ns, then the lower limit on the uncertainty of this number would be ±1. This artificial circumstance could never be encountered with TOF-MS confirming 2Gsa/s is an adequate sampling rate.

Laser-Recording Synchronization

A typical LIMS triggering scheme involves a photodiode that is exposed to a small fraction of the laser light directed at it using a beam sampler. A line from the photodiode to the transient digitizer (in most cases this is an oscilloscope) acts as the external trigger. Depending on when the trigger pulse reaches the acceptance threshold with respect to the digitizer's internal clock, the synchronization of the ionization time with $t = 0$ as defined by the digitizer has some amount of jitter. A relatively inexpensive oscilloscope

with sufficient bandwidth ($\geq$ 1GHz) and sampling capabilities (2Gsa/s) has a trigger jitter of 15ps$_{\text{rms}}$ (30). If pulse widths are inherently are on the order of ns or tens of ns, this broadening effect can be ignored. Fast photodiodes have a width of $\sim$ 1ns and assuming that the jitter in its rise time is 10% of its width, then its contribution to broadening will be approximately a distribution with a width of approximately 100ps, which is relatively small.

Finite Ionization Time

In conjunction with the laser synchronization is the finite time over which ions are produced. The ionization laser is a significant source of broadening, limiting the arrival time distribution to the FWHM of the pulse. For a single hydrogen, which takes approximately 1.5μs, to travel to the detector (see figure 52(b)), this means

Space Charge Effect

None of the simulations took into account the space charge effect of the ion beam mainly because an accurate estimate of the expected current could not be established. According to (31), space charge effect can be quite significant with laser ionization sources. If 10^4 ions are produced by a beam with a waist of 0.1mm, a broadening of 10ns would be experienced. From a geometric standpoint, this system will not produce 10^4 ions per shot; in fact, 100 ions would seem exceptional. Space charge effect is very unlikely to cause significant broadening in this system.

Temperature Increasing the Turn-Around-Effect

The turn-around-effect is the spread in arrival time due to ions with initial velocities but in opposite directions (6). Ions with smaller masses which would be characterized with higher temperatures experience a much larger decrease in resolution. This was shown for the case of hydrogren in section 3.7. To reduce the turn-around-effect, the electric field strength in the region where the ion's are produced can be increased.

The turn-around-effect is the spread in arrival time due to ions with initial velocities but in opposite directions (6). Thus, ions with smaller masses which will be characterized with higher temperatures will experience a much larger decrease in resolution. This was shown for the case of hydrogren in section 3.7. To reduce the turn-around-effect, the electric field strength in the region where the ion's are produced can be increased. The temporal dispersion (Δt) due to the turn-around-effect is described by (32),

$$\Delta t = 2\frac{\sqrt{2mU_0}}{eE_1}, \tag{15}$$

where U_0 is the ion's initial kinetic energy, m is the ion's mass and E_1 is the electric field seen in figure 2. When trying to discern signal from light particles, the field can be increased while keeping the literal spatial focusing and space focus location the same by increasing the lower and middle plate voltage while keeping the ratio of the ratio E_2/E_1 the same. In general, the stronger E_1 is made, the worse the resolution is made at the space focus because the physical distribution of ion starting locations results in a larger distribution of kinetic energies after acceleration. Generally, the trade-off between compensating for source of dispersion while worsening another is optimized during operation. For a cloud of ions

Voltage Supply Stability The resolution limit due to ripple of the HV supply is generally not a constraint for most TOF-MS. The resolution is related to ripple by,

$$R = \Delta m/m = \Delta V/V, \tag{16}$$

based on equation 2 on page 2. Programmable HV supplies can be purchased with ripple regulation of 0.001% from Stanford Research Systems at a reasonable cost, which would limit resolution to 100,000. HV supply stability is not an issue that warrants concern with this system.

Construction Accuracy and Precision
Need to do some runs showing this!!!

Collision with Neutral Gas Molecules
Vacuum pressures below 1×10^{-8}torr are required for this system from the standpoint of trapping ability and for efficient operation of the hexapole Stark guide. The mean free path of a particle at 1×10^{-8}torr is $\sim$ 660m. This means that on average, if the flight length is 1m and 660 molecules are produced in each laser shot, then 1 molecule, on average will undergo a collision each run. In worse vacuum conditions and when many thousands of ions are generated in each run, broadening due to this would be more substantial; however, it is unlikely to pose a serious threat to mass resolution and transmission efficiency in this system.

B.7 Detection Limit Calculations

Rimke et al. (33) discuss their REMPI-TOF-MS system with a detection limit of less than 10^7 atoms per sample, meaning that the molecule, whose abundance was trying to measured could be accurately detected by the TOF-MS if the general sample contained more than 10^7atoms; the same approach was used to estimate the detection limit of this system. The following efficiencies are used in estimating the total system efficiency:

Table 5. Apparatus efficiencies

Type		Value (%)
Geometric efficiency	(ϵ_g)	4.6×10^{-6}
Ionization efficiency	(ϵ_i)	20
Transmission efficiency	(ϵ_t)	100
Detector efficiency	(ϵ_d)	43
Total efficiency[1]	(ϵ_{tot})	4.0×10^{-7}

[1] $\epsilon_{tot} = \epsilon_g \epsilon_i \epsilon_t \epsilon_d$

The geometric efficiency takes into account the fact that only a fraction of the molecular beam can interact with the MOT atoms and only a fraction of those molecules can be ionized by a focused laser. The ionization efficency is the probability of a resonance-enhanced electronic transition to a continuum state. The transmission efficiency refers to how effectively the TOF-MS can transport ions from the desired ionization volume to the detector and the detector efficiency is self explanatory. The calculation of the values in table 5 are described below in more detail. If each molecular beam pulse contains 10^9 molecules, then 4 molecules should be

the average number seen in the collected mass spectrum, which is on the border of detectability. This number depends very strongly on the assumptions made in the following calculations, which are questionable in their accuracy.

B.7.1 Geometric Efficiency

According to (23), the temperature of a molecular beam of CaF_2 produced by the hexapole velocity filter has a most probable velocity (v_p) of 4.5m/s, which corresponds to a MBD with a temperature of 70mK. It was assumed that a molecule with a mass of 100amu would have the same v_p.

$$\begin{aligned} T &= \frac{m v_p^2}{2k_B} \\ &= \frac{(100\text{amu})(4.5\text{ms}^{-1})}{2(1.38 \times 10^{-23}\text{m}^2\text{kgs}^{-2}\text{K}^{-1})} \\ &\simeq 70\text{mK} \end{aligned} \tag{17}$$

The following assumptions were made about the geometry of the MOT and molecular beam in order to continue:

1. the MOT can be modelled as a cube with a volume of 4mm^3
2. the molecular beam's cross section has a uniform density of molecules
3. the molecular beam can be focused from its nominal 8mm diameter down to a diameter of 2mm (8).[12]

The best time to ionize the product molecules is when the highest density of them are in the MOT region interacting with the trapped atoms. At that time, the longitudinal velocity of molecules entering the MOT volume is $v = v_p - 4.5\text{mm/s}$ and the longitudinal volocity of molecules leaving the MOT volume is $v = v_p + 4.5\text{mm/s}$. The fraction of reactant molecules that can result in product molecules in the MOT volume can be approximated; the fraction is 0.00184.[13]

The total number of molecules in a beam is a dependent on how it is produced at the hexapole's source but according to Momose (8), 10^9 molecules is a reasonable estimate. The number of reactant molecules within the MOT volume when the ionization beam is delivered is found by,

$$N = 10^9\text{molecules} \times 0.00184 = 1.84 \times 10^6\text{molecules} \tag{18}$$

For the purpose of this calculation, a reaction efficiency of 1% was used, which reduces the number of product molecules in the ionizable region to ~ 1840.[14] A Gaussian beam with

[12] Of course, focusing will not result in a collimated beam but a beam with a focus $\sim$ 25mm from the hexapole's face with some amount of divergence. However, for this order of magnitude estimate, it is assumed that the average diameter of the molecular beam is 2mm as it passes through the MOT.

[13] This value was obtained by integration of an MBD ($T = 70\text{mK}$) over $v_p - 4.5\text{mm/s} \leq v \leq v_p + 4.5\text{mm/s}$.

[14] A molecular dynamics simulation would be needed to determine an accurate reaction cross section. This cross section truly is a crucial value for determining whether or not the number of molecules produced by each ionization pulse will be within the detection limits of the spectrometer and is why the detection limit goal was replaced.

$\lambda = 250$nm that is focused to a waist radius of 50μm has a focal volume (ie. twice the Rayleigh range), which is given by,

$$\begin{aligned} z_R &= \frac{\pi w_o^2}{\lambda} \\ &= \frac{\pi(5 \times 10^{-5}\text{m})^2}{250 \times 10^{-9}\text{m}} \\ &= 0.0314\text{m} \simeq 3\text{cm} \end{aligned} \tag{19}$$

Since the Rayleigh range is much larger than the MOT's diameter (in this case cube's side length), all molecules within the ionization beam's diameter ($\sim 100\mu$m), that are also within the MOT will be ionized. Of course, product molecules outside of the MOT's volume will also be ionized but it is assumed that those ions would not be reach the detector. The ratio of the ionization volume to the molecular beam's volume is,

$$\begin{aligned} \frac{V_{ionization}}{V_{beam}} &= \frac{\pi r_{laser}^2 l}{\pi r_{mbeam}^2 l} \\ &= \frac{(50\mu\text{m})^2}{(1\text{mm})^2} \\ &= 2.5 \times 10^{-3} \end{aligned} \tag{20}$$

Combining all geometric efficiency components results in an efficiency of $4.6 \times 10^{-6}\%$.

B.7.2 Ionization Efficiency

Rimke et al. (33) predicted that their ionization efficiency was 50% and that the percentage of atoms in the ground state was 40%.

In reference (34), the sample calculation of a very conservative estimate for ionization efficiency of 2-photon REMPI was performed; the resulting efficiency was 10%. This value assumed the following:

1. the absorption cross section for the first step (σ_1) was 10^{-18}cm^2
2. the absorption cross section for the second step (σ_2) was 10^{-17}cm^2
3. the first absorption step was not saturated
4. the laser pulse intensity (I) was 10^7W/cm^2
5. the laser pulse duration (τ) was 10ns

Boesl (34) states that the efficiency can be signficantly better if σ_1 were higher, which it typically is compared to the value used in the calculation and if a higher intensity laser is used to saturate the first transition.

Given the conservative nature of the ionization efficiency calculation of (34), the ionization efficiency in (33) (50%) was be used in all estimates. Also, the proportion of molecules in the

ground state is not easily predicted without a very in depth analysis, so the value used in (33) (40%) was also adopted. In general, there is the possibility of fragmentation due to NRMPI; however, the probabilty of this occuring is so small when lasers are operated at laser intensities meant for REMPI, that this process can be neglected. The end result is an ionization efficiency of 20%.

B.7.3 Transmission Efficiency

Simulations performed under realistic operating conditons with the mass spectrometer (see section 3.7) confirm that this TOF-MS has a transmission rate of 100%.

B.7.4 Detector Efficiency

The detector was assumed to be a microchannel plate for the reasons outlined in section D. The literature on microchannel plate provides a large range of possible efficiencies because of many influential factors. For simplicity, the physical area of the channels making up the detector was used as the detection efficiency, which lies within the range of acceptable values outlined in (35). A typical value for the open area ratio is $\sim 50\%$ (26).

For this design, since the detector's surface is to be rotated by $\sim 15^\circ$ with respect to the impinging ions' flight path, the transmission efficiency of the grid will also decrease from $\sim 90\%$ to 86%. Thus the overall detector efficiency is $\sim 43\%$.

B.8 Budget

B.8.1 3D-MOT Vacuum

Table 6. 3D-MOT Vacuum Budget

Component/Description	Supplier	Quantity	Cost ($)
Source chamber			
- Spherical Hexagon (CF63)	KP[1]	1	1,000
Drift chamber			
- Custom	KL[2]	1	1,250
Bayard Alpert vacuum gauge	KL	1	1,350
Ion pump[3]			
- Vaclon Plus 150	V[4]	1	4,000
Scroll pump	U[5]	1	6,450
Fused Silica viewports			
- UV rated	M[6]	8	1,600
Electrical Feedthrough			
- Multi pin, high voltage	M	1	550
In-Vacuum mounting supplies			
- eV Parts Kit			
- 2 groove grabbers			
- mesh	KP	1	780
Fused silica substrates			
- ITO coated	Z[7]	3	500
Microchannel Plate Detector			
- chevron configuration			
- flange mounted with BNC connectors	J[8]	1	6,200
Subtotal			**23,680**

[1] Kimball Physics, Inc
[2] Kurt J. Lesker Company
[3] See appendix E
[4] Varian, Inc
[5] ULVAC Technologies
[6] MPF, Inc
[7] ZC & R Coatings for Optics, Inc
[8] Jordan TOF, Inc

B.8.2 Optics [15]

Table 7. Optical Components Budget

Component/Description	Supplier	Quantity	Cost ($)
Optics table	T[1]	1	1,000
Mirrors	T	20	5,000
λ/4 plates	T	12	3,000
Lenses	T	4	600
Beam sampler	T	1	250
Photodiode - GaP (UV sensitive)	T	1	250
Pyroelectric meter	T	1	1,150
Subtotal			**11,250**

[1] Thor Labs, Ltd

B.8.3 2D-MOT Loader

Table 8. 2D-MOT loader budget

Component/Description	Supplier	Quantity	Cost ($)
Coils & Driver	G[1]	1	1000
Vacuum chamber - Highly customized	K[2]	1	2000
Windows - Custom AR Coating	M[3]	4	2000
Dispenser - built in house	n/a	1	500
Elements	A[4]	n/a	200
Ion Pump - 40l/s	V[5]	1	3000
Subtotal			**8,700**

[1] GMW Associates
[2] Kurt J. Lesker Company
[3] MPF, Inc
[4] Alfa Aesar
[5] Varian, Inc

[15] all optical component mounting assemblies can be manufactuered in house

B.8.4 3D-MOT Magnet

Table 9. Magnets Budget

Component/Description	Supplier	Quantity	Cost ($)
3D-MOT *Coils*			
- wire			
- support stand		1	500
Current supply	G[1]	1	4,000
Subtotal			**4,500**

[1] GMW Associates

B.8.5 TOF-MS Electronics and Data Acquisition System

Table 10. TOF-MS electronics and data acquisition system budget

Component/Description	Supplier	Quantity	Cost ($)
High voltage power supplies			
- PS325 (±2.5kV)	S[1]	3	6,000
HV cabling and connectors	U[2]	n/a	400
Oscilloscope and cabling			
- Infiniivision 6102A	A[2]	1	13,030
Subtotal			**19,430**
Total			**67,560**

[1] Stanford Research Systems, Inc
[2] UBC Stores
[3] Agilent Technologies

C Additional Case Analyses

C.1 Hexapole Distortion

C.1.1 Simplest Geometry (No Hexapole)

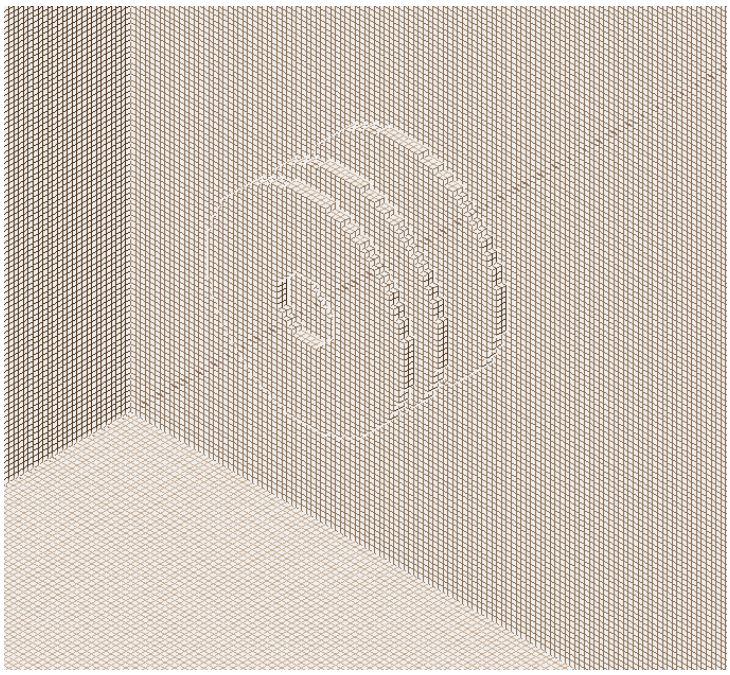

Geometry	
Lower Plate (z)	44mm
Middle Plate (z)	56mm
Upper Plate (z)	63mm
Inner diameter	10mm
Outer diameter	40mm
Hexapole	None

Voltages	
Lower Plate (V_1)	1000V
Middle Plate (V_2)	650V
Upper Plate (V_3)	0V

Proof that the ideal geometry was in fact ideal needed to be established. Without a hexapole, one would expect no asymmetry in E_x and would expect the average x position of the ions to lie along $x = 100$mm (ie. the ion cloud stays centred on the plates' axis). While the first statement was verified as true in figure 31, figure 32 displays a systematic error that was only realized after completing all other runs.

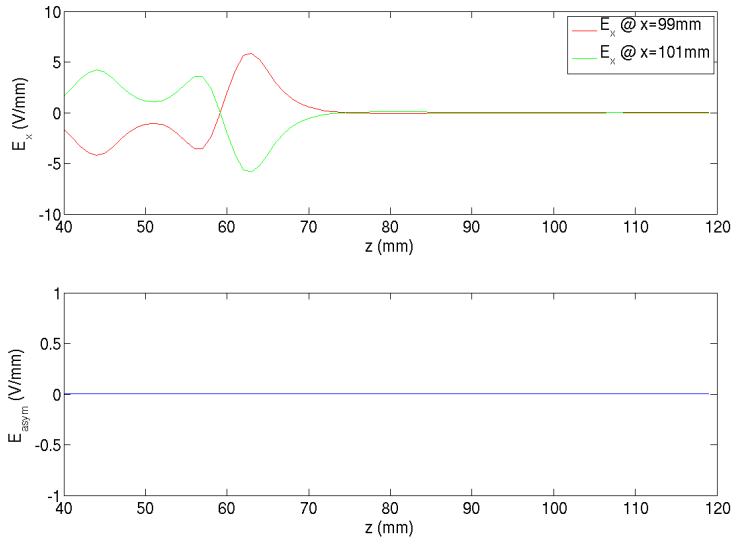

Figure 31. E_x asymmetry plot without hexapole present

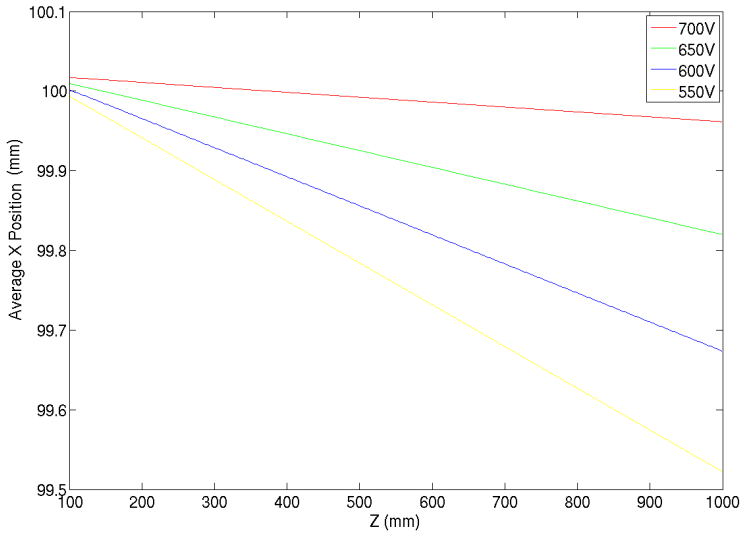

Figure 32. Average x position of ion image at various drift lengths without the hexapole's presence. The results for various middle plate voltages are displayed; drift region start: $z = 64$mm

Conclusions The divergence of the ion image from the ideal ($x = 100$mm) is the result of poor sampling; only 4000 ions are randomly distributed in the ionization volume. When viewing all other runs, this must be kept in mind so as to not under estimate the effect of the hexapole.

C.1.2 Nominal Geometry

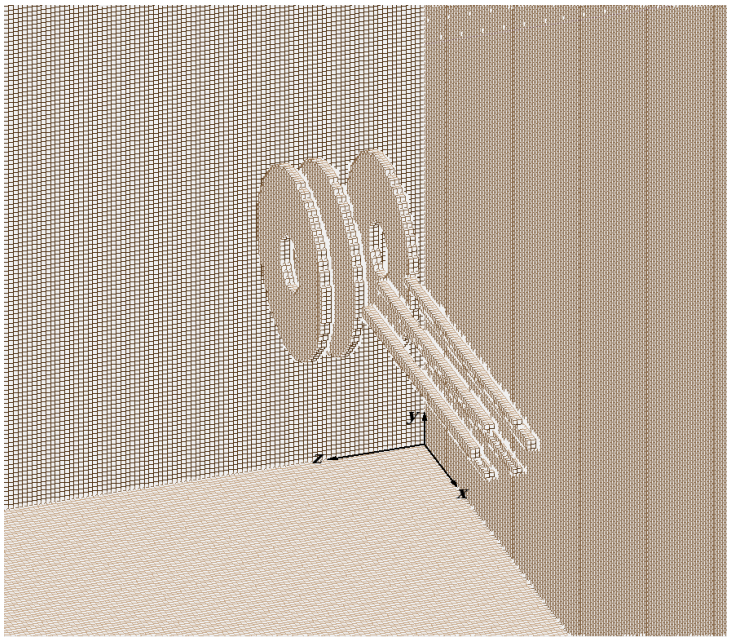

Geometry	
Lower Plate (z)	44mm
Middle Plate (z)	56mm
Upper Plate (z)	63mm
Inner diameter	10mm
Outer diameter	40mm
Hexapole	Standard

Voltages	
Lower Plate (V_1)	1000V
Middle Plate (V_2)	650V
Upper Plate (V_3)	0V
Hexapole	±2500V

The hexapole was in the standard orientation for all runs and had potentials of ±2500V. Figure 33 displays the plots of the asymmetry in E_x as it varies with the z-axis.

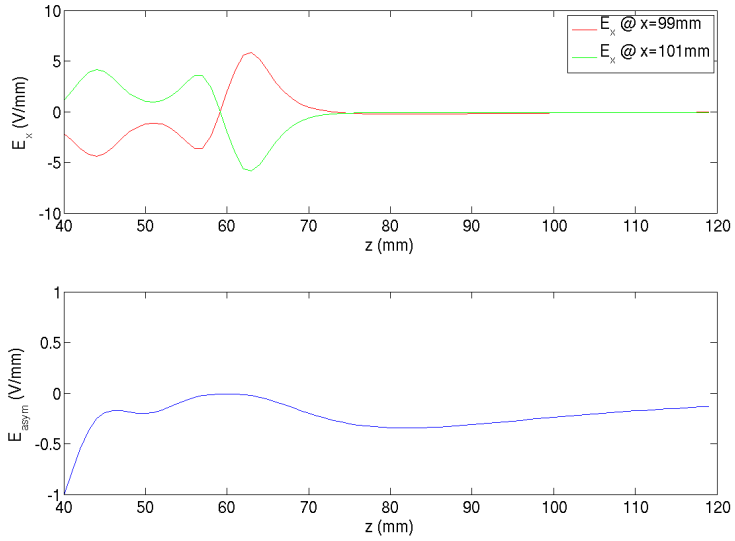

Figure 33. E_x asymmetry plot displaying magnitude of field inhomogeneity introduced by hexapole

The asymmetry in the region between the lower and middle plates (44mm $\leq z \leq$ 56mm) is slightly larger than -0.2V/mm while the asymmetry between the middle and upper plate is orders of magnitude smaller.

The drift region is defined as all points with $z \geq$ 64mm. In theory, the drift region is field free (0V); however, this clearly is not the case as the portion of the drift region directly

following the upper plate contains much larger values of E_{asym} than the first extraction region. To provide a correspondance between the magnitude of asymmetry and the shift in average x position of the ions as they fly towards the detector, figure 34 was produced.

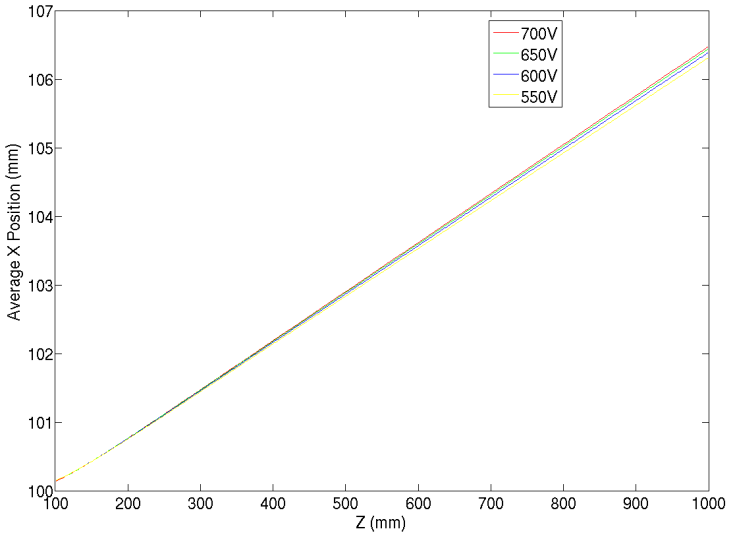

Figure 34. Average x position of ion image at various drift lengths with the nominal geometry. The results for various middle plate voltages are displayed; drift region start: $z = 64$mm

Although all asymmetry plots use the 1000V, 650V, 0V configuration, figure 34 displays the results for the cases when V_2 is 550V, 600V, 650V and 700V. The difference in the average x position for different middle plate voltages is only appreciable after drifting to $z \approx 1000$mm; even at that length the dispersion depending on the voltage configuration is still approximately 2 orders of magnitude smaller than the absolute shift in ion image from the "ideal" case seen in figure 32.

Conclusions The hexapole introduces a substanial asymmetry, which is more pronounced in the drift region than originally expected. After travelling approximately 1m, the average ion position moved $\sim$ 6mm off its intended flight path. To reduce this error, attempts were made to enforce the parallel plate boundary condition by increasing the plate surface area.

C.1.3 Solid Lower Plate

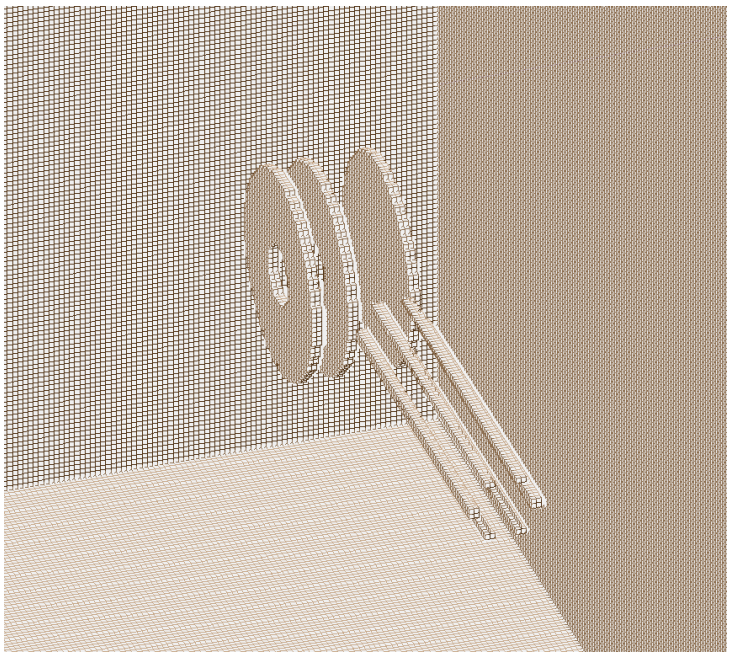

Geometry	
Lower Plate (z)	44mm
Middle Plate (z)	56mm
Upper Plate (z)	63mm
Inner diameter[16]	10mm
Outer diameter	40mm
Hexapole	Standard

Voltages	
Lower Plate (V_1)	1000V
Middle Plate (V_2)	650V
Upper Plate (V_3)	0V
Hexapole	±2500V

[16]The bottom plate does not have a hole

The logical geometry to follow the nominal case is one that is identical in all respects except for the base plate. With a solid base plate, it was anticipated that field homogeneity would significantly improve. Figure 35 displays the E_x asymmetry results.

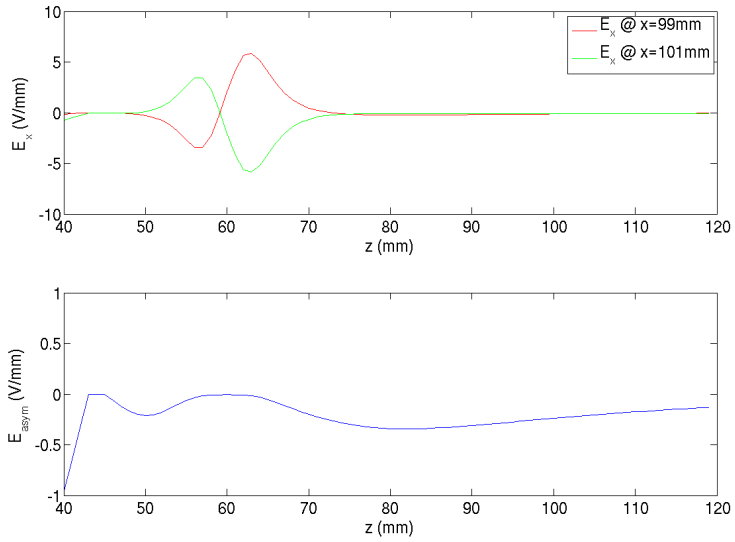

Figure 35. E_x asymmetry using a solid lower plate.

The asymmetry reaches a maximum value of -0.2V/mm between the lower and middle extraction plates. Very little asymmetry can be seen between the middle and upper plates due to their much smaller separation (5mm). It is clear that the drift region is still not a true

drift region given the very large values of E_{asym}, which reach a maximum of approximately of $\sim 0.35\text{V/mm}$ at $z = 82\text{mm}$.

The most noteworthy result of this run is that the asymmetry changes only slightly in the region where the ions start. This means that by removing the hole in the base plate, the field homogeneity improved very little; the impact that a solid plate would have on trapping efficiency would likely outweigh the benefits gained with a solid lower plate (2). To confirm that the field homogeneity was minimally improved, figure 36 displays the average x position as a function of flight length for this geometry.

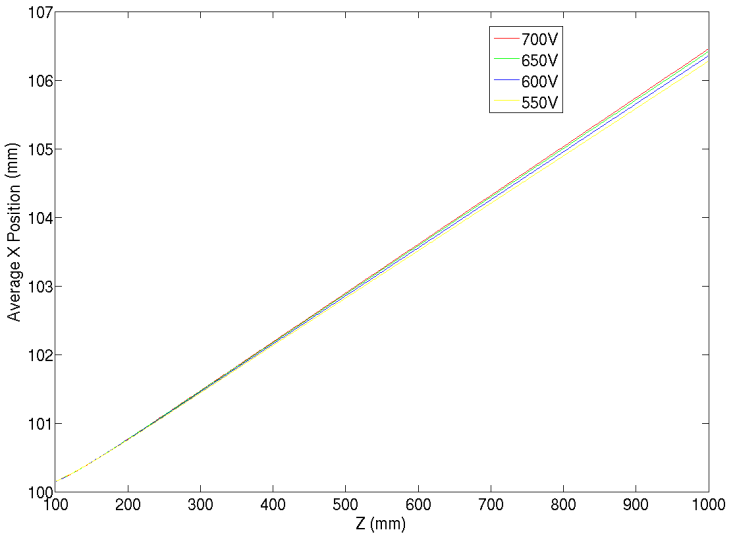

Figure 36. Average x position of ions at various drift lengths using a solid lower plate. The results for various middle plate voltages are displayed; drift region start: $z = 64\text{mm}$.

Conclusions Since removal of the hole does not offer substantial advantages in ion optics, and could significantly hurt the MOT's atom trapping ability, the decision to abandon the solid lower plate geometry was made.

C.1.4 Square Plates

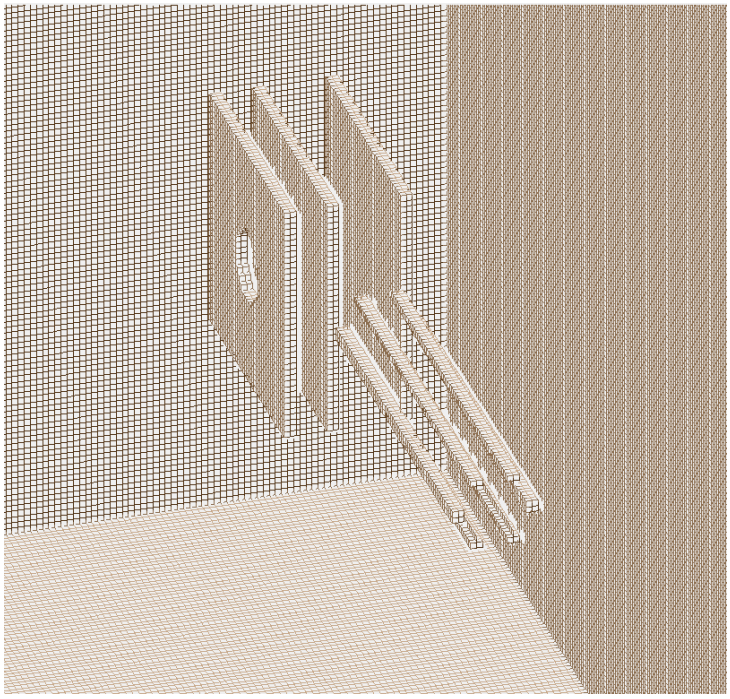

Geometry	
Lower Plate (z)	44mm
Middle Plate (z)	56mm
Upper Plate (z)	63mm
Inner diameter	10mm
Side Length	40mm
Hexapole	Standard

Voltages	
Lower Plate (V_1)	1000V
Middle Plate (V_2)	650V
Upper Plate (V_3)	0V
Hexapole	±2500V

There was no reasoning behind choosing round plates except that round plates were used in the design by Kraft et al. (24), who were trying to accomplish a similar, overall goal. For a given circular plate diameter, a square plate with side lengths equal to that diameter provide more electrode area enforcing the parallel plate boundary condition. Figure 37 is the asymmetry plot for the square plate geometry seen above.

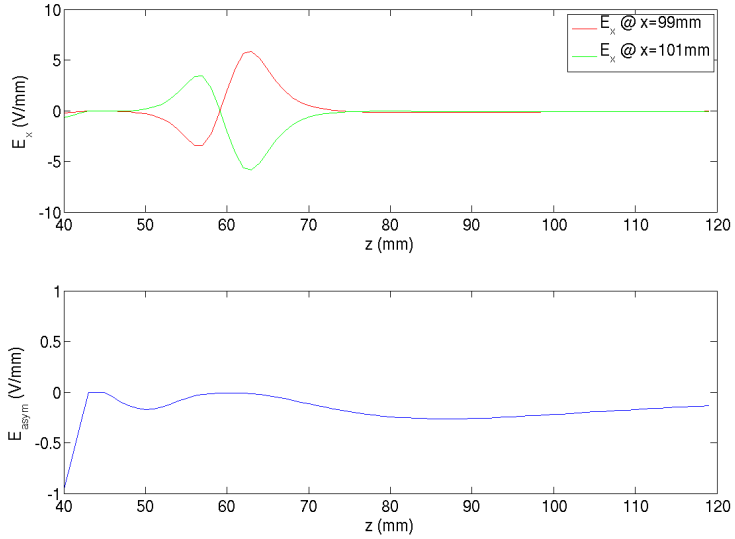

Figure 37. E_x asymmetry using a square plate geometry

Although the decrease in asymmetry does not seem much greater than the decrease caused by using a solid lower plate, the difference is 3.21× larger. A run using the voltage configuration described above yielded the results seen in figure 38.

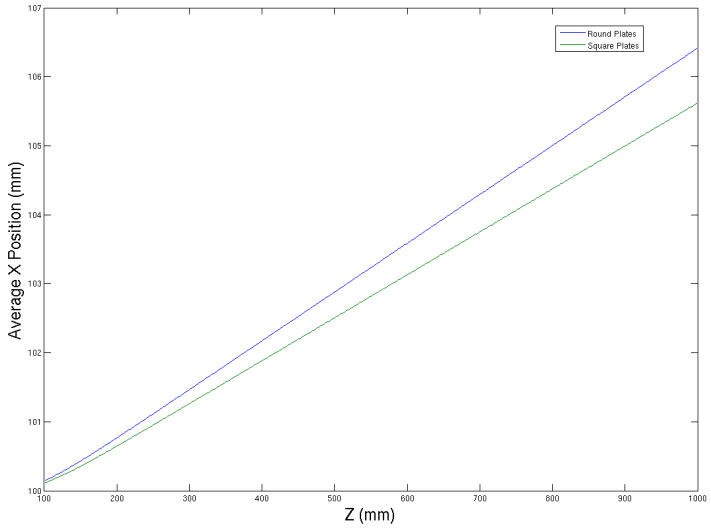

Figure 38. Average x position along flight path using a square plate geometry. Voltage configuration: $V_1 = 1000\text{V}$, $V_2 = 650\text{V}$, $V_3 = 0\text{V}$; ionization volume = nominal.

Conclusions When compared with circular plates, the square plates offered an improvement of $\sim$ 1mm at $z = 1000\text{mm}$ and there were no clear disadvantages of using square acceleration plates. The conclusion made from this trial was to use a square plate geometry

It should be noted that it is possible to tune the average hexapole voltage until the effect it has on ion trajectory is negligible. Many qualitative runs were completed to establish this fact; however, the results of these runs will not be presented here. As part of a sound design, it is preferable that the ion optics of the TOF-MS operate as independently as possible from the hexapole so that a 'retuning' of the hexapole is not required each time the extraction plate voltages are changed.

C.1.5 Complete Drift Shield

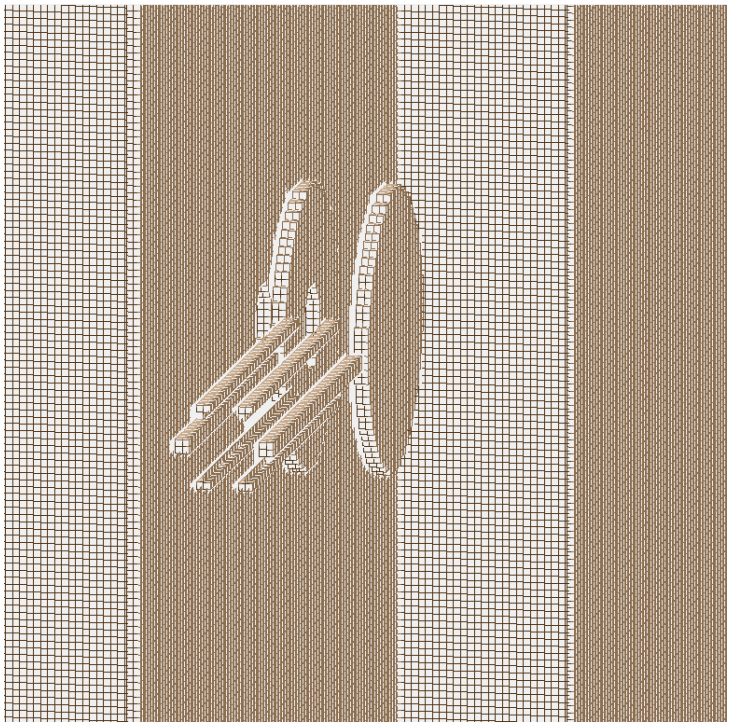

Geometry	
Lower Plate (z)	44mm
Middle Plate (z)	56mm
Upper Plate (z)	63mm
Inner diameter[16]	10mm
Outer diameter[17]	40mm
Hexapole	Standard

Voltages	
Lower Plate (V_1)	1000V
Middle Plate (V_2)	650V
Upper Plate (V_3)	0V
Hexapole	±2500V

[16] The bottom plate does not have a hole

[17] The top plate completely shields the drift region

This geometry was tested in order to isolate the shift in average x position due to the field asymmetry in the drift region and that due to the field asymmetry between the extraction plates. The upper plate was extended to the boundaries of the ion optics workbench to create the perfect drift shield and its success can be seen from the asymmetry plot seen in figure 39.

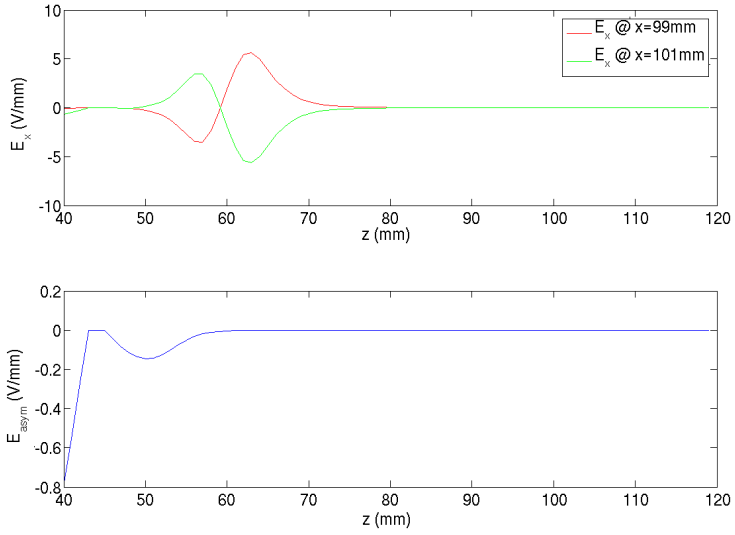

Figure 39. E_x asymmetry using a perfect drift region shield

A run using the wall shield was conducted under the normal voltage configuration to see

how much the average x position was altered when the drift region conditions were ideal ($E_x = E_y = E_z = 0$).

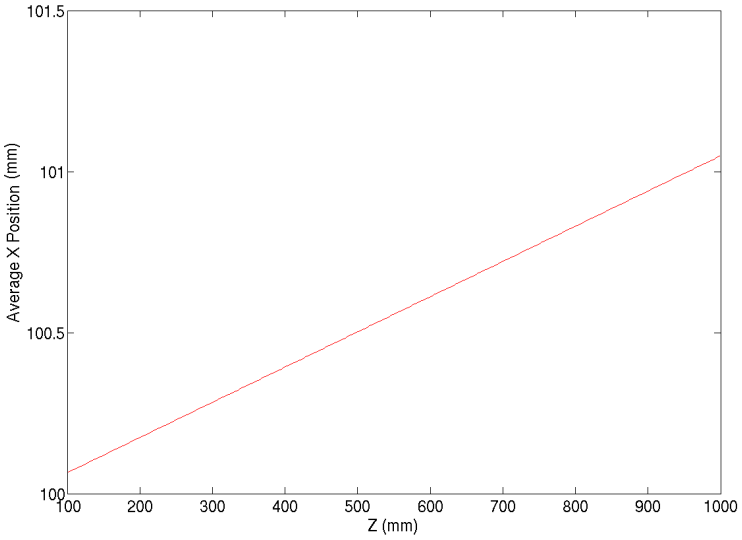

Figure 40. Average x position using a perfect drift shield

Conclusions This result is quite important because it appears that if the drift region can be properly shielded, the perturbation in the extraction region has an effect that is almost an order of magnitude smaller than the hexapole's effect on the drift region. The shift in x position is ~ 1.3mm at $z = 1000$mm, taking into account systematic error, which is an acceptable amount of offset.

Using a tubular shield allows it to serve a second purpose, as a lens. Other shielding ideas also involved modifying the size and shape of the upper plate; however, their ability to shield was not as efficient as the mesh tube. The only disadvantages that could be forseen with the mesh tube were (i) its very high surface area, which could make achieving UHV more difficult[16], and (ii) its potential to act as an obstacle for light generated by the MOT that is to be recorded with a photodiode or CCD camera[17] .

To determine what length of tube would be necessary to work as efficiently as the wall drift shield, a series of runs were performed in which the tube length was varied. The results suggested that a tube approximately ~ 100mm long would be sufficient.

C.2 Magnetic Interference

C.2.1 Background

The influence of the MOT's magnetic field on spatial and temporal dispersion was investigated by applying various anti-Helmholtz fields to the simulation volume. Different coil geometries were used to determine the sensitivity of magnetic field effects to coil size. Intuitively, the

[16]Proper cleaning procedures and handling would negate this disadvantage so its impact on the final shielding decision will not be very strong.

[17]This is a mute point if the imaging is performed through the lower plate.

impact of the field is likely to be less significant, the more focused the ion beam is because the difference in field that each ion experiences will be smaller; for this reason, various middle plate voltages were tested. The nominal geometry with the exception of a solid lower plate was used in the simulations.[18] A smaller overall array volume was used (100mm × 100mm × 1000mm) with the normal grid density (1mm/gu) to decrease magnetic field computation time. This reduction in size means that the ideal flight path of the average ion position is along $(x, y, z) \rightarrow (50\text{mm}, 50\text{mm}, z)$.[19]

It was assumed that the coils of the magnet would be kept outside the vacuum chamber. To reach this conclusion, the advantages were weighed against the disadvantages in the chart seen below. An influential factor not displayed in the table was based on the experience of Dr. Booth, who strongly urged keeping the magnet outside the vacuum chamber.

Advantages	Disadvantages
• Easier to achieve good vacuum	• Limited in coil dimensions
• Fewer components in vacuum makes optical access simpler (mounting components will not be impedance)	• Large eddy currents could be generated in chamber's wall issues if switching the magnetic field on and off is required
• Water cooling of coils is simpler outside of vacuum compared to inside vacuum	• Coil and coil holders will be inconvenient to work around outside of chamber
• Coil holders will not impact field homogeneity (i.e. current carrying wires impacting field lines)	• Need much larger current or many more loops ($R \rightarrow 3R$ then $I \rightarrow 9I$ or $N \rightarrow 9N$ or some combination
• More freedom with plate geometry	

Due to the slow computation time, only $\sim$ 1500 ions could be flown. The ions were not given an initial temperature so that the effect of the magnetic field on the flight path could be viewed independently of initial velocity effects.

[18] The decision to keep the hole in the lower plate had not been made at this point, which is why a solid lower plate was used.

[19] At this time, the ability to view the resolution at all points in the drift region was not possible so plots displaying resolution as a function drift length were not generated.

C.2.2 Tests/Measurements

200mm Diameter Coil - 10G/cm Windings with a diameter of 200mm represent an ordinary set of coils to be used for the MOT in this design (2). Three voltage configurations were investigated to uncover any dependence of the magnetic field's effect on how collimated the ions were after leaving the extraction plates. Using the FWZM definition of mass resolution (R_0), figure 41 was made for comparison between when the coils were on and when they were off.

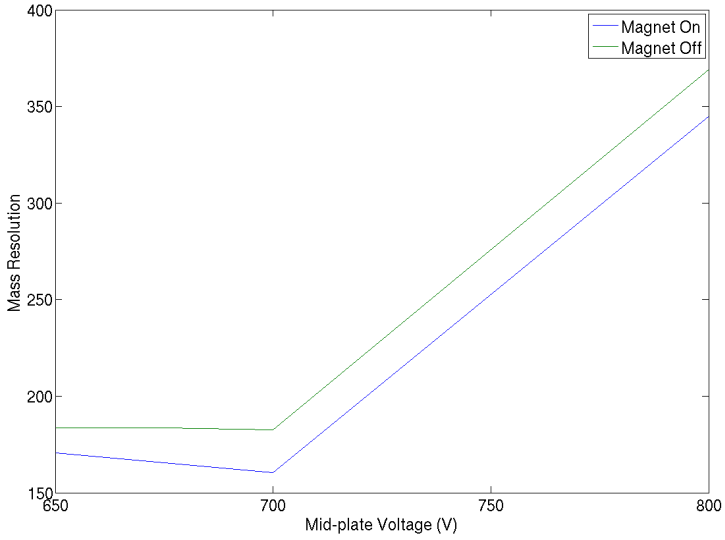

Figure 41. Influence of magnetic field produced by 200mm coils ($\frac{dB_z}{dz} = 10$G/cm) on mass resolution (R_0) at $z = 1000$mm. Voltage configuration: $V_1 = 1000$V, $V_2 = 650, 700, 750, 800$V, $V_3 = 0$V; ionization volume: nominal.

There is approximately a 10% decrease in R_0 that does not show a dependence with V_2. While for certain voltages, the mass resolution is below the goal of 200, this does not represent the resolution at the space focus. While a 10% drop in resolution is significant, it was smaller than anticipated and would not outweigh the difficulties caused by switching the magnet on and off (ex. reduced repetition time, signal noise, event timing, etc...).

Further investigating the case when 650V was applied to the middle plate, it is clear that the magnet contributes to the focusing of the extraction plates since the standard deviation (σ_x) in the x direction is 0.5145mm with the magnet ON and 1.202mm with the magnet OFF at $z = 1000$mm. The average x position (μ_x) with the magnet ON was 53.45mm and with it OFF, the average location was 51.70mm.

Inadvertently, a run with the magnetic off shows that the hexapole's effect can be significantly reduced if the vacuum chamber's diameter is narrower. This geometry exposes the drift region to a hexapole that is half as long and as a result, the deflection was reduced from ~ 6.5mm to 1.7mm.

Conclusions The anti-Helmholtz field does not appear to disturb the flight path to such an extent that it must be switched on and off each flight.

300mm Diameter Coil - 10G/cm Changing the coil diameter had a minimal effect on spatial and temporal dispersion as can be seen by comparing the mass resolution, μ_x and σ_x. Again, there does not appear to be a significant dependence of resolution on middle plate voltage as there is a nearly constant decrease in mass resolution using the FWZM definition.

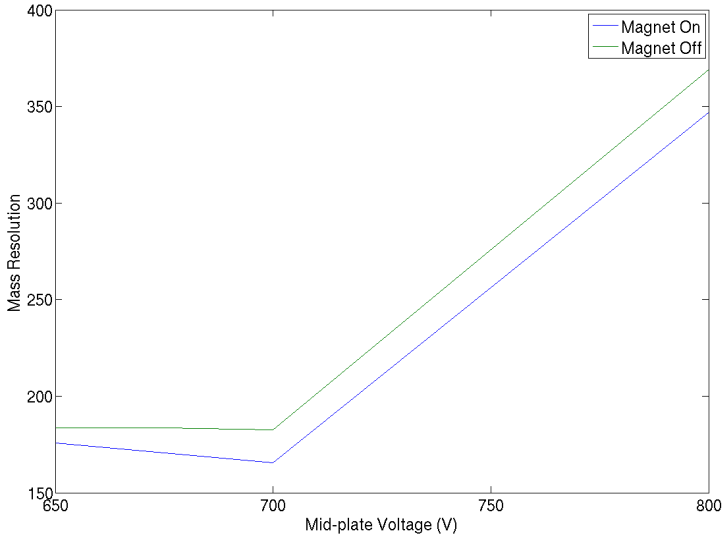

Figure 42. Influence of magnetic field produced by 300mm coils ($\frac{dB_z}{dz} = 10$G/cm) on mass resolution (R_0) at $z = 1000$mm. Voltage configuration: $V_1 = 1000$V, $V_2 = 650, 700, 750, 800$V, $V_3 = 0$V; ionization volume: nominal.

The shift in μ_x was from 51.974mm with the magnet OFF to 53.835mm with the magnet ON. The spread in the x values were very similar and the magnet exhibited its ability to focus ions. With the magnet OFF, σ_x was 10.963mm while with the magnet ON, σ_x was 9.249mm.

Conclusion The results for 200mm and 300mm coils differ by a small enough amount that the impact of the magnetic field was assumed to be constant for coils with this approximate diameter.

300mm Diameter Coil - 100G/cm As a final test, the effect of the magnetic field was amplified by increasing the field gradient by an order of magnitude. At no point would a MOT be operated under this condition, this was done purely to study the impact of the magnetic field. Figure 43 clearly conveys that there is a point when the magnetic field's effect is too detrimental to ignore; with a middle plate voltage of 800V, a drop in resolution of 40.5% is experienced.

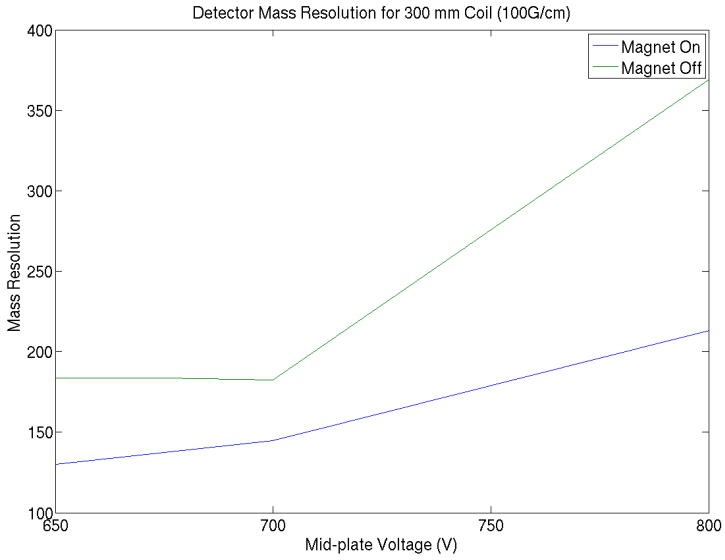

Figure 43. Influence of magnetic field produced by 300mm coils ($\frac{dB_z}{dz} = 100\text{G/cm}$) on mass resolution ($R_0$) at $z = 1000\text{mm}$. Voltage configuration: $V_1 = 1000\text{V}$, $V_2 = 650, 700, 750, 800\text{V}$, $V_3 = 0\text{V}$; ionization volume: nominal.

More interesting is the spatial effect it has on the ion image, which is displayed as figure 44(b). The image of the ions at $z = 1000\text{mm}$ typically looks like figure 45(b); however, the magnetic field has caused the image to rotate. This effect was not measurable with a magnetic field gradient of 10G/cm.

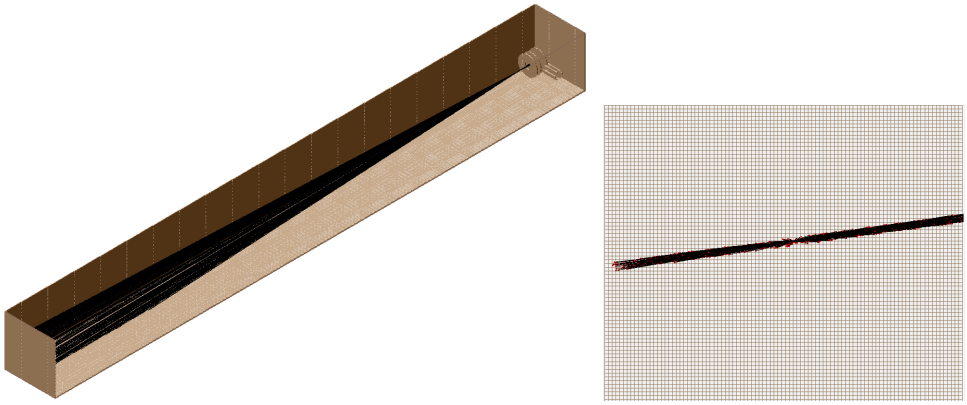

(a) Isometric view (b) XY view

Figure 44. Screenshots of SIMION with middle plate voltage at 800V and $\frac{dB_z}{dz}|_{mot} = 100\text{G/cm}$

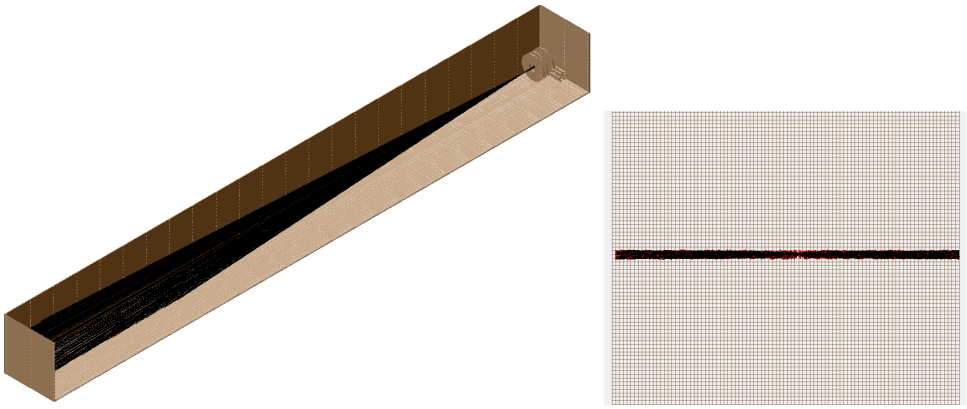

(a) Isometric view (b) XY view

Figure 45. Screenshots of SIMION with middle plate voltage at 800V and $\frac{dB_z}{dz}|_{mot} = 0\text{G/cm}$

Conclusion A spiralling trajectory is characteristic of a magnetic field, so this result was not surprising. The ions remain fairly close to the axis, relative to the diameter of the magnet, throughout their flight. Close to the axis, the $\vec{B}$-field is mainly in the $\hat{z}$ direction. The extraction plates naturally act as electrostatic lenses (see section F) which give the ions a radial components to their velocity. Any radial velocity crossed with a mainly axial magnetic field results in a spiralling motion.

Through correspondence with Dr. Stephan Kraft from (24), it was confirmed that in their design, the MOT does not need to be switched on and off for consecutive trials and the linear TOF-MS he helped design had a mass resolution greater than 1000.

A series of tests were conducted to ensure that SIMION was handling the magnetic fields as expected. While SIMION is capable of solving for magnetic fields, they needed to be modelled externally using Matlab 2008 and then introduced to the simulations through programming in SIMION's RPN language. The results of the tests were consistent with what was expected based on theory, thus corroborating the results of this section.

Impact on Space Focus Resolution After creating a program to record the mass resolution at consecutive z planes in order to see the space focus, a run was performed to support the decision to not cycle the magnetic field between TOF-MS runs. This simulation was also used to provide a quantitative result that could be applied to simulations without a magnetic field to estimate the additional decrease in resolution it causes. 4000 ions were flown with no initial velocity and using the voltage configuration that was adopted in the simulations used to test the final geometry's robustness. Figure 46, displays R_{SD} as a function of drift length in the presence of a magnet field produced by 200mm diameter coils ($\frac{dB_z}{dz} = 10\text{G/cm}$) using the system's final geometry.

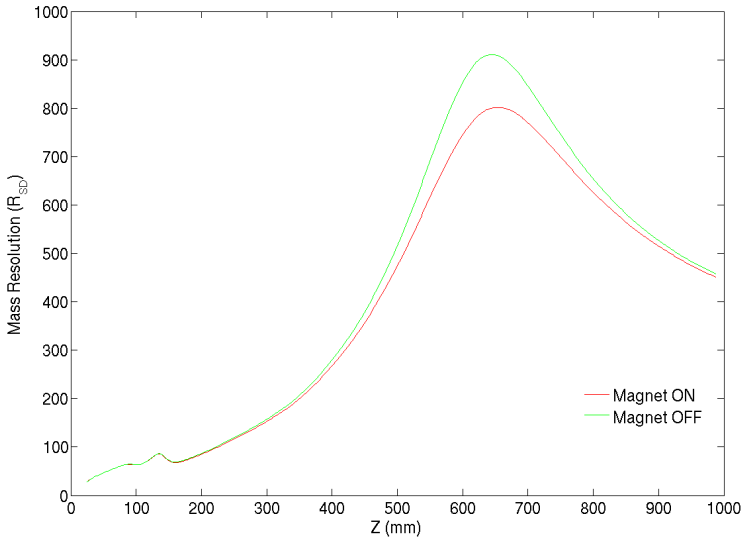

Figure 46. Influence of magnetic field produced by 300mm coils ($100\frac{dB_z}{dz}$) on mass resolution (R_0) at $z = 1000$mm. Voltage configuration: $V_1 = 1000$V, $V_2 = 650, 700, 750, 800$V, $V_3 = 0$V; ionization volume: nominal.

Conclusions This simulation took 2 days to run and from it a general rule was devised to approximate the impact of the magnetic field on the resolution of the space focus. It is clear that the discrepancy between the curves reaches a maximum at the space focus; the mass resolution at the space focus decreased from 910.4 to 801.6. Using this ratio of resolutions, it was assumed that a simulation without a magnetic field could be corrected by increasing the temporal width by 13.6%.

C.3 Lensing

C.3.1 Extraction Plates' Focal Length

A series of short runs were conducted to determine approximately where the extraction plates focus the ions in the drift region as a function of middle plate voltage (V_1). Figure 47 displays the beam width over the entire drift length for middle plate voltages varying between $550-850$V. These runs were made without a hexapole in the geometry; however, runs were completed with a hexapole in the geometry and by visual inspection, it was clear that the hexapole's effect on the focal position was minimal.

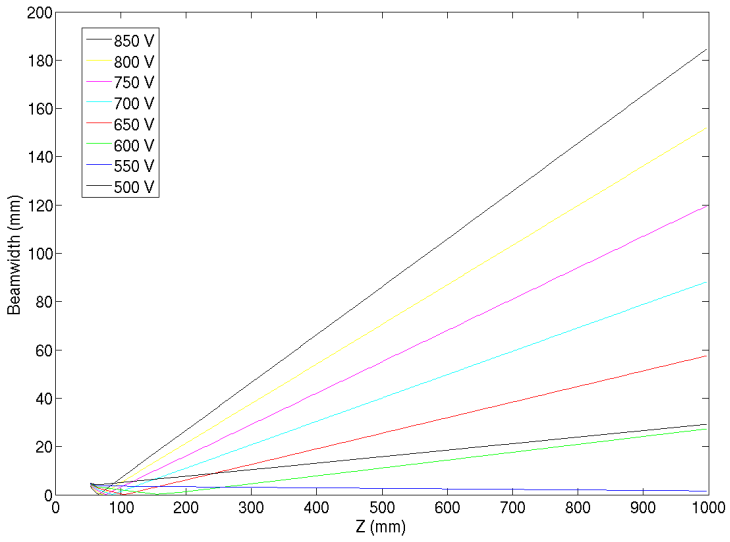

Figure 47. Beam width over entire drift length

An attempt to model the extraction plates using ray optics was unsuccessful, with the discrepancy in the focal length on the order of the focal length itself. This is explain by the poor adherance of the assumptions on which the ray optics theory is based to this particular system (ie. small plates, large aperatures and small plate separations). Further information on how the system was modeled and why the model failed can be found in section F.

Conclusions At $z = 800$mm, the middle plate voltage could be at most 650V to maintain complete transmission. At 850V, such a large number of ions would be lost, that the maximum transmission efficiency would be approximately 30%. Referring to figure 55 of page 71, to move the space focus to a detector at the end of a 800mm drift length, one would need to operate the middle plate voltage at $\sim$ 850V. The lensing effect due to the extraction plates causes the ion beamwidth to be so large that approximately half of the ions would fall on a typically sized detector ($\varnothing$40mm).

C.3.2 Einzel Lens Operating Modes

The decision to operate the Einzel lens in accel-decel mode instead of decel-accel mode was made based on two premises. First, accel-decel mode offers less spherical aberration. From qualitative runs in SIMION™, its ability to ensure 100% transmission was significantly better than decel-accel mode. Using middle plate voltages between 900V and 950V in combination with decel-accel mode lead to the interaction of outlying ions with the fringe fields of the Einzel lens, which ejected them through the electrodes' gaps or diverted them into the lens's walls. One run was made to determine if the decel-accel mode offered any advantage in resolution; figure 48 displays that the two performed relatively equally.

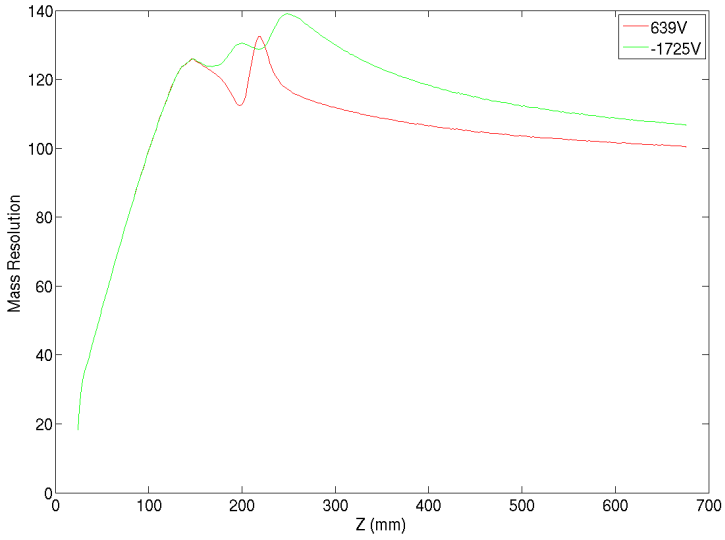

Figure 48. Mass resolution (R_0) performance comparison operating the einzel lens in AD and DA modes. Drift region start: $z = 34$mm; voltage configuration: $V_1 = 1000$V, $V_2 = 600$V, $V_3 = 0$V; ionization volume: nominal.

Conclusions The only drawback of accel-decel mode is that a much larger voltage is needed to achieve the same focal length. In figure 48, the voltages were tuned manually for both operating modes until ions left the lens as parallel to the drift axis as possible; to achieve this in accel-decel mode, the middle electrode needed -1725V applied to it while in decel-accel mode, 639V. In this run, the choice to place the lens's mid-plane 87mm from the upper extraction plate (ie. $z = 121$mm) had not been made, which is why the distortion in the resolution curves does not occur there.

C.4 Realistic Conditions

C.4.1 Large Ionization Volume

Some fraction of molecules outside the studied ionization volume will be ionized unintentionally through NRMPI. The fraction of those ions that impinge on the detector was anticipated to be quite small but some quantification of their transmission efficiency was needed. To predict how many ions outside of the desired ionization volume would navigate through the ion optical elements to the detector, the ionization volume was extended so that is was 75mm in length opposed to 5mm[20]. To maintain a reasonable spatial sampling of this larger volume, the total number of ions flown was increased to 8000.

The vast majority of ions outside the ionization volume did not travel unscathed by electrode walls as can be see from figure 49(a). A closer look at the flight path of ions inside of the ionization volume reveals that if ions did not begin within $\Delta x \simeq 14$mm of the centre-of-mass coordinate($x = 50$mm), they could not enter the aperture; many in fact were diverted away from the aperture as can be seen from the top down view of the extraction plates.

[20] $\Delta y = 0.1$mm and $\Delta z = 0.1$mm

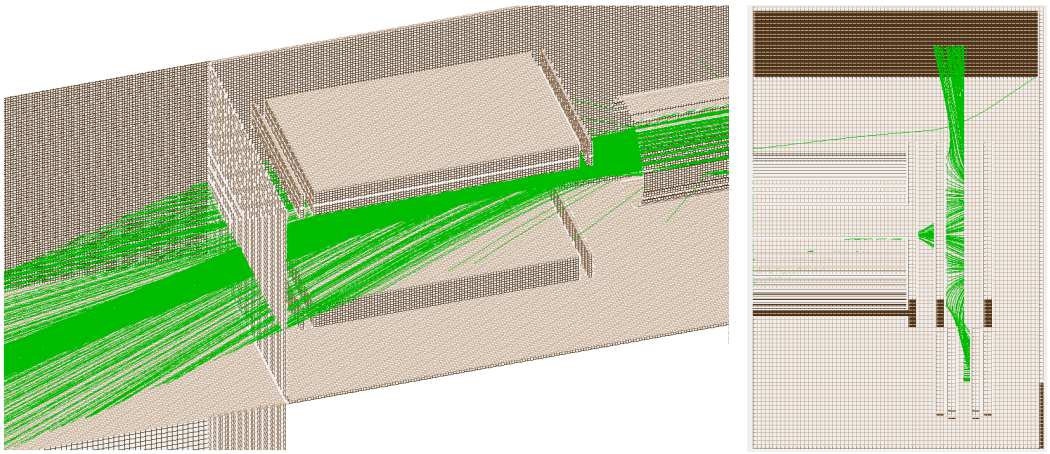

(a) Ion paths through parallel deflector

(b) Ion paths through extraction plates

Figure 49. SIMION screen shots of ion trajectories with large ionization volume

If an imaginary detector against the back wall of the simulation volume was 40mm wide, then 9.81% of the 8000 ions that were flown would have hit the detector. Of those 785 ions, 670 were ions starting within the original ionization volume. This means that there is approximately a 17% increase in the number of ions hitting the detector even though the ionization volume grew 15× in size.

These results assume that there is an equal density of ions outside the volume as there is inside the volume. One would expect there to be a lower density of product molecules outside the MOT volume than within it, especially, if the ionization pulse is sent when the molecules with the most probable velocity are coincident with the MOT's centre.

Of the 107 ions that make up the group that was inadvertently collected, some will be product molecules, which were supposed to be ionized and some will be reactant molecules or atoms that are ionized by NRMPI. Under normal REMPI operating conditions, the ionization probability of a REMPI process is generally three to four orders of magnitude higher than NRMPI. One concern is if product molecules outside of the desired volume are ionized, the performance of the TOF-MS will be further diminished. Figure 50 shows that the drop in resolution was quite substantial but performance was still above our goal. In this case, the FDSDM definition was used because double peaking could not be seen in the histograms and it is a close approximation of $R_{50\%}$ (see figure 51)

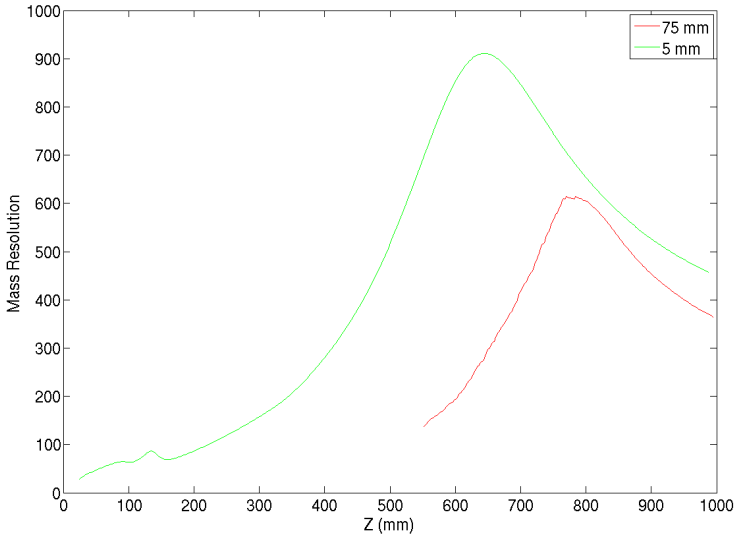

Figure 50. Comparison of mass resolution when ions are produced outside of the nominal volume. Drift length start: $z = 34$mm; voltage configuration: $V_1 = 1000$V, $V_2 = 900$V, $V_3 = 0$V, $V_{def} = \pm 94.3$V; ionization volumes: $\Delta x = 5, 75$mm, $\Delta y = \Delta z = 0.1$mm.

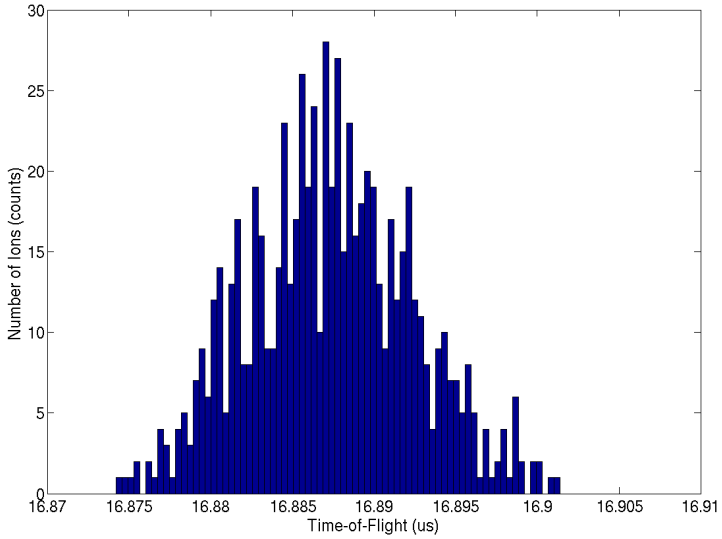

Figure 51. TOF histogram at the space focus when the ionzation volume is $\Delta x = 75$mm, $\Delta y = \Delta z = 0.1$mm.

C.4.2 Li + OH Reaction Assumptions

To state upper limit on the hydrogen atom's velocity, the following conditions were assumed:

1. Li is trapped by the MOT and has zero average velocity
2. OH makes up the molecular beam with velocity directed along $-x$ axis corresponding to the most probable energy of an MBD with $T = 0.1$K

The situation when LiO leaves the collision along the $+x$ axis and H leaves along the $-x$ axis results in the largest hydrogen velocity possible. This velocity was calculated to be 6726.9m/s, which if converted into a MBD with that as its most probable speed corresponds to $\sim 2725K$. Had the hydrogen exited the collision at some angle with respect to the x-axis, its momentum would not be as great so by assuming this speed is the most probable speed is already a considerable overestimate of the actual case but will provide an upper bound on the deterioration of performance.

C.4.3 Hot & Cold Products

The heavy molecule was given a mass and temperature of 100amu and 1K, repectively, while the light atom was given a mass of 1amu and 4000K in one scenario, and 1amu and 5000K in the other scenario. The voltage configuration for these runs were identical: $V_3 = 1000$V4, $V_2 = 900$V, $V_1 = 0$K and $V_{def} = \pm 94.3$V. The main conclusion that was drawn from this run was that although small atoms/molecules may move with much higher velocities than cold products, the reduction in mass resolution is not on the scale it would need to be to result to cause overlap between the two species. This fact is made apparent by the large separation between the 1amu peak around $t = 1.5\mu$s and the 100amu peak around $t = 15\mu$s seen in figures 52(b) and 53(b)

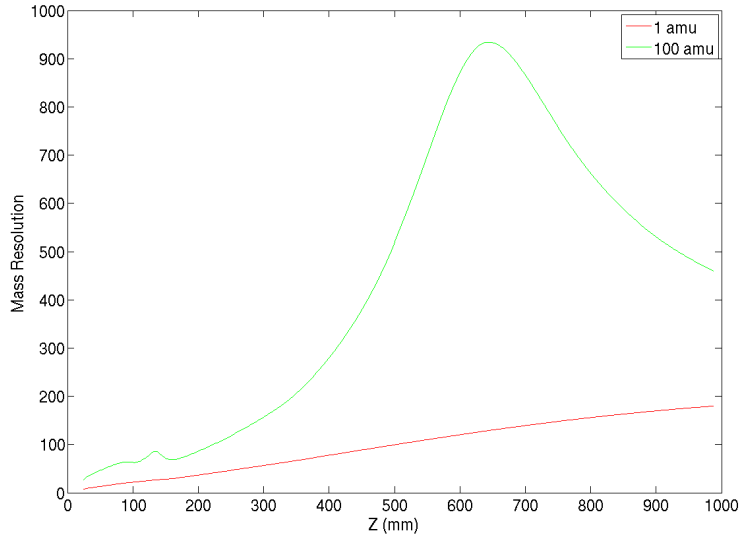

(a) Resolution over drift length

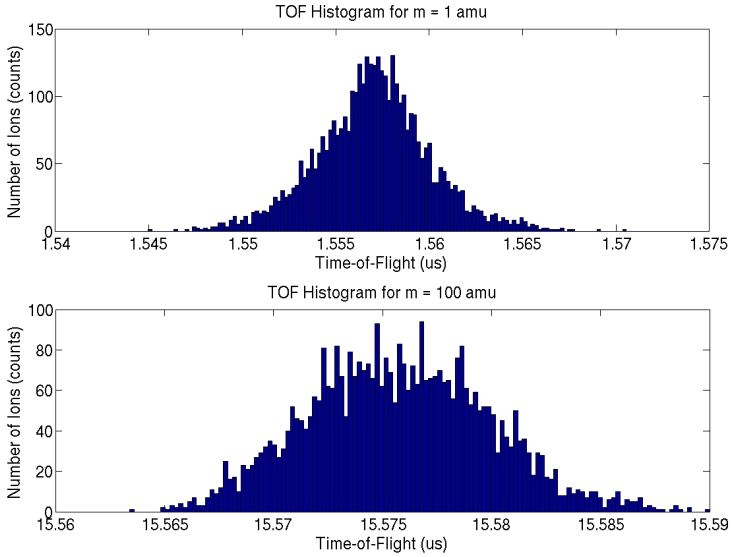

(b) TOF histograms for 1amu & 100amu

Figure 52. Resolution (R_{SD}) over the entire drift length for both chemical species and the associated TOF histograms at the space focus of the 100amu molecule 4000K. Drift length start: $z = 34$mm; voltage configuration: $V_1 = 1000$V, $V_2 = 900$V, $V_3 = 0$V, $V_{def} = \pm 94.3$V; ionization volume: $\Delta x = 5$mm, $\Delta y = \Delta z = 0.1$mm.

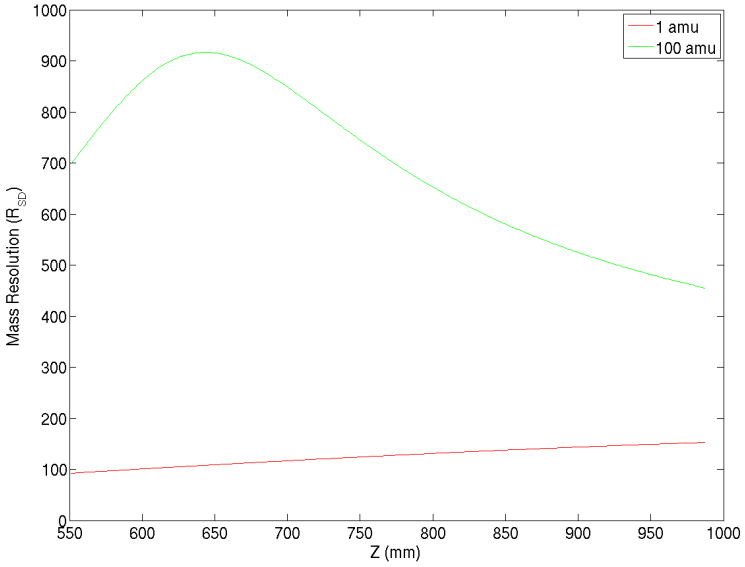

(a) Resolution over drift length

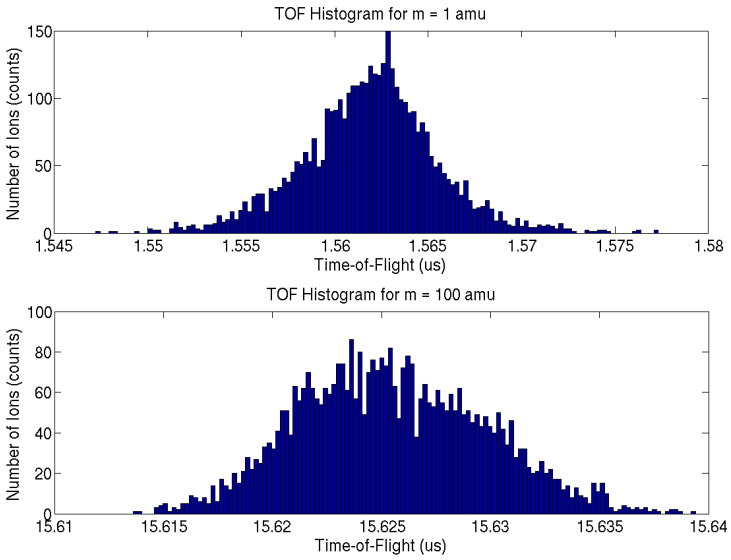

(b) TOF histograms for 1amu & 100amu

Figure 53. Resolution (R_{SD}) over the entire drift length for both chemical species and the associated TOF histograms at the space focus of the 100 amu molecule. Light molecule has temperature of 5000K. Drift length start: $z = 34$mm; voltage configuration: $V_1 = 1000$V, $V_2 = 900$V, $V_3 = 0$V, $V_{def} = \pm 94.3$V; ionization volume: $\Delta x = 5$mm, $\Delta y = \Delta z = 0.1$mm.

C.5 Space Focus Tunability

The major advantage that a Wiley-McLaren style extraction plate geometry has is the ability to move the space focus to the detector's location. With a simple, two plate extraction region, the space focus is located $2s_0$ from the upper extraction plate, where s_0 is defined in section 2 (5).

From equation 3, d is a function of the ratio E_2/E_1 and L_2/s_0. To confirm that the SIMION simulations had reasonable results, a series of runs were conducted in which the lower and upper plates were held at 1000V and 0V, respectively, while the middle plate voltage was varied. By varying the middle plate voltage and holding the geometry constant, E_2/E_1 is varied, which should move the space focus to a predictable location. All trials before this set of runs used middle plate voltages in the range of $550\text{V} - 700\text{V}$, which made it appear as though the space focus could only be shifted by a small amount.

These runs were conducted before investigating the use of an Einzel lens to correct beam divergence. To keep the beam collimated to prevent ions from hitting the side walls, the aperture was changed from a circle to a slot, as seen in figure 54. A slot aperture has twice the focusing power of a circular aperture but only in the direction parallel to the shorter dimension of the slot.

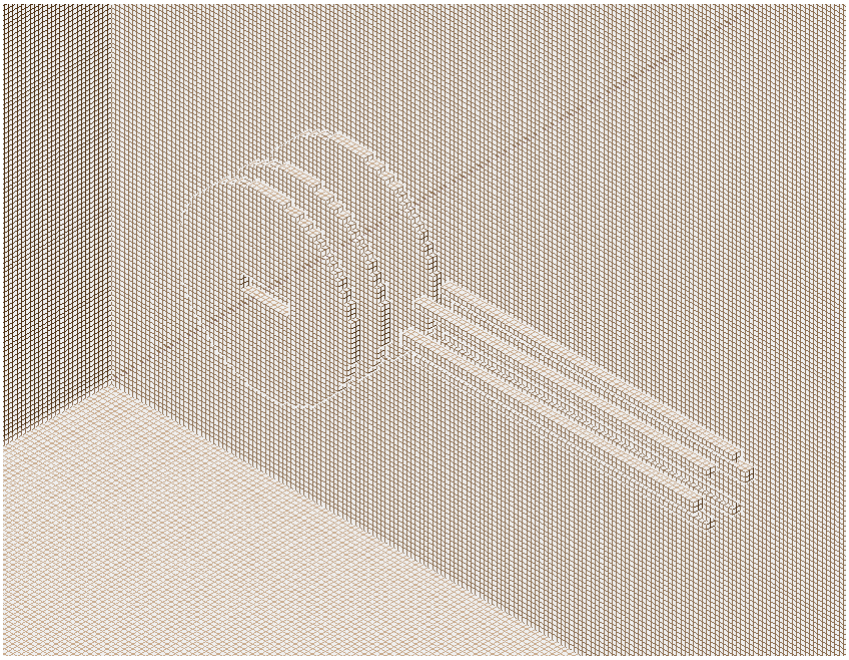

Figure 54. Slot aperture geometry

After completing runs using voltages between 550V and 900V, the space focuses were located and figure 55 was made to compare the locations with the locations predicted by equation 3.

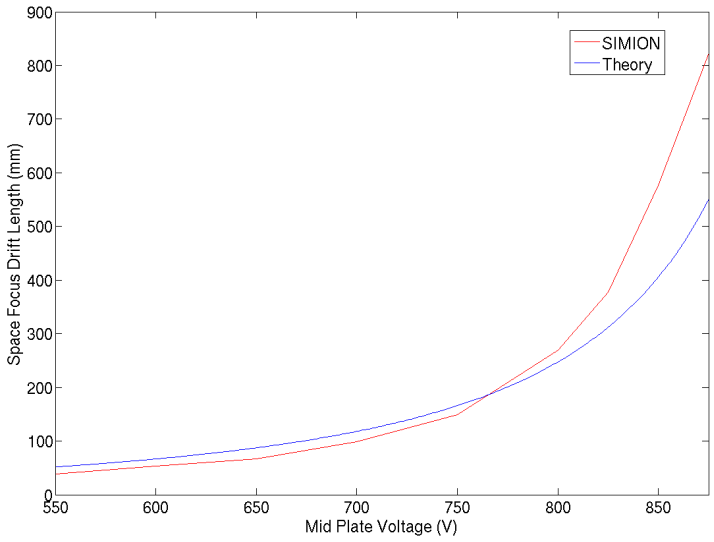

Figure 55. Location of space focus in drift region as a function of middle plate voltage

The field distortions induced by the hexapole played some role in moving the location. The equation derived in (5) is based on a 1D analysis, which does not account for the plates' apertures.

Figure 55 makes it clear why such a small variation in the space focus position was seen when operated with a middle plate voltage between 550V and 700V.

C.6 Hexapole Orientation

The hexapole was the first component introduced to the Wiley-McLaren MS layout. It was anticipated that the hexapole's close proximity to the extraction plates would pose the main obstacle to design around because it was required to be no further than 25mm away from the centre of the plates(8). There were two reasonable ways that the hexapole's axis could be oriented: in a plane between the lower and middle plates (figure 56(a)) or directly aligned with the plates' axis (figure 56(b)).

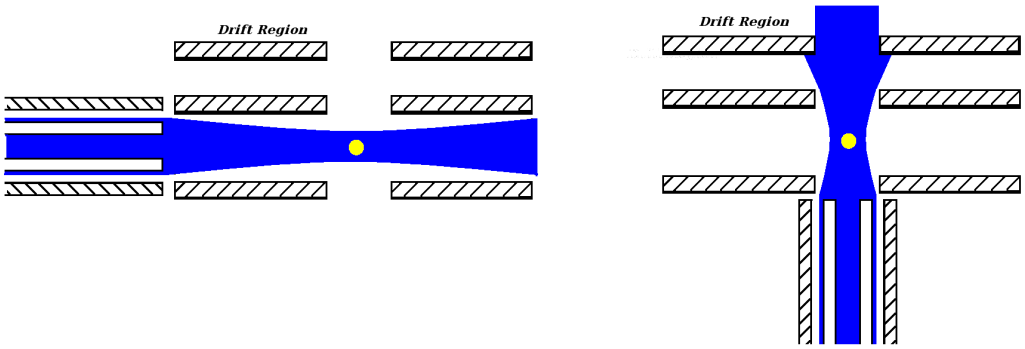

(a) Orientation 1 (b) Orientation 2

Figure 56. Two possible hexapole orientations (red = molecular beam, yellow = trapped atoms)

Figure 56(a) was used for the reason that figure 56(b) would put the hexapole in the path of the MOT laser passing through the centre-hole of the plates. The MOT lasers along this axis would have to fit between two consecutive poles of the hexapole (4mm), which would be very difficult and make the MOT optics unnecessarily complicated. It does have the advantage that it would likely be less perturbative to the electric field, and the hexapole's face could be brought closer to the trapped atoms; however, these advantages would not outweigh the complexity it adds to the MOT optics (2).

The hexapole could be rotated into any orientation about its axis, so a decision to set the hexapole orientation early on in the design process was made. The standard orientation is that seen in figure 57(a) while the non standard orientation represents the standard orientation rotated by 30^o.

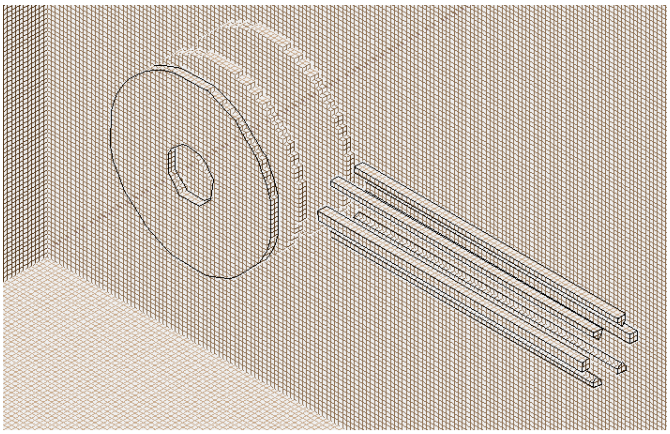

(a) Standard

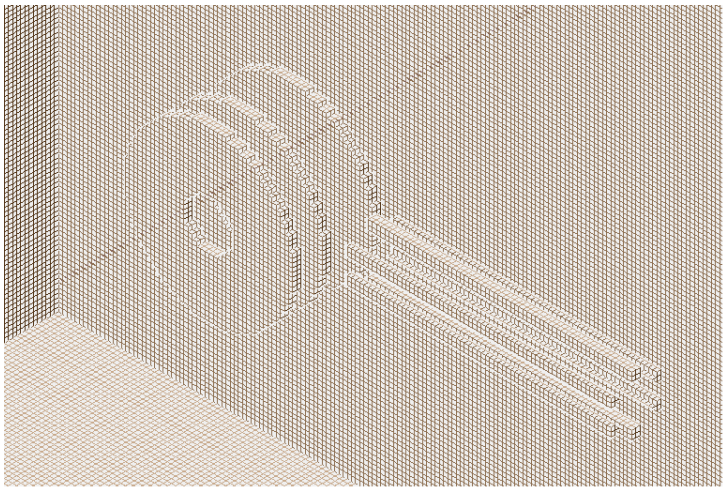

(b) Non-standard

Figure 57. Hexapole orientations

Comparing simulations with the same extraction plate geometry and voltage configuration ($V_1 = 1000$V, $V_2 = 650$V and $V_3 = 0$V) but different hexapole orientations, neither presented an obvious gain in mass resolution performance as can be seen in figure 58.

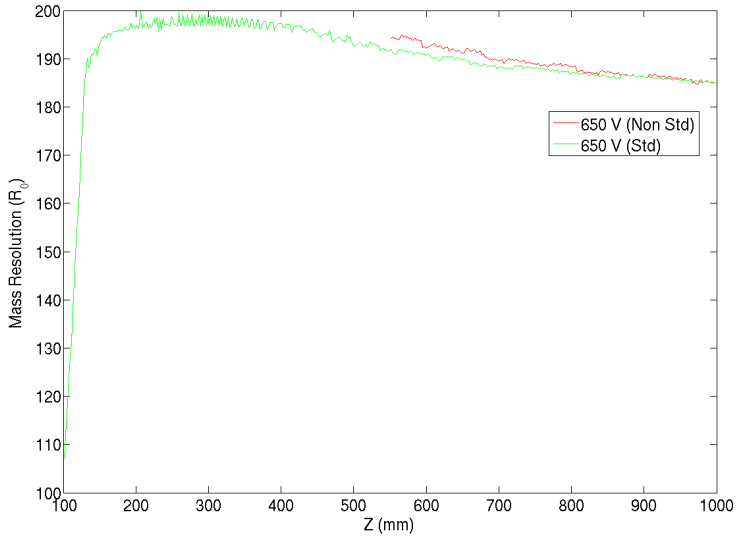

Figure 58. Resolution over drift length for both hexapole orientations. Data was only collected for the non-standard orientation over last half of the drift length.

A comparison of the average x position of the ion cloud yielded a slightly different outcome as can be seen in figure 59. At all distance in the drift region, the non-standard orientation was nearly twice as far from the ideal flight path ($x = 100$mm). Without further investigation into what was causing the significantly higher transverse force on the ions, the decision to always operate with the hexapole in the standard orientation was made.

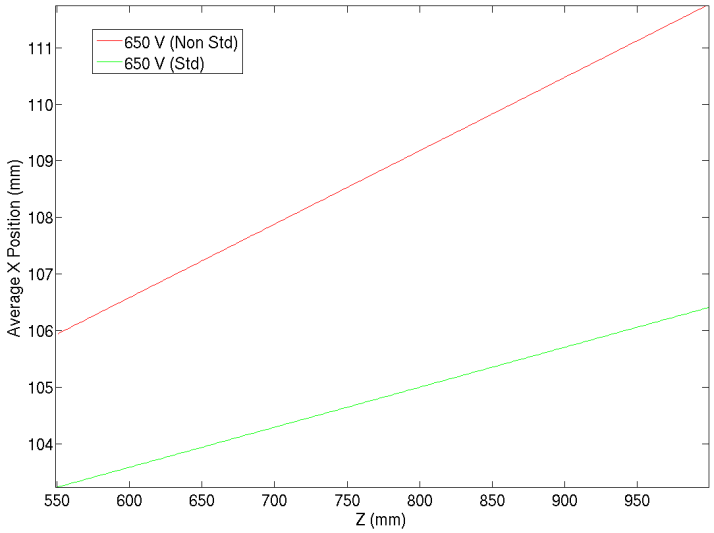

Figure 59. Average x position over drift length for both hexapole orientations. Data was only collected for the non-standard orientation over last half of the drift length.

D Ion Detectors

Continuous dynode electron multipliers (EM) are by far the most commonly used detectors in TOF-MS. Within this class of detector, there are two main types: [21] the channeltron and the microchannel plate detector (MCP) . In comparing MCPs and channeltrons, the MCPs are typically the instrument of choice in TOF-MS because they are capable of producing pulses that are $\sim$ 1ns (36) in duration while channeltron pulses are typically 20ns in duration (28).[22]

An MCP can be operated in two different modes: analog and pulse counting. The mode that it is operated in is dependent on the rate of ion events. Event rates below $10^8 s^{-1}$ can be captured in pulse counting mode, which can result in a more sensitive detection and more accurate quantification of the number of ions of a given mass (36).

[21] Microsphere plates are less commonly found in literature and there appears to be only a single manufacturer, El-Mur Ltd, that produces them. Compared to the other two detectors, it is a very new technology with advantages and disadvantages that are still being studied (36). For this reason alone, this detector was eliminated as a suitable ion detector candidate.

[22] For low ion count rates, the MCP is generally operated in pulse counting mode, which is analogous to photon counting with a photomultiplier tube. A longer pulse duration results in a longer deadtime, which reduces the maximum rate ions can hit the detector due to pulse pileup.

E Vacuum

Although the precise geometry of the vacuum chamber was not considered extensively, an investigation into the necessary vacuum quality was undertaken to determine a suitable vacuum pump cost in the budget.

The vacuum pressure that is generally required in time-of-flight mass spectrometers $\sim 7.5 \times 10^{-6}$torr (28). The design criteria for this apparatus is to have a maximum flight path of 1m.

The mean free path of a particle in a gas is found using (37),

$$L = \frac{kT}{\sqrt{2}p\sigma}, \tag{21}$$

where σ is the collision cross section ($\sigma = \pi d^2$), d is the sum of the background gas's and ion's van der Waal radii , k is Boltzmann's constant, T is the temperature of the background gas and p is the background gas pressure. Sample values provided in (37) to represent typical mass spectrometer parameters are the following: $T = 300$K, $k = 1.38 \times 10^{-23}\text{m}^2\text{kgs}^{-2}\text{K}^{-1}$ and $\sigma = 45 \times 10^{-20}\text{m}^2$. When substituted, this yields the relationship,

$$L = \frac{4.95}{p} \tag{22}$$

where p is in millitorr. This leads to a free path length of ~ 660m at 7.5×10^{-6}torr, which is much greater than the ion's flight path length. The losses due to ion neutral collisions will be quite small even if it is assumed that each collision results in neutralization and/or redirects the ion away from the detector.

The pressure requirement during normal operation of the hexapole is $\sim 1 \times 10^{-8}$torr according to Vyskocil (23). In general, MOTs require vacuum pressures of 1×10^{-8}torr to ensure an appreciable trap lifetime (2).

Discussions with Dr. Madison suggest that alternatives to a turbopump, such as a sputter ion pump, should strongly be considered for achieving better vacuum conditions. However, careful placement of an ion pump is crucial since an ion pump generates ions and has stray magnet fields, which could further reduce the TOF-MS performance. The grounded grid over the face of an MCP minimizes any electric fields that actively accelerate stray ions towards the detector.

F Ray Optics

F.1 Aperture Lenses

Plate electrodes with small holes seperating two regions of space with different electric fields act as lenses analogous to thin lenses in light optics. In literature, they are known as aperature lenses and have a focal length defined by(9),

$$f = \frac{4V_a}{E_2 - E_1}, \tag{23}$$

where V_a is the particles kinetic energy (V), E_1 is the electric field strength[23] (V/m) in the region the particle is leaving, E_2 is the electric field strength (V/m) in the region the particle will enter and f is the focal length of the aperature lens. Ray optics is generally used to provide first order estimates of different properties of ions. Figure 60 illustrates the radial electric field that produces a virtual ion image (diverging rays) if positive ions were flown from the stronger electric field region (E_1) into the weaker electric field region (E_2).

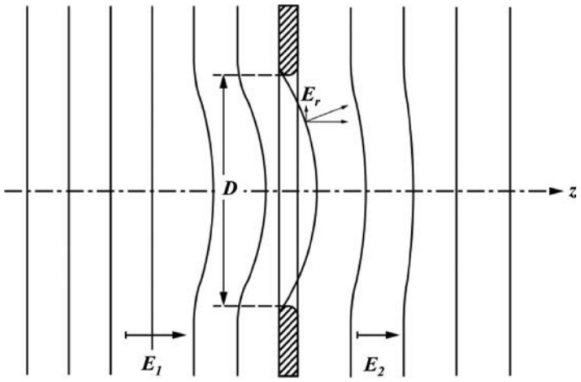

Figure 60. General aperature lens (9)

A ray optics approach was initially used to model the Wiley-McLaren extraction plate arrangement, as a means of checking the reliability of the results produced by SIMION. However, the assumptions that ray optics is based on break down immediately once aperatures in electrodes are improperly represented as perturbations in the electric field (9).

F.2 Einzel Lenses

Two categories of ion optical lenses exist: immersion lenses and unipotential lenses. An immersion lens is one that changes the kinetic energy of ions after they pass through it while a unipotential lens does not. An Einzel lens is a 3-piece, unipotential lens that can be made up of cylindrical electrodes or apertures electrodes. Typically, cylindrical electrodes are used because designing the electrode support structure is much simpler. This lens system's major difference from an aperture lens is that the thin lens approximation no longer applies so two principal planes and two focal planes are needed to describe the lens. An example of an Einzel lens and its cardinal planes can be seen in figure 61.

[23] A positive electric field strength will accelerate a positively charged particle in the positive direction

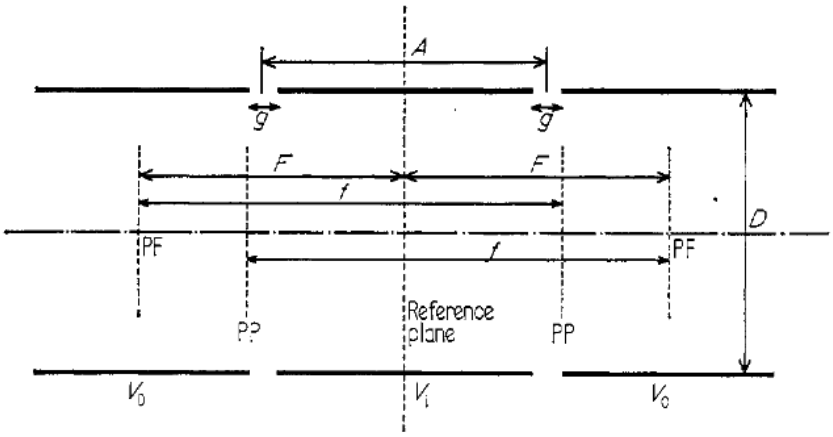

Figure 61. Einzel lens schematic displaying the reference plane (or mid-plane), 2 principal focal planes (PF) and 2 principal planes(PP) (11)

The voltage on the two outer electrodes (V_0) is the same while the middle electrode is held at a potential either above or below this potential. An Einzel lens is delineated by its electrode gap-to-diameter ratio (g/D) and mid-electrode length-to-diameter ratio (A/D). An Einzel lens has two operating modes for any given focal length (F): accel-decel and decel-accel. In accel-decel mode, $V_i > V_0$ while in decel-accel mode $V_i < V_0$. Whenever possible, it is best to operate in accel-decel mode because the resulting flight path is kept closer to the cylinders' axis, which results in smaller spherical aberration (10). As well, to avoid significant spherical aberration, the filling factor of the lens should not exceed 50%. The filling factor is the ratio of the diameter of the ray bundle at the first gap to the diameter of the lens (10).

The most extensive resource of focal length properties is Harting and Read's *Electrostatic Lenses*, 1976. A copy of the this book could not be obtained in a timely manner so the work of (11) was used to obtain the focal properties for a typical lens geometry.

The voltage dictated by (11) to be used to create a parallel beam was in disagreement with the voltage obtained through manual tuning in SIMION™. This was attributed to the fact that Adams and Read (11) calculated the axial potentials of an Einzel lens assuming that the outer electrodes were very long compared their diameter. This assumption simply is not applicable to the Einzel lens geometry implemented in this design as the outer electrode length-to-diameter ratio was 1.8.

F.3 Deflection Plates

A parallel plate condenser is a commonly used ion optical device seen extensively in orthogonal acceleration TOF-MSs. In this design, it was considered as a method for directing ions off their original course once they leave the extraction plate region. A simple parallel plate geometry can be seen in figure 62, illustrating the small angle deflection of a positive ion as it passes through a uniform electric field.

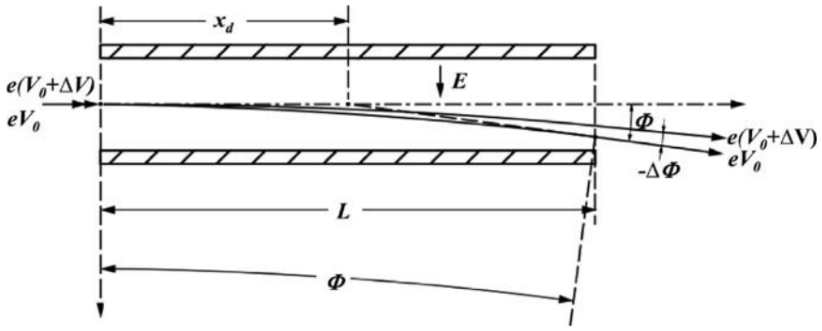

Figure 62. Small angle deflection of positive ion passing through a parallel plate condenser (9)

The relationship between the deflection angle (Φ) of an ion entering in the plane halfway between the plates, where $V = 0$, and the voltage (V_a) applied to the plates separated by a distance d is given by,

$$\Phi \simeq tan\Phi = \frac{1}{2}\frac{L}{d}\frac{V_a}{V_o}, \tag{24}$$

where eV_o is the kinetic energy of the ion as it enters the uniform electric field region, and L is the length of the plates (9). This, of course, assumes that there is an abrupt transition between the outer, field-free region and the parallel plates' electric field. As a first approximation this is true; however, in mass spectrometry, the effect of the plates' fringe field cannot be ignored. In fact, it has a very important effect on isochronous surfaces.

Dahl et al. (13) describe a compact, modular deflector that makes use of field terminating electrodes just outside of the parallel plate deflectors. Assuming that the plate voltages are centred about zero, the "bulging" field lines bend the ions away from the mid-line as they enter the parallel plates. Once the ions are within the parallel plate region, the ions will have different longitudinal speeds. When the condition $V_a x/V_o d << 1$ holds true[24], the isochronous rotation angle is equal to the angle of deflection (Φ) but opposite in direction (see figure 63) (12). This condition was satisfied in nearly all simulations suggesting that the detector's angle should not be constrained to an orientation angle that is normal to the incident ion path.

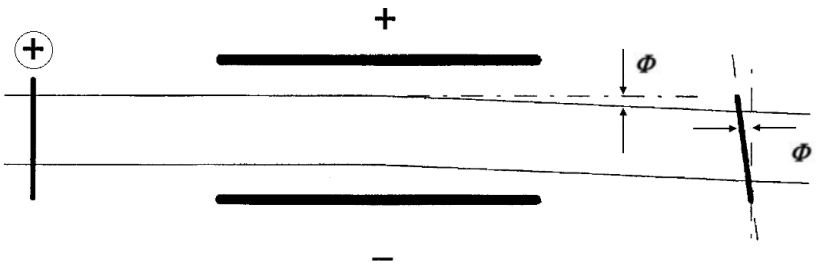

Figure 63. Isochronous surface that enters parallel plates with orientation normal to z-axis leaves rotated by the same angle it was deflected but in the opposite direction (12).

Finally, to mitigate the penetration of stray electric fields from other ion optical components, field terminators are typically used. This has been thoroughly investigated by Wollnik and

[24] x refers to the quantity defined in section 3.5

Ewald (38) for the case of stray fields penetrating a magnetic energy analyzer and a parallel plate condenser. Dahl et al. (13) stresses the importance of field terminators in his modular beam deflector design in order to minimize the defocusing of the ion beam as it enters the parallel plates. With field terminators, the effective length of the plates increases, which should be taken into account when calculating the voltage to apply to achieve a particular degree of bending; figure 64 can be used to predict the effective length of parallel plates with thin field terminators.

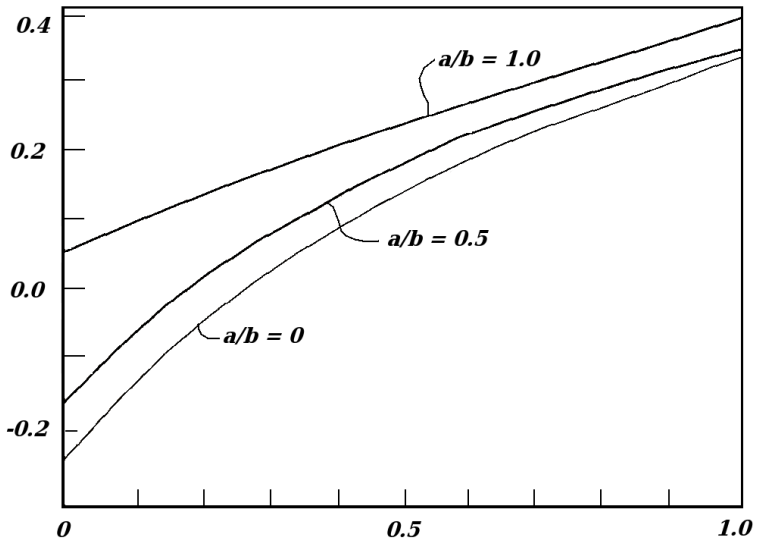

Figure 64. Plot to determine effective cut-off of parallel plate field (d^*) using a thin grounded diaphragm as a field terminator (36).

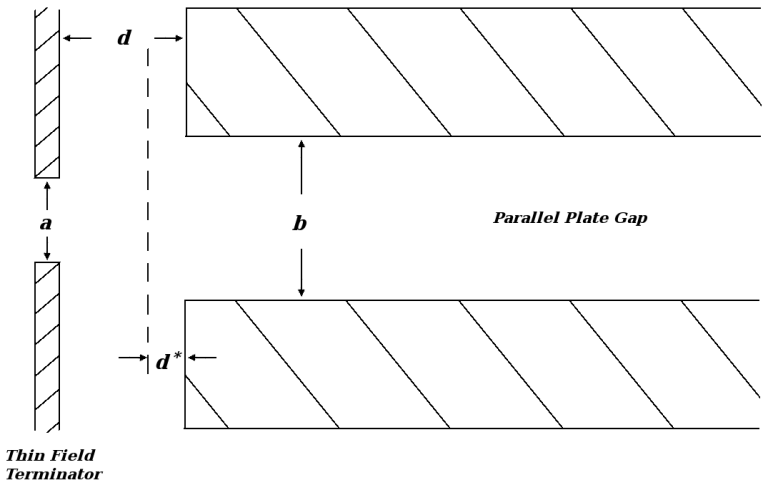

Figure 65. Field terminator geometry (36).